AN ABSTRACT OF THE DISSERTATION OF

Liangdong Zhu for the degree of Doctor of Philosophy in Physics presented on November 2, 2017.

Title: Optical Development and Materials Applications of Tunable Femtosecond Stimulated Raman Spectroscopy

Abstract approved: _____
Chong Fang

To obtain a mechanistic understanding of the chemical processes, techniques that offer a frame-by-frame visualization of molecular structure during a reaction are of vital importance. Numerous efforts and advances have been made in order to acquire such vivid molecular "movies", especially in the electronic excited state. Ultrafast molecular spectroscopy method with sufficient spatial and temporal resolutions provides such a possibility. In particular, the recent development and implementation of femtosecond stimulated Raman spectroscopy (FSRS) has achieved previously hidden information of the structural dynamics of many intriguing photosensitive molecular systems across disciplines. As a technique in the mixed time-frequency domain, performing FSRS has its unique benefits in tracking vibrational dynamics, enhancing transient species, improving the signal-to-noise ratio, and so on.

In this dissertation, I will cover our experimental work on optical innovation, the unique broadband up-converted multicolor array (BUMA) technique, the incorporation of BUMA

into FSRS setup, expanding the versatility and area of application possibilities and the exploratory effort of studying metalorganic complex precursors in solution for metal oxide thin films using ultrafast spectroscopy tools including FSRS.

The convenient and economical generation of background-free, spatially dispersed BUMA signals is realized in a 0.15-mm-thick BK7 glass slide with spectral tunability from visible to near IR. Using one of the BUMA sidebands as probe pulse, the FSRS measurement yields high-quality Raman spectrum spanning a broad detection window of ca. 100—4000 cm^{-1}, where Raman peaks in both low-frequency and high-frequency regions are well resolved without any unwanted interference pattern.

From the first prototype, we moved forward to build a versatile and efficient wavelength tunable FSRS setup, which includes simultaneously tunable Raman pump and probe pulses in the visible. A spectral resolution of ~12 cm^{-1} is achieved in the lab. Pre-resonance enhancement of FSRS signals of a photoacid pyranine in aqueous solution by tuning Raman pump toward the electronic absorption peak is achieved, where the stimulated Raman gain of the 1627 cm^{-1} mode is increased by over 15 times.

Moreover, the methodology of concomitantly generating two distinct sets of temporally controllable BUMA sidebands is demonstrated in a versatile optical setup. By varying the time delay between the two incident laser pulses with suitable crossing angles, we can continuously tune the BUMA signals from the visible to near-IR range, which sequentially emerge on either side of the 800 nm fundamental pulse, in both BBO crystal and BK7 glass. Ultrabroad bandwidth of ~2000 cm^{-1} is obtained. The pump-power-dependence of

sideband signal indicates that the sideband signal goes through an intrinsic nonlinear parametric amplification process in BBO.

Further development of the FSRS setup in the ultraviolet (UV) region has been made by using another set of BUMA sidebands with bluer center wavelength (ca. 360—460 nm). The Stokes spectrum of 15 mM laser dye LD390 in solution with an electronic absorption peak at ~355 nm, was found to be >21 times stronger with a 400 nm Raman pump than that with 550 nm Raman pump. The Raman spectrum of LD390 was collected over a ~1400 cm^{-1} detection window for the first time. Using the same 400 nm ps Raman pump from a home-built second harmonic bandwidth compressor, the anti-Stokes Raman spectrum turns out to be even stronger than the Stokes spectrum, which is attributed to different resonance enhancement factors involving ground and electronic "vibronic" levels.

To implement our technical innovations in tunable FSRS to tackle problems in materials science, we systematically performed a set of experiments to study dynamics of metal-organic complexes precursors for bismuth tungsten oxide thin film. Solutions of two precursor molecules, triphenyl bismuth (Ph_3Bi) and tungsten hexacarbonyl [$W(CO)_6$] were studied. Simultaneous generation and characterization of crystalline bismuth thin film from Ph_3Bi in methanol were achieved and confirmed by detection of a coherent A_{1g} optical phonon mode of the nascent crystalline bismuth.

Subsequently, transient absorption and tunable FSRS techniques were synergistically used to investigate the UV photolysis of tungsten hexacarbonyl in solution and the ensuing solvent molecule binding events. After 267 nm femtosecond laser irradiation, the excited

state absorption band of $W(CO)_6$ within ~400—500 nm exhibits distinct dynamics in methanol, tetrahydrofuran, and acetonitrile on molecular timescales. The delineated photochemical reaction pathways on the basis of ligand nucleophilicity and solvent reorientation time provide the rational design principles for solution precursors.

Optical Development and Materials Applications of Tunable Femtosecond Stimulated Raman Spectroscopy

by

Liangdong Zhu

A DISSERTATION

submitted to

Oregon State University

in partial fulfillment of
the requirements for the
degree of

Doctor of Philosophy

Presented November 2, 2017
Commencement June 2018

Doctor of Philosophy dissertation of Liangdong Zhu presented on November 2, 2017

APPROVED:

Major Professor, representing Physics

Head of the Department of Physics

Dean of the Graduate School

I understand that my dissertation will become part of the permanent collection of Oregon State University libraries. My signature below authorizes release of my dissertation to any reader upon request.

Liangdong Zhu, Author

ACKNOWLEDGEMENTS

I would like to express my sincere thanks to my advisor, Dr. Chong Fang, for his generous guidance, knowledge, constant support and patience throughout the completion of my Ph.D. study. Dr. Fang's strong dedication to fundamental research and keen passion for new discoveries set a great example for me. This work would not have been possible without his excellent technical guidance, discussions, and editorial advice.

I would give special thanks to Dr. Henri Jansen. Without his help, I might have given up along the way.

I would like to thank Dr. Sean Burrows, Dr. Stephen Lancaster, Dr. Yun-Shik Lee and Dr. David McIntyre for serving as my committee members.

I also want to thank all my friends and labmates for their advice, support, encouragement and friendship.

Thanks to the Department of Physics, Department of Chemistry, and Center for Sustainable Material Chemistry led by Dr. Douglas Keszler for proving me such a wonderful opportunity to study, research, live, and grow over the years.

Last but certainly not least, I sincerely appreciate my parents and wife Qin Zhou for their unconditional love and endless support.

CONTRIBUTION OF AUTHORS

Prof. Chong Fang has contributed to the design, execution, and writing of each published article and each chapter in this Ph.D. thesis. Prof. Douglas A. Keszler and Dr. Sumit Saha from Center for Sustainable Materials Chemistry (CSMC) and Department of Chemistry at OSU collaborated on the projects about metal-organic complexes as solution precursors for metal oxide thin films. Dr. Weimin Liu, Dr. Fangyuan Han, Ms. Yanli Wang, and Mr. Liang Wang at the Fang Lab have supported the experimental or theoretical efforts in completing the relevant projects on ultrafast optics and materials sciences.

TABLE OF CONTENTS

TABLE OF CONTENTS (Continued)

TABLE OF CONTENTS (Continued)

TABLE OF CONTENTS (Continued)

LIST OF FIGURES

Figure Page

LIST OF FIGURES (Continued)

Figure Page

LIST OF FIGURES (Continued)

Figure Page

LIST OF TABLES

Table Page

Chapter 1 General Introduction

1.1 Motivation

For a physical chemist or chemical physicist, experimentally mapping out the multidimensional potential energy surface (PES) of chemical reaction is an ultimate goal. To fulfill this goal vibrational spectroscopic methods provide the possibility, where the quantized energy level relationships, instantaneous frequencies, populations and anharmonicities information of a system can be obtained. Once such information of a reactive PES is acquired, extremely accurate predictions of the rate and outcome of a chemical reaction will be possible. As a result, the reaction pathway can be directly controlled even in a complex environment such as solution. Ultrafast spectroscopy might help solve this PES myth, which is able to reach picosecond, femtosecond, or even attosecond time scales at which atomic and molecular systems evolve.

Over the years, light has become increasingly important in revealing the complexity of nature, since radiation can be used as an effective tool to investigate matter and study phenomena too fast or invisible to the human eye. After excitation by a photon, photosensitive or photoreactive molecules structurally evolve along many different nuclear coordinates and react on the femtosecond (fs) to picosecond (ps) time scale by isomerizing, breaking bonds or ejecting electrons. To probe the evolution of these intrinsically fast molecular transformation processes it is necessary to have spectroscopic methods that are capable of providing structural information with fs time resolution. The most widely used ultrafast technique is transient absorption, which collects time-resolved electronic spectra

in the excited states. In this classic pump-probe scheme, the first (pump pulse) photoexcites the sample, initiating the dynamics of interest; the second (probe pulse) at a precisely determined later time point detects the induced modifications to the molecular system.

However, to obtain structural information about the nuclear dynamics accompanying a photochemical process it is crucial to record vibrational spectra of the system as it evolves. Vibrational spectroscopy is a promising approach to capture structural changes on the fs to ps time scale. By studying the time-dependent behavior of individual vibrational bands, the molecular evolution is mapped along the multidimensional reaction coordinates. Femtosecond Stimulated Raman Spectroscopy (FSRS) is a novel time-resolved technique to monitor structural changes during ultrafast photophysical and photochemical processes. Remarkably, FSRS performed in the mixed time-frequency domain can achieve both fs time resolution and chemical-bond-level spatial resolution.

The use of vibrational spectroscopies represents a significant advance towards understanding PESs, as vibrational frequencies correspond directly to structure and depend greatly on the interplay between nuclear motions. Comparing to the widely used infrared (IR) spectroscopy, which is limited to a relatively narrow bandwidth in the mid-IR and commonly suffers from the intense and broad vibrational absorption bands from water and other solvents, FSRS does not have those drawbacks.

FSRS enables efficient data collection in the electronic excited state, which ensures the integrity of analyzing transient vibrational intensity, frequency, and bandwidth. FSRS employs a sophisticated fs-ps-fs pulse sequence that ensures the balance between

photoexcitation timing, pulse peak density, and the perturbative approach to the sample system under study. Transient Raman mode intensity and frequency dynamics are key information derived from FSRS as a function of time. The FSRS method allow us to generate signal photons in the electronic excited state without impulsively exciting all modes, because the preceding actinic pump in our set up has a typical bandwidth of ~500 cm^{-1} so only low-frequency modes are impulsively excited and acquire coherent character starting from the "time zero" of a photoinduced process. In contrast, the recently developed time-resolved impulsive Raman technique uses all fs pulses, essentially performing transient absorption in the electronic excited state.[1,2] Because the pertinent vibrational information needs to be retrieved from spectral oscillations measured in the electronic domain (different from measuring the stimulated Raman scattering signal directly in the frequency domain), peak analysis therein becomes rather challenging and extensive data processing with Fourier transform are required to convert the time domain signal into frequency domain peaks. Notable, the simultaneous generation of excited state population with coherent motions in FSRS provides an intuitive platform to dissect the potentially functional roles of low-frequency skeletal motions along photochemical reaction coordinates. We note that the coherent motions refer to the phase relationship between an ensemble of molecules which dephase typically on the few ps timescale in solution due to molecular collisions and energy relaxation. FSRS can also take advantage of resonance Raman enhancement effect by tuning the Raman pump-probe pair into an electronic transition band while does not require the use of ultrashort pulses below 10 fs for instance.

1.2 Application and improvement of FSRS in our group

A typical FSRS setup consists of a fs actinic pump, a narrowband ps Raman pump and a broadband fs Raman probe. The Raman pump and probe pulses coincide on the sample, while time delay between the actinic pump and Raman probe is varied as the time axis.[3]

The pioneering work of FSRS can be traced back to Yoshizawa and co-workers in 1999 and Mathies and co-workers in 2003.[4,5] After that, FSRS has been developed into a general, versatile, and powerful spectroscopic platform to study a wide variety of photosensitive systems.[6-16]

As our group was established at OSU Chemistry in 2010, we aimed to further develop and exploit the full potential of this structural dynamics technique. The proof-of-principle experiment using FSRS to reveal a functional motion in wild-type (wt)GFP conducted at UC Berkeley has motivated us to build an improved setup to tackle more challenging problems in energy and health-related fields.[13] We have since developed an innovative broadband up-converted multicolor array (BUMA) methodology to provide a background-free Raman probe that can be conveniently tuned by changing the crossing angle of two incident beams or the time delay between them.[17,18] By selecting different transparent media and carefully adjusting the beam geometry, the Raman probe tunable range covers near UV to near IR. Usually spectral regions near 800 or 400 nm are where the laser fundamental pulse or second harmonic pulse overwhelms SCWL, making it extremely difficult to detect low-frequency Raman modes if the Raman pump needs to be at 800 or

400 nm. With the BUMA sideband as Raman probe, this common problem is circumvented. Together with a narrowband Raman pump at 800 nm from a home-built grating-slit-based spectral filter[19] or at 400 nm from a home-built second harmonic bandwidth compressor (SHBC),[20,21] we have collected high-quality Stokes and anti-Stokes FSRS data of a photoacid in solution and metal-organic complex in solution from the broad UV to near-IR region.[22,23] During the electrolytic synthesis of aqueous Al nanoclusters as solution precursors to make high-quality metal oxide thin films, this improved FSRS methodology with BUMA-based Raman probe enabled us to monitor the intermediate structures and formation pathways of the unique *flat* Al_{13} aqueous clusters *in situ*.[14]

The tunability of ps Raman pump has been achieved using a two-stage noncollinear optical parametric amplifier (NOPA) pumping a tunable ps seed by a ps 400 nm pulse generated by the aforementioned SHBC.[20] The ps seed is the result of spectral filtering the output of a fs-NOPA that operates in the ca. 480—750 nm region with a Type-II BBO crystal. With this tunable FSRS setup where every optical component easily accessible on the optical table, we have experimentally investigated a wide array of photosensitive molecules with various absorption and emission properties. For example, we directly observed hydrogen bond breaking events followed by excited-state population bifurcation and solvation with 660 nm Raman pump and 670–760 nm Raman probe pulses, which pre-resonantly enhance transient coumarin 102 (C102) species in the singly excited state following 400 nm photoexcitation.[24] In another study of popular model photoacid pyranine, we directly observed an intermolecular hydrogen bond stretching mode at ~180 cm^{-1} between the

photoacid (proton donor) and water molecules (proton acceptor) from the Stokes and anti-Stokes FSRS experiments which corroborated the contact ion-pair formation and excited-state proton transfer (ESPT) reaction on the sub-ps to tens of ps timescale.[25]

In a GFP-based calcium biosensor study, the Raman pump was tuned to 530 nm that approaches the stimulated emission band of the deprotonated chromophore inside the GFP pocket. Together with a broadband Raman probe generated in 2-mm-thick sapphire crystal plate to perform Stokes FSRS, we uncovered the working mechanism of an intensiometric protein biosensor, G-GECO1.1, which highlights the deprotonation process and a two-ring twisting process of its embedded Thr-Tyr-Gly chromophore.[26,27]

Following several successful applications of tunable FSRS to different systems, we have developed a general rule to position the Raman pump and Raman probe wavelengths in reference to excited state absorption (ESA) or stimulated emission (SE) bands, which could constitute an effective experimental strategy to increase the signal-to-noise ratio (SNR).[28] We recently presented a comprehensive study of stimulated Raman line shapes of the photoacid pyranine in neat methanol with tunable Raman pump and probe pulses across an ESA band. Following 400 nm photo-excitation, the dynamic and mode-dependent Raman line shapes of pyranine were recorded, which substantiates the power of wavelength-tunable FSRS and caution to avoid right-on-resonance conditions and dispersive line shapes.[29]

1.3 Outline

In Chapter 2, we briefly discuss several ultrafast optical techniques that have been implemented into our experimental setup to enable our advanced ultrafast spectroscopy.

In Chapter 3, we report the generation of spatially dispersed BUMA signals via cascaded four-wave mixing (CFWM) processes in a 0.15-mm-thick BK7 glass slide, using two weak near-IR fs laser pulses and any transparent media with third-order nonlinear susceptibility $\chi^{(3)}$ can in principle be used. This work also represented the first time that the BUMA sideband was implemented into an FSRS setup collecting the ground-state Raman spectrum of a solvent.

In Chapter 4, we report a versatile and efficient tunable FSRS setup which includes Raman pump and probe pulses both tunable in the visible region from the same fs laser source. The narrowband ps Raman pump wavelength tunability of ca. 480—750 nm with power as high as 14 mW (laser repetition rate is 1 kHz). Our second harmonic bandwidth compressor design involves only one grating. In parallel, the broadband fs Raman probe (450—850 nm, <100 μW) was generated from the spatially separated BUMA laser sidebands, which provide convenient tunability and self-compression on the basis of CFWM.[17,19] Both the solvent cyclohexane and the photoacid pyranine were studied using tunable FSRS and we confirmed the feasibility of tuning the Raman pump-probe pair as well as the power of pre-resonance enhancement to improve the SNR of sample system. This work demonstrates that tunable FSRS can be accomplished from commercially available fs laser amplifier

system with routine optics to tackle a wider range of challenging problems in research labs and field applications.[13,14,30,31]

In Chapter 5, we exploit the methodology of simultaneously generating two distinct sets of temporally controllable BUMA sidebands. in a thin transparent medium. The temporal chirp of a broadband supercontinuum white light (SCWL) allows us to vary the time delay between SCWL and a stronger fundamental pulse (FP) at 800 nm to sequentially generate two sets of laser sidebands on either side of the FP in BBO crystal. Numerical calculations at phase-matching conditions reveal that the unique BUMA signals on the SCWL side mainly arise from the interaction between $\chi^{(3)}$-based FWM-OPA and CFWM processes. After a systematic measurement of the pump-power-dependent sideband signal amplification aided by simulation results in BBO crystal and BK7 glass, we prove that $\chi^{(2)}$-assisted OPA contributes to sideband amplification and WL-BUMA generation in BBO.

In Chapter 6, we describe the first implementation of a UV-FSRS setup with a home-built second harmonic bandwidth compressor (SHBC, output at ~400 nm center wavelength, ~1.5 ps fwhm of pulse duration) as the Raman pump and BUMA sideband laser pulses (ca. 360—460 nm, fs) as the Raman probe to collect the stimulated Raman spectrum. The particular BUMA signals was generated from SFG/SHG-based CFWM processes in a thin BBO crystal. Besides providing previously unavailable spectroscopic characterization of a laser dye, our experiment manifests the advantage of using tunable FSRS to study molecules with different absorption profiles even into the UV region. Using the ps 400 nm Raman pump, both Stokes and anti-Stokes Raman spectra were collected and compared.

In Chapter 7, we applied our optical techniques on metal-organic complexes in solution as a collaborative work with Center for Sustainable Materials Chemistry (CSMC) led by Dr. Keszler at OSU Chemistry. We demonstrated simultaneous generation and characterization of crystalline bismuth thin film from triphenyl bismuth (Ph_3Bi) in methanol using a combination of fs transient absorption (fs-TA) upon UV laser irradiation and UV-FSRS in the electronic ground state. Fourier transform analysis of spectral oscillations observed in fs-TA of Ph_3Bi in methanol reveals a coherent A_{1g} optical phonon mode at ~90 cm^{-1} which can be attributed to the nascent crystalline bismuth directly formed out of solution, which was an exciting discovery of "Nanowrite" in a laboratory setting. A notable blueshift of the phonon mode with increasing irradiation time tracks the gradual thickening of bismuth thin film reaching ~80 nm after 90 min. On the microscopic timescale, a prominent ~4 ps decay time constant of the excited-state absorption band was attributed to a metal-ligand bond-weakening/breaking intermediate process. Our versatile optical setup enabled us to accomplish the laser-induced crystallization process *in situ*, making high-quality thin films from the bottom-up and directly from solution while tracking key spectral signatures.

In Chapter 8, we apply fs-TA and tunable FSRS spectroscopic methods to study the UV photolysis of tungsten hexacarbonyl [$W(CO)_6$] and subsequent solvent binding events. Despite extensive study of this compound in solution, the photoinduced dissociation and solvation processes remain elusive. We track the excited-state absorption band within ~400—500 nm in various solvents on molecular timescales after 267 nm fs laser irradiation and observed distinct time constants which can be correlated with different photoinduced

processes from solvent complexation, solvation to ligand rearrangement. Such structural dynamics insights further substantiate the combined resolving power of ultrafast electronic and vibrational spectroscopic methods to dissect the photochemical reaction coordinates of metal-organic complexes in solution, which provide the much needed rational design principles for solution precursors (with suitable metal center and surrounding ligands) in nanowrite applications.

In Chapter 9 we provide the perspectives of this series of work in concluding remarks.

1.4 References

[1] M. Liebel, C. Schnedermann, T. Wende, and P. Kukura, "Principles and Applications of Broadband Impulsive Vibrational Spectroscopy", *J. Phys. Chem. A* **119**, 9506-9517 (2015).

[2] H. Kuramochi, S. Takeuchi, and T. Tahara, "Femtosecond Time-Resolved Impulsive Stimulated Raman Spectroscopy using Sub-7-fs Pulses: Apparatus and Applications", *Rev. Sci. Instrum.* **87**, 043107 (2016).

[3] D. W. McCamant, P. Kukura, S. Yoon, and R. A. Mathies, "Femtosecond Broadband Stimulated Raman Spectroscopy: Apparatus and Methods", *Rev. Sci. Instrum.* **75** (11), 4971-4980 (2004).

[4] M. Yoshizawa and M. Kurosawa, "Femtosecond Time-Resolved Raman Spectroscopy Using Stimulated Raman Scattering", *Phys. Rev. A* **61** (1), 013808 (1999).

[5] D. W. McCamant, P. Kukura, and R. A. Mathies, "Femtosecond Time-Resolved Stimulated Raman Spectroscopy: Application to the Ultrafast Internal Conversion in β-Carotene", *J. Phys. Chem. A* **107**, 8208-8214 (2003).

[6] P. Kukura, D. W. McCamant, S. Yoon, D. B. Wandschneider, and R. A. Mathies, "Structural Observation of the Primary Isomerization in Vision with Femtosecond-Stimulated Raman", *Science* **310**, 1006-1009 (2005).

[7] H. Kuramochi, S. Takeuchi, and T. Tahara, "Ultrafast Structural Evolution of Photoactive Yellow Protein Chromophore Revealed by Ultraviolet Resonance Femtosecond Stimulated Raman Spectroscopy", *J. Phys. Chem. Lett.* **3** (15), 2025-2029 (2012).

[8] D. R. Dietze and R. A. Mathies, "Femtosecond Stimulated Raman Spectroscopy", *ChemPhysChem* **17**, 1224-1251 (2016).

[9] J. Lee, J. R. Challa, and D. W. McCamant, "Ultraviolet Light Makes dGMP Floppy: Femtosecond Stimulated Raman Spectroscopy of 2′ -Deoxyguanosine 5′ -Monophosphate", *J. Phys. Chem. B* **121**, 4722-4732 (2017).

[10] C. Schnedermann, V. Muders, D. Ehrenberg, R. Schlesinger, P. Kukura, and J. Heberle, "Vibronic Dynamics of the Ultrafast all-trans to 13-cis Photoisomerization of Retinal in Channelrhodopsin-1", *J. Am. Chem. Soc.* **138**, 4757-4762 (2016).

[11] M. Quick, A. L. Dobryakov, I. N. Ioffe, A. A. Granovsky, S. A. Kovalenko, and N. P. Ernsting, "Perpendicular State of an Electronically Excited Stilbene: Observation by Femtosecond-Stimulated Raman Spectroscopy", *J. Phys. Chem. Lett.* **7**, 4047-4052 (2016).

[12] C. R. Hall, J. Conyard, I. A. Heisler, G. Jones, J. Frost, W. R. Browne, B. L. Feringa, and S. R. Meech, "Ultrafast Dynamics in Light-Driven Molecular Rotary Motors Probed by Femtosecond Stimulated Raman Spectroscopy", *J. Am. Chem. Soc.* **139**, 7408-7414 (2017).

[13] C. Fang, R. R. Frontiera, R. Tran, and R. A. Mathies, "Mapping GFP Structure Evolution during Proton Transfer with Femtosecond Raman Spectroscopy", *Nature*

462 (7270), 200-204 (2009).

[14] W. Wang, W. Liu, I.-Y. Chang, L. A. Wills, L. N. Zakharov, S. W. Boettcher, P. H.-Y. Cheong, C. Fang, and D. A. Keszler, "Electrolytic Synthesis of Aqueous Aluminum Nanoclusters and *in situ* Characterization by Femtosecond Raman Spectroscopy & Computations", *Proc. Natl. Acad. Sci. U.S.A.* **110** (46), 18397-18401 (2013).

[15] D. P. Hoffman and R. A. Mathies, "Femtosecond Stimulated Raman Exposes the Role of Vibrational Coherence in Condensed-Phase Photoreactivity", *Acc. Chem. Res.* **49** (4), 616-625 (2016).

[16] S.-Y. Lee, D. Zhang, D. W. McCamant, P. Kukura, and R. A. Mathies, "Theory of Femtosecond Stimulated Raman Spectroscopy", *J. Chem. Phys.* **121** (8), 3632-3642 (2004).

[17] W. Liu, L. Zhu, and C. Fang, "Observation of Sum-Frequency-Generation-Induced Cascaded Four-Wave Mixing Using Two Crossing Femtosecond Laser Pulses in a 0.1 mm Beta-Barium-Borate Crystal", *Opt. Lett.* **37** (18), 3783-3785 (2012).

[18] W. Liu, L. Zhu, L. Wang, and C. Fang, "Cascaded Four-Wave Mixing for Broadband Tunable Laser Sideband Generation", *Opt. Lett.* **38** (11), 1772-1774 (2013).

[19] W. Liu, F. Han, C. Smith, and C. Fang, "Ultrafast Conformational Dynamics of Pyranine during Excited State Proton Transfer in Aqueous Solution Revealed by Femtosecond Stimulated Raman Spectroscopy", *J. Phys. Chem. B* **116**, 10535-10550 (2012).

[20] L. Zhu, W. Liu, and C. Fang, "A Versatile Femtosecond Stimulated Raman Spectroscopy Setup with Tunable Pulses in the Visible to Near Infrared", *Appl. Phys. Lett.* **105** (4), 041106 (2014).

[21] L. Zhu, W. Liu, Y. Wang, and C. Fang, "Sum-Frequency-Generation-Based Laser Sidebands for Tunable Femtosecond Raman Spectroscopy in the Ultraviolet", *Appl. Sci.* **5** (2), 48-61 (2015).

[22] L. Zhu, W. Liu, and C. Fang, "Tunable Sideband Laser from Cascaded Four-Wave Mixing in Thin glass for Ultra-Broadband Femtosecond Stimulated Raman Spectroscopy", *Appl. Phys. Lett.* **103** (6), 061110 (2013).

[23] L. Zhu, S. Saha, W. Liu, Y. Wang, D. A. Keszler, and C. Fang, "Simultaneous Solution-Based Generation and Characterization of Crystalline Bismuth Thin Film by Femtosecond Laser Spectroscopy", *Appl. Phys. Lett.* **107** (6), 061901 (2015).

[24] F. Han, W. Liu, L. Zhu, Y. Wang, and C. Fang, "Initial Hydrogen-Bonding Dynamics of Photoexcited Coumarin in Solution with Femtosecond Stimulated Raman Spectroscopy", *J. Mater. Chem. C* **4** (14), 2954-2963 (2016).

[25] W. Liu, Y. Wang, L. Tang, B. G. Oscar, L. Zhu, and C. Fang, "Panoramic Portrait of Primary Molecular Events Preceding Excited State Proton Transfer in Water", *Chem. Sci.* **7** (8), 5484-5494 (2016).

[26] L. Tang, W. Liu, Y. Wang, L. Zhu, F. Han, and C. Fang, "Ultrafast Structural Evolution and Chromophore Inhomogeneity inside a Green-Fluorescent-Protein-Based Ca^{2+} Biosensor", *J. Phys. Chem. Lett.* **7** (7), 1225-1230 (2016).

[27] S. R. Tachibana, L. Tang, Y. Wang, L. Zhu, W. Liu, and C. Fang, "Tuning Calcium Biosensors with a Single-Site Mutation: Structural Dynamics Insights from Femtosecond Raman Spectroscopy", *Phys. Chem. Chem. Phys.* **19** (10), 7138-7146 (2017).

[28] W. Liu, L. Tang, B. G. Oscar, Y. Wang, C. Chen, and C. Fang, "Tracking Ultrafast Vibrational Cooling during Excited-State Proton Transfer Reaction with Anti-Stokes and Stokes Femtosecond Stimulated Raman Spectroscopy", *J. Phys. Chem. Lett.* **8** (5), 997-1003 (2017).

[29] B. G. Oscar, C. Chen, W. Liu, L. Zhu, and C. Fang, "Dynamic Raman Line Shapes on an Evolving Excited-State Landscape: Insights from Tunable Femtosecond Stimulated Raman Spectroscopy", *J. Phys. Chem. A* **121** (29), 5428-5441 (2017).

[30] R. M. Hochstrasser, "Two-Dimensional Spectroscopy at Infrared and Optical Frequencies", *Proc. Natl. Acad. Sci. U.S.A.* **104** (36), 14190-14196 (2007).

[31] B. G. Oscar, W. Liu, Y. Zhao, L. Tang, Y. Wang, R. E. Campbell, and C. Fang, "Excited-State Structural Dynamics of a Dual-Emission Calmodulin-Green Fluorescent Protein Sensor for Calcium Ion Imaging", *Proc. Natl. Acad. Sci. U.S.A.* **111** (28), 10191-10196 (2014).

Chapter 2 Ultrafast Optical Techniques

2.1 Introduction

Ultrafast spectroscopy is able to investigate molecular dynamics on their intrinsic timescales, which makes it very powerful in studying electronic and vibrational dynamics in the fields of photochemistry, photophysics, and photobiology. This clear advantage has made ultrafast spectroscopy one of the most active areas of modern physical chemistry, where ultrashort laser pulses can be used to observe and potentially control the outcome of reactions in real time.

The technological improvement of Ti:sapphire-based lasers in the early 1990s triggered the commercialization of ultrashort pulsed laser and made them relatively simple to use. The Ti : sapphire oscillators now produce 10–20 fs pulses routinely. The sub-10 fs pulses can be achieved using optimized configurations to compensate the temporal chirp in the pulse duration. Based on the commercially available laser source, various optical techniques have also been widely used to manipulate different parameters of laser pulses, such as the wavelength, bandwidth, pulse duration, etc. Regarding the ultrafast spectroscopic setups we have developed in the lab, a series of techniques have been implemented. In this chapter, we discuss the principles of several nonlinear optical techniques that have been employed to manipulate and characterize the pulses.

2.2 Supercontinuum generation

The nonlinear propagation of an ultrafast laser pulse leads to filamentation if the pulse is focused in a transparent material. The word filamentation means that the laser beam maintains a nearly constant beam waist over a certain distance, as a result of dynamic balance between Kerr self-focusing and plasma defocusing effects.[1,2] During this process, the pulse experiences changes in temporal, spatial, and spectral properties.

The condition of filamentation formation is satisfied when the incident beam power exceeds the critical power for self-focusing. The filament of an ultrashort laser pulse can produce a spectrally broadened pulse ranging from ultraviolet to infrared, or supercontinuum white light (SCWL). Since the first observation of SCWL in crystals and glasses in 1970,[3] SCWL has attracted intense research. The generation of supercontinuum has been demonstrated in a variety of materials, including solids, liquids and gasses.[4,5] Practically, SCWL generation in condensed bulk media is a user-friendly technique because it is compact, efficient, low cost, and robust with straightforward alignment. Moreover, the SCWL radiation bears high spatial and temporal coherence at various parts of the optical spectrum.[5] The SCWL beam preserves the same level of or even better spatial coherence as the input laser beam due to spatial mode cleaning effect,[6,7] which gives the beam excellent focusability. The high temporal coherence of SCWL arises from a well-defined temporal structure of femtosecond (fs) filament. The SCWL pulses typically acquire a regular chirp due to material dispersion and hence exhibit good compressibility.[8]

Typical SCWL spectra using fs Ti: sapphire laser from three media are shown in Figure 2.1.

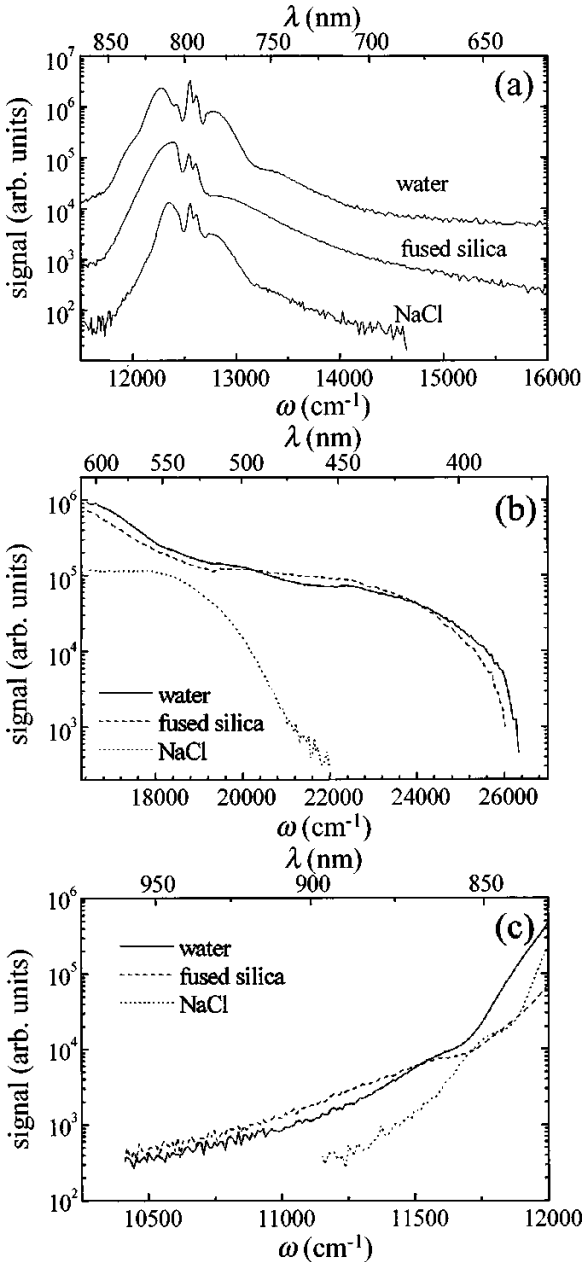

Figure 2.1 Typical white-light continuum spectra generated in water, UV-grade fused silica, and NaCl in the red to near-infrared region. The intense spectral components around the laser

wavelength are suppressed with a RG850 color filter. All spectra are corrected for filter, CCD, and grating responses.[5]

As a result, SCWL has been widely used in many fields: for example, it is extremely useful as the probe pulse in all kinds of ultrafast time-resolved spectroscopic measurements; it is also an ideal seed pulse in an optical parametric amplifier (OPA) system. During SCWL generation, self-focusing effect may lead to the beam breaking up into multiple filaments which could make the SCWL unstable. It is hence the crucial to control the incident laser pulse power such that SCWL is generated without producing multiple filaments. For a sub 100-fs pulse, this means that the pulse energy must be limited to approximately 1 μJ.

A typical setup of SCWL is depicted in Figure 2.2. In short, a 800 nm fundamental beam from a mode-locked fs Ti:sapphire laser goes through an iris and a neutral density filter to select out a part of the beam that has good spatial quality and proper intensity. Then beam is then focused via a lens onto a wide-bandgap dielectric material such as sapphire plate or calcium fluoride plate, where SCWL is generated. After a collimation lens, the center part of SCWL is picked out by a second iris and ready to be applied to different optical systems.

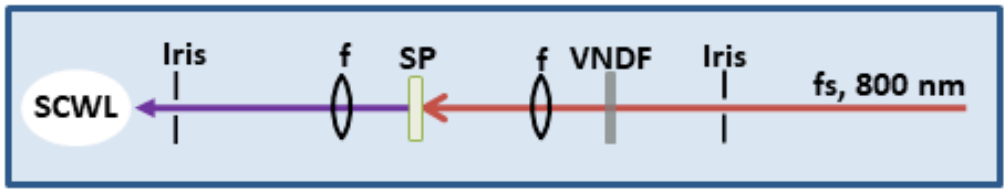

Figure 2.2 Scheme for supercontinuum white light (SCWL) generation.

VNDF: variable neutral density filter; f: lens; SP: sapphire plate. The SCWL pulse duration is larger than the incident fs pulse due to the commonly positive chirp introduced by glass materials the light traverses. Both the SP and the second lens f are mounted on translation stages after the incident beam (red) hits the transparent medium, which enables the fine tuning of SCWL properties from intensity, spectral coverage and shape, chirp, etc.

2.3 Optical parametric amplifier (OPA)

The spectroscopic study of photochemistry requires a tunable coherent source of high-power or high-energy radiation as well as a broad wavelength tuning range to be applicable to many systems. The OPA technique, which provides high output energies, broad frequency tunability and simplicity to operate, makes it a reliable laser source for the task. In 1965, the first tunable optical parametric oscillator was demonstrated.[9] Over the years, with improvements in materials and laser pump sources, this technique has been greatly developed. Nowadays, commercially available OPA systems could match a variety of ultrashort pulse laser sources[10] and produce picosecond and femtosecond pulses that are broadly tunable from 0.2 up to 20 μm.[11,12]

The principle of OPA in a suitable nonlinear crystal is as follows. A higher frequency and higher intensity beam, known as the pum, at frequency ω_p, amplifies a lower frequency, lower intensity beam, called the signal, at frequency ω_s. Meanwhile a third beam, named the idler beam, at frequency ω_i is generated. In this process, energy conservation relation

$$\hbar\omega_p = \hbar\omega_s + \hbar\omega_i \qquad (2.3.1)$$

is satisfied; meanwhile, the momentum conservation relation, or phase-matching condition

$$\hbar\boldsymbol{k}_p = \hbar\boldsymbol{k}_s + \hbar\boldsymbol{k}_i \qquad (2.3.2)$$

must be satisfied, where $\boldsymbol{k}_\mathrm{p}$, $\boldsymbol{k}_\mathrm{s}$, and $\boldsymbol{k}_\mathrm{i}$ are the wave vectors of pump, signal, and idler, respectively. In an OPA, the energy flows from a high-power pump beam to a low-power signal beam, generating a third idler beam as well. The pump beam, in this process, needs

to be very high intensities (order of tens of GW/cm^2) to be efficient, which can be readily achieved by femtosecond laser systems.

We can use coupled nonlinear equations to describe the OPA process. If neglecting pump depletion and assuming perfect phase matching, the parametric gain can be solved as growing exponentially with the crystal length L and the coefficient Γ:

$$\mathrm{G} = \frac{1}{4} e^{2\Gamma L} \qquad (2.3.3)$$

where coefficient Γ depends on the pump intensity, signal and idler wavelengths, the nonlinear coefficient of crystal and the refractive indexes at the three interacting wavelengths. Even though it seems that longer crystal gives higher gain, this relation does not hold when considering ultrashort pulses. For a femtosecond OPA, three pulses with different wavelengths propagates in the nonlinear crystal with different group velocities. Therefore, in the presence of group velocity mismatch (GVM), the effective length of crystal is

$$L_{eff} = \frac{\tau}{\delta} \qquad (2.3.4)$$

where τ is pump pulse duration and δ is the GVM between pump and signal/idler. In other words, the shorter the pulse, the thinner the crystal should be. GVM between signal and idler also limits the phase matching bandwidth.

Such a limitation of bandwidth can be overcome when an additional degree of freedom is introduced using a noncollinear geometry. Instead of traveling in the same direction, the

aforementioned three beams have small angles between each other. Broadband phase matching can be achieved for a signal-idler angle that the signal group velocity equals the projection of the idler group velocity along the signal direction. The experimental scheme of an ultra-broadband noncollinear OPA (NOPA) is shown in Figure 2.3.

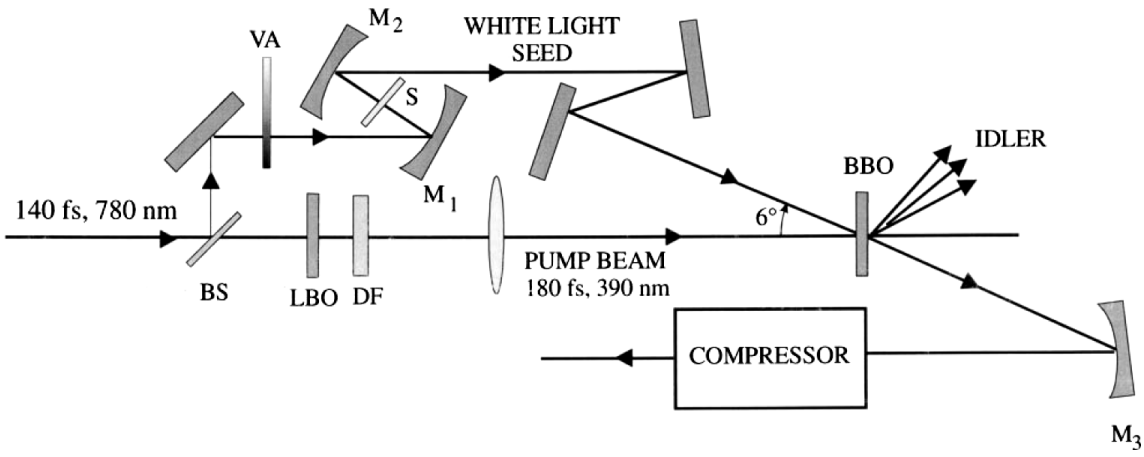

Figure 2.3 Scheme of a fs noncollinear OPA in the visible region.

BS: beam splitter; VA: variable attenuator; S: 1-mm-thick sapphire plate; DF: dichroic filter; M1 , M2 , M3 , spherical mirrors; LBO, lithium triborate crystal; BBO, beta-barium borate crystal. The signal after the BBO is reflected by M_3 into a compressor to reduce the temporal chirp of the signal pulse.[13]

2.4 Second harmonic bandwidth compression

Since many spectroscopic setups are based on femtosecond Ti:sapphire laser, people have started to face a paradox that a reliable laser source with a few picoseconds duration is harder to obtain than that with a duration of 100 fs or less. Moreover, in the FSRS experiment, synchronization between two fs pulses and a narrowband ps pulse is necessary. A method originates from radar technology has been introduced to generate coherent narrowband ps pulses starting from broadband fs pulses. The idea is to mix pulses with opposite chirps,[14,15] which is called second harmonic bandwidth compression (SHBC) when the mixing occurs in a second harmonic generation scenario.[16,17]

Simply speaking, a thick crystal can produce narrowband harmonics from short broadband pulses. However, there are two drawbacks: low efficiency and low stability because other nonlinear effects may occur in the same nonlinear medium. In contrast, SHBC achieves high efficiency and stability wherein in an ideal case, two input pulses are linearly chirped with opposite temporal chirps,

$$\omega_1(t) = \omega_0 + \alpha t \qquad (2.4.1)$$

$$\omega_2(t) = \omega_0 - \alpha t \qquad (2.4.2)$$

where α is a constant. In this scenario, the sum frequency is constant

$$\omega_s(t) = 2\omega_0 \qquad (2.4.3)$$

The output bandwidth to first order approximation is as narrow as the inverse of the chirped-pulse duration because the blue (red) edge of one beam meets the red (blue) edge of the other beam in the BBO crystal for SHG (e.g., generating a ps 400 nm pulse).

A typical SHBC setup is shown in Figure 2.4. A ~100 fs pump pulse, centered near 800 nm, with 180 cm^{-1} FWHM bandwidth, is split into two equal portions. Each pump pulse is temporally chirped using what is essentially the front half of a 4*f* pulse shaper with a retro-reflecting mirror placed at the Fourier plane. The pulse shapers share a common diffraction grating (inward and outward with a compact folding geometry) and utilize two separately positioned but identical cylindrical lenses of focal length *f*. Each pulse experiences two reflections from the grating. Phase-conjugate temporal chirps are introduced to the pumps by adjusting the distance, L, between the lenses and the grating to $L_+ = f - \delta$ for positive chirp, and $L_- = f + \delta$ to obtain an equal amount of negative chirp (δ is the offset from focal point). Sum frequency generation of the two incident beams with opposite chirps in BBO delivers a 3.5 cm^{-1} linewidth, 5.4 ps pulse-duration beam centered at 400 nm.[18]

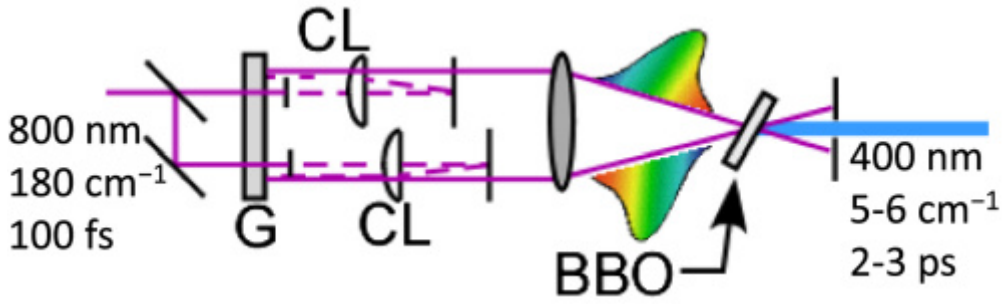

Figure 2.4 SHBC schematic setup.

Dashed lines indicate beam paths internal to the pulse stretchers. G: grating; CL: cylindrical lens. BBO: beta-barium-borate crystal.[18] Copyright 2013 Optical Society of America.

2.5 Ultrafast pulse compression

Short laser pulses have proved their importance in advancing various technologies, they also provide an excellent tool for studying physical or chemical processes occurring on very fast time scales, including all kinds of ultrafast spectroscopy. In signal generation, amplification and propagation of fs pulses with dispersion compensation plays a key role. Pulse compression and dispersion control are indispensable for the improvement of most of the desired applications of ultrafast lasers. In this section we briefly review the commonly used dispersive devices for pulse including grating and prism pairs as well as chirped mirrors.

In any medium, pulses will naturally be broadened due to dispersion (the dependence of the refractive index on wavelength). The mechanism of this broadening can be explained using the concept of group velocity. The group velocity of a wave is the velocity with which the overall shape of the waves' amplitudes (envelope of the wave) propagates through space. The group velocity v_g is defined by the equation:

$$v_g = \frac{d\omega}{dk} \qquad (2.5.1)$$

Where ω is angular frequency and k is the wavevector. If ω is not a linear function of k, the envelope of a wave packet will become distorted as it travels. The variation of group velocity with frequency can be given (via Taylor expansion of the k-vector phase) by:

$$k''(\omega) = \frac{d}{d\omega}\left[\frac{1}{v_g}\right] = \frac{\lambda_0^3}{2\pi c_0^2}\frac{d^2 n}{d\lambda_0^2} \qquad (2.5.2)$$

This term is named group velocity dispersion (GVD) with the unit of (time^2/distance), commonly expressed in fs^2/mm. A related term called group delay dispersion (GDD) is the product of GVD and medium length L, thus having the typical unit of fs^2. Most of the materials have positive GVD terms in the visible to near-IR regions. As a result, the redder portion of the transmitted light usually has larger group velocity, while bluer portion has smaller group velocity (i.e., the red precedes the blue component). Note that ultrafast laser pulses have ultrabroad bandwidth, so the broadening effect due to GVD can be dramatic which hinder applications such as ultrafast molecular spectroscopy. To address this issue, pulse compression techniques have been introduced.

A widely used method is to manipulate angular dispersion so that this device has controllable negative GVD. In consequence, it can compensate for the positive chirp arising from ultrafast light propagation through materials.

A parallel grating pair pulse compressor was demonstrated by Treacy in 1969.[19] As shown in Figure 2.5, since the path length for λ_L is greater than that for λ_S the longer wavelength (redder) components experience a greater group delay (negative GVD), which is opposite to that from normal materials. Later in 1987, this design was improved by Martinez using a grating-lens model.[20]

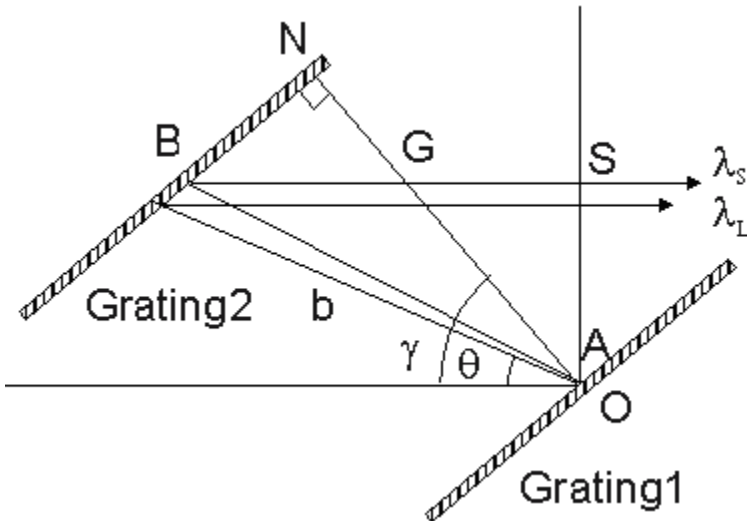

Figure 2.5 Geometrical arrangement of diffraction gratings used for pulse compression. The angle of incidence is γ (to the surface normal), and θ is the angle between the incident and diffracted rays. The paths are shown for two wavelength components with $\lambda_L > \lambda_S$.[19] The larger the separation between the two gratings, the larger the negative GDD. Copyright 1969 IEEE.

Similar function can also be realized by using Brewster-angled prisms (see Figure 2.6).[21] When comparing to the grating counterparts, the prism separation and insertion can be easily adjusted in space, which means that the compression parameters can be better controlled.[22,23] In principle, only the GDD due to dispersion was considered to be the main factor here, not the GDD due to the prism (typically glass material) itself. This is because the negative GDD due to prism angular dispersion is usually much greater than that from the transparent material of the prism. To reduce the required separation between prisms for effective pulse compression, highly dispersive glass such as SF10 and Suprasil is used.

In our setup, we use a two-prism pulse compressor and let the input and output laser pulses travel through each prism twice (forward and backward) by using a folding mirror (or a roof mirror). We can finely adjust the inter-prism distance with a footprint half the size of the four-prism pulse compressor in Figure 2.6, and reduce the optical alignment issues which may introduce spatial chirps, beam magnification, and pulse front tilt, etc. The principle stands the same and we have achieved pulse compression typically to the 20—30 fs range for our ultrafast electronic and vibrational spectroscopic measurements detailed in subsequent chapters in this thesis.

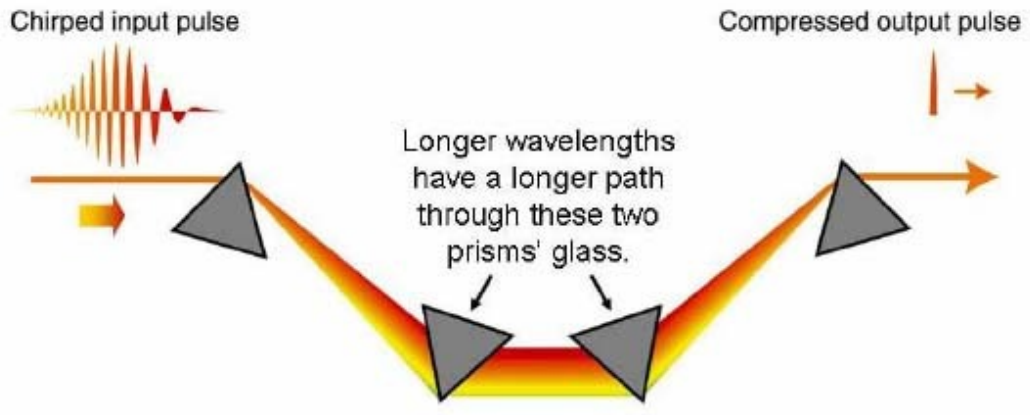

Figure 2.6 Prism pulse compressor.[24]

Because angular dispersion introduces negative chirp, it compensates for the positive chirp accumulated by the light pulse travelling through non-absorbing material. All the incident angles on prisms should be identical. When optimized by adding or subtracting glass from the beam path without altering the output beam direction, a chirped input pulse can emerge from the other side unchirped (i.e., well compressed). Copyright 2006 Optical Society of America.

Although grating and prism pairs have been successfully used as laser pulse compressor, they suffer from higher order dispersion, spatial chirps, large size and difficulty in everyday alignment. A more compact and user-friendly method is chirped mirrors (CM), which are dispersive multilayer structures designed for pulses compression (see Figure 2.7).[25] CM is able to provide dispersion without much material or a large footprint in the beam path so they avoid the undesirable spatiotemporal effects typically encountered in the prism compression system (Figure 2.6). The CM can precisely control GVD (nearly linear with the designed incident light wavelength range) or even some higher order dispersion. The high reflectivity with appropriate anti-reflective optical coating (to allow for light penetration into the CM structure above the substrate) in a broadband wavelength range makes CM an appealing key component for extremely short pulse compression.[26] More and more ultrafast spectroscopy groups have adopted CM as the main pulse compressor.

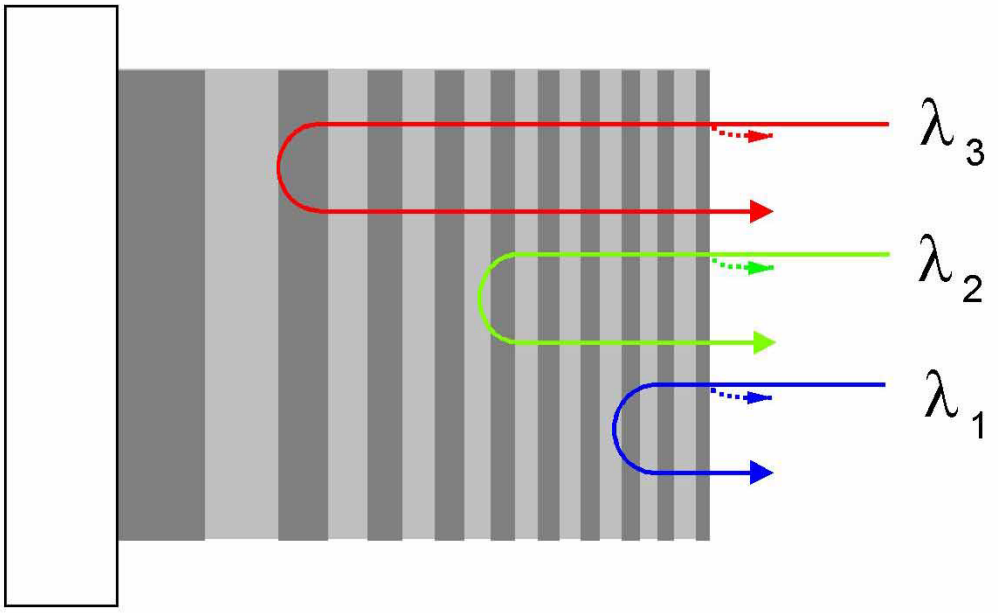

Figure 2.7 Schematic representation of a chirped mirror.

The frequency dependence of the group velocity delay experienced by a broadband pulse upon reflection off a CM can be controlled by means of the penetration depth of different spectral components in the multilayer, $\lambda_1 < \lambda_2 < \lambda_3$ (i.e., red components penetrate the deepest on the typical few μm range).[27]

2.6 References

[1] J. E. Sharping, M. A. Foster, A. L. Gaeta, J. Lasri, O. Lyngnes, and K. Vogel, "Octave-Spanning, High-Power Microstructure-Fiber-Based Optical Parametric Oscillators", *Opt. Express* **15** (4), 1474-1479 (2007).

[2] S. Tzortzakis, L. Sudrie, M. Franco, B. Prade, A. Mysyrowicz, A. Couairon, and L. Berge, "Self-Guided Propagation of Ultrashort IR Laser Pulses in Fused Silica", *Phys. Rev. Lett.* **87** (21), 213902 (2001).

[3] R. R. Alfano and S. L. Shapiro, "Emission in the Region 4000 to 7000 A Via Four-Photon Coupling in Glass", *Phys. Rev. Lett.* **24** (11), 584-587 (1970).

[4] A. Brodeur and S. L. Chin, "Band-Gap Dependence of the Ultrafast White-Light Continuum", *Phys. Rev. Lett.* **80** (20) (1998).

[5] A. Brodeur and S. L. Chin, "Ultrafast White-Light Continuum Generation and Self-Focusing in Transparent Condensed Media", *J. Opt. Soc. Am. B* **16** (4) (1999).

[6] W. Watanabe and K. Itoh, "Spatial Coherence of Supercontinuum Emitted from Multiple Filaments", *Jpn. J. Appl. Phys.* **40** (21), 592-595 (2001).

[7] M. F. B. Prade, A. Mysyrowicz, A. Couairon, H. Buersing, B. Eberle, M. Krenz, D. Seiffer, and O. Vasseur, "Spatial Mode Cleaning by Femtosecond Filamentation in Air", *Opt. Lett.* **31**, 2601-2603 (2006).

[8] D. B. D. Wegkamp, S. Bonora, G. Cerullo, J. St¨ahler, M. Wolf, and S. Wall, "Phase Retrieval and Compression of Low-Power White-Light Pulses", *Appl. Phys. Lett.* **99**, 101101 (2011).

[9] J. A. Giordmaine and R. C. Miller, "Tunable Coherent Parametric Oscillation in $LiNbO_3$ at Optical Frequencies", *Phys. Rev. Lett.* **14**, 973 (1965).

[10] A. Piskarskas, "Optical Parametric Generators: Tunable, Powerful, Ultrafast", *Opt. Photon. News* **7** (7), 25-28 (1997).

[11] R. Danielius, A. Piskarskas, A. Stabinis, G. P. Banfi, P. Di Trapani, and R. Righini, "Traveling-Wave Parametric Generation of Widely Tunable, Highly Coherent Femtosecond Light Pulses", *J. Opt. Soc. Am. B* **10** (11), 2222-2232 (1993).

[12] G. Cerullo and S. D. Silvestri, "Ultrafast Optical Parametric Amplifiers", *Rev. Sci. Instrum.* **74** (1), 1-16 (2003).

[13] A. Shirakawa and T. Kobayashi, "Noncollinearly Phase-Matched Femtosecond Optical Parametric Amplification with a 2000 cm^{-1} Bandwidth", *Appl. Phys. Lett.* **72** (2), 147-149 (1998).

[14] G. Veitas and R. Danielius, "Efficient Generation of <3-cm^{-1} Bandwidth Mid-IR Pulses by Difference-Frequency Mixing of Chirped Pulses", *J. Opt. Soc. Am. B* **19** (6), 1411 (2002).

[15] H. Luo, L. Qian, P. Yuan, and H. Zhu, "Generation of Tunable Narrowband Pulses Initiating from a Femtosecond Optical Parametric Amplifier", *Opt. Express* **14** (22), 10631 (2006).

[16] S. Laimgruber, H. Schachenmayr, B. Schmidt, W. Zinth, and P. Gilch, "A Femtosecond Stimulated Raman Spectrograph for the Near Ultraviolet", *Appl. Phys.*

B **85** (4), 557-564 (2006).

[17] F. Raoult, A. C. L. Boscheron, D. Husson, C. Sauteret, A. Modena, V. Malka, F. Dorchies, and A. Migus, "Efficient Generation of Narrow-Bandwidth Picosecond Pulses by Frequency Doubling of Femtosecond Chirped Pulses", *Opt. Lett.* **23** (14), 1117-1119 (1998).

[18] S. P. Kearney and D. J. Scoglietti, "Hybrid Femtosecond/Picosecond Rotational Coherent Anti-Stokes Raman Scattering at Flame Temperatures using a Second-Harmonic Bandwidth-Compressed Probe", *Opt. Lett.* **38** (6), 833-835 (2013).

[19] E. B. Treacy, "Optical Pulse Compression with Diffraction Gratings", *IEEE J. Quantum Electron.* **QE-5** (9), 193-196 (1969).

[20] O. E. Martinez, "3000 Times Grating Compressor with Positive Group Velocity Dispersion: Application to Fber Compensation in 1.3-1.6 μm Region", *IEEE J. Quantum Electron.* **QE-23** (1), 59-64 (1987).

[21] R. L. Fork, O. E. Martinez, and J. P. Gordon, "Negative Dispersion Using Pairs of Prisms", *Opt. Lett.* **9** (2), 150-152 (1984).

[22] K. Naganuma and K. Mogi, "50-fs Pulse Generation Directly From a Colliding-Pulse Mode-Locked Ti:Sapphire Laser Using an Antiresonant ring Mirror", *Opt. Lett.* **16** (10), 738-740 (1991).

[23] Z. Zhang and T. Yagi, "Observation of Group Delay Dispersion as a Function of the Pulse Width in a Mode Locked Ti:Sapphire Laser", *Appl. Phys. Lett.* **63** (22), 2993 (1993).

[24] S. Akturk, X. Gu, M. Kimmel, and R. Trebino, "Extremely Simple Single-Prism Ultrashort-Pulse Compressor", *Opt. Express* **14** (21), 10101-10108 (2006).

[25] F. X. Kärtner, N. Matuschek, T. Schibli, U. Keller, H. A. Haus, C. Heine, R. Morf, V. Scheuer, M. Tilsch, and T. Tschudi, "Design and Fabrication of Double-Chirped Mirrors", *Opt. Lett.* **22** (11), 831-833 (1997).

[26] V. Pervak, S. Naumov, G. Tempea, V. Yakovlev, F. Krausz, and A. Apolonski, "1.5-Octave Chirped Mirror for Pulse Compression Down to Sub-3 fs", *Appl. Phys. B* **87** (1), 5-12 (2007).

[27] P. Dombi, V. S. Yakovlev, K. O'Keeffe, T. Fuji, M. Lezius, and G. Tempea, "Pulse Compression with Time-Domain Optimized Chirped Mirrors", *Opt. Express* **13** (26), 10888-10894 (2005).

Chapter 3 Tunable Sideband Laser from Cascaded Four-Wave Mixing in Thin Glass for Ultra-Broadband Femtosecond Stimulated Raman Spectroscopy

Liangdong Zhu, Weimin Liu, and Chong Fang*

Applied Physics Letters, **103** (6), 061110, published online August 7, 2013 DOI: 10.1063/1.4817915

3.1 Abstract

We demonstrate the generation of broadband up-converted multicolor array (BUMA) in a thin BK7 glass slide using two noncollinear weak near-IR laser pulses with various crossing angles. The BUMA signal arises from cubic nonlinear $\chi^{(3)} : \chi^{(3)}$ processes via cascaded four-wave mixing of the two incident beams. Broad and continuous tunability of BUMA is simply achieved by varying the time delay between the two pulses. We implement one of the BUMA sidebands as the probe pulse for femtosecond stimulated Raman spectroscopy and collect a solvent mixture anti-Stokes Raman spectrum with an ultrabroad detection range of ca. 100—4000 cm^{-1}.

3.2 Introduction

Ultrafast spectroscopy is a powerful technique to study electronic and vibrational dynamics in the fields of photochemistry, photophysics, and photobiology.[1-5] To investigate molecular dynamics on their intrinsic timescales, i.e., femtoseconds (fs) to picoseconds (ps), the laser pulses utilized must have shorter duration than the response time of the dynamics of interest. Therefore, ultrabroad wavelength-tunable laser pulses with duration less than 20 fs (i.e., a typical chemical bond vibrational period) are extremely useful. The noncollinear optical parametric amplification (NOPA) with $\chi^{(2)}$-based second harmonic generation is one of the dominant ways to generate tunable fs lasers.[6] In another approach using two crossing fs laser pulses in various optically anisotropic and isotropic media, a

multicolor angularly separated array from UV to near IR was obtained from the $\chi(3)$-based cascaded four-wave mixing (CFWM) processes.[7-12] The wavelength tunability was achieved via changing the crossing angle (α) between the two incoming beams. Recently, we have demonstrated a convenient and versatile method to generate tunable multicolor lasers in a thin anisotropic medium such as BBO by two weak near-IR beams.[11,13] Broadband frequency up-converted multicolor array (BUMA) signals from 350 to 800 nm are readily tuned through varying the time delay between an 800 nm fundamental pulse (FP) and a positively chirped near-IR pulse, or rotating the crystal to achieve various phase-matching conditions (PMCs).[13]

In this Letter, based on our previous work,[11,13] we demonstrate a more flexible and cost-effective approach to generate BUMA sideband lasers in a thin (0.15 mm thickness) BK7 glass slide. The main difference from literature on amorphous materials is that, (a) our BUMA signals arise from two weak near-IR pulses from commercially available fs laser amplifiers; (b) wavelength tunability is achieved by simply varying the time delay between the two incident pulses; (c) ultrabroad bandwidth (ca. 1000—1600 cm^{-1}) is obtained. We implement the first-order sideband as the probe pulse in femtosecond stimulated Raman spectroscopy (FSRS) with a narrowband 800 nm Raman pump,[14-17] and successfully collect the anti-Stokes Raman spectrum of an organic solvent mixture spanning the ultrabroad frequency range of 100—4000 cm^{-1}.

3.3 Experimental setup

The experimental setup for BUMA generation[13] is depicted in Figure 3.1b. In brief, ~50 mW of the 800 nm fundamental output with 35 fs pulse duration and 1 kHz repetition rate from a mode-locked Ti:sapphire laser amplifier (Coherent Legend Elite) is split into two parts by a beamsplitter. About 10 μJ of the FP is focused onto a 2-mm-thick sapphire plate to generate a super-continuum white light (SCWL); its near-IR part (>810 nm, ~200 nJ/pulse) is selected with a longpass filter. The other FP arm is attenuated by an iris and a variable neutral density filter to ~8 μJ/pulse. The two beams are loosely focused by an f=10 cm concave mirror on a 150-μm-thick BK7 glass slide. The diameters of both beams on the glass surface are ~200 μm (near normal incidence). The crossing angle is tuned 2—10° using a reflective mirror on a translation stage. The wavelengths of different-order sidebands are measured by an Ocean Optics spectrometer. For FSRS, we use a home-built spectral filter consisting of a 1200 grooves/mm, 750 nm blaze reflective diffraction grating and a ~90 μm width mechanical slit to generate the Raman pump (~10 cm^{-1} bandwidth and ~3.5 ps pulse duration).[15] The first-order BUMA sideband is selected and made noncollinear with the Raman pump before being focused on the 5-mm-thick quartz sample cell by an f=10 cm fused silica lens. After the solvent sample, the probe beam carrying the stimulated Raman signal is re-collimated and focused into the spectrograph with a 600 grooves/mm, 1000 nm blaze grating. The dispersed signal is collected by a CCD camera (Princeton Instruments, PIXIS 100F), synchronized with the laser to achieve shot-to-shot spectral acquisition.

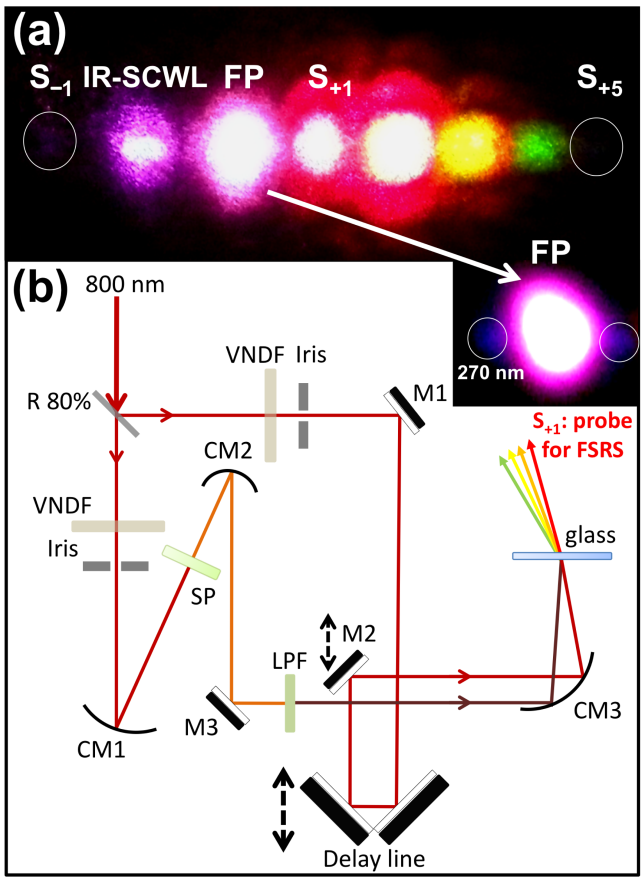

Figure 3.1 BUMA generation scheme. (a) Photograph of the CFWM signals generated in a 0.15-mm-thick BK7 glass slide. Up to five BUMA laser sidebands can be observed on the stronger FP side. (b) Schematic of the experimental setup. CM1–3 are Ag-coated concave mirrors, M1–3 are plane mirrors, VNDF is variable neutral density filter (OD=0–2), SP is 2-mm-thick *Z*-cut sapphire crystal plate, and LPF is longpass filter. The photograph of the UV sidebands on both sides of FP is shown as an inset.

When the FP and IR-SCWL pulse are temporally and spatially overlapped on the thin BK7 glass, cascaded multicolor sidebands emerge on the FP side Figure 3.1a: five frequency up-converted sidebands are identified with good spatial separation. Only one frequency down-converted sideband appears on the SCWL side due to its weak energy (~0.2 μJ/pulse), and the rapid increase of the wavevector mismatch with the beam order, leading to the observed asymmetry.[9,10] The Figure 3.1a inset shows an enlarged photograph of the FP spot past the glass, and two satellite laser spots manifest on both sides of FP. Their center wavelength are measured to be ~270 nm, possibly due to third-harmonic generation processes occurring on the glass-air interface because bulk glass strongly absorbs UV light.[18] Characterization of these UV sidebands has been reported later that year.[19]

3.4 Characterization of sidebands

For CFWM processes, the multicolor sideband signals generated by the FP and SCWL pulse are determined by the energy conservation relation: $\omega_{+m} = (m+1)\omega_1 - m\omega_2$, and the PMC: $\vec{k}_{+m} = (m+1)\vec{k}_1 - m\vec{k}_2$ where m=1, 2... is the beam order, $\vec{k}_{+m}, \vec{k}_1 \; and \; \vec{k}_2$ are the wavevectors of the sideband, FP, SCWL, respectively. The crossing angle α-dependent wavevector magnitude of the up-converted sidebands according to noncollinear geometrical PMCs is given by[9,11]

$$k_{+m} = \left\{ \left[(m+1)k_1 + mk_2 \right]^2 - 4m(m+1)k_1 k_2 \cos^2\left(\frac{\alpha}{2}\right) \right\}^{\frac{1}{2}} \qquad (3.1)$$

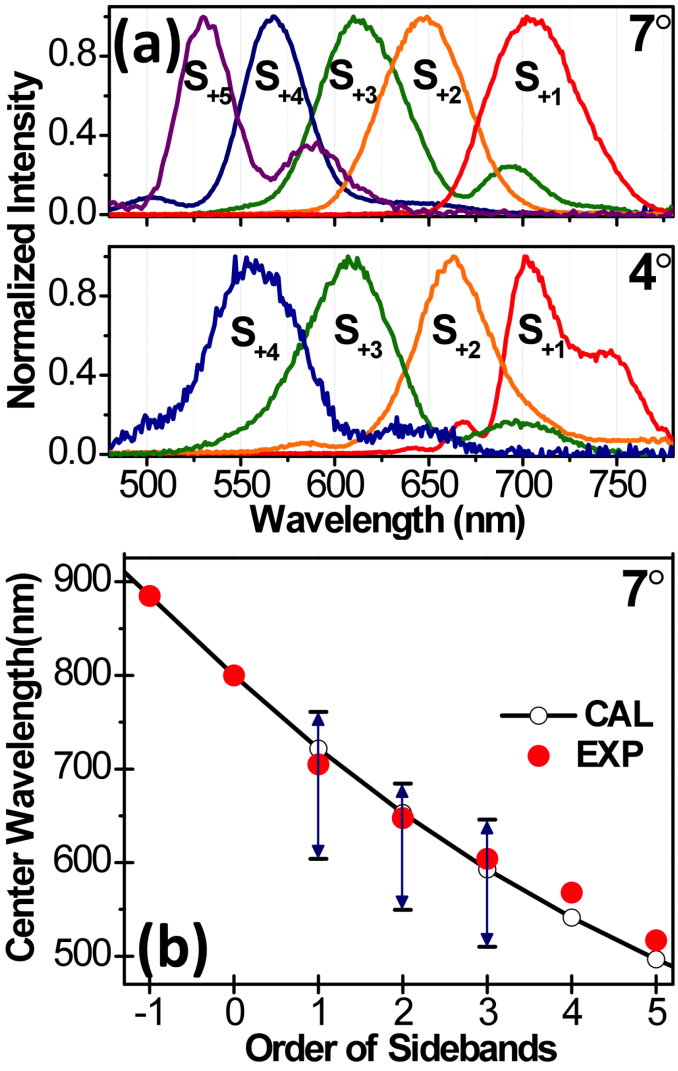

Figure 3.2 BUMA spectra and tunability. (a) Normalized spectra of the generated BUMA sidebands in BK7 glass with crossing angles of 7° and 4° between the two incident beams. They are labeled as S_{+i} (i=1, 2, 3 …), and i is the beam order. (b) Center wavelengths of different orders of CFWM sidebands: red filled circles, experimental data; open circles, calculation results based on the interacting 800 nm FP and the 880 nm component of the IR-SCWL pulse with a crossing angle of 7°. The broadband tunability of the first three sidebands is represented by double-arrowed vertical lines.

The normalized spectra of the BUMA signals generated at α=7° and 4° are shown in Figure 3.2a. In contrast to previous reports,[9,20,21] these sidebands all have ultrabroad bandwidth (>1000 cm^{-1}), corresponding to the Fourier transform-limited pulse duration of <15 fs if assumed Gaussian pulse shape. We attribute the BUMA observation to (1) the broadband incident pulses, particularly the SCWL, that support PMC at each cascaded step using the appropriate wavelength component; (2) the thinness of transparent medium that guarantees small enough material dispersion; and (3) an optimized crossing angle wherein the PMCs are satisfied over a broad bandwidth for BUMA generation.[22] Figure 3.2b shows the calculated BUMA wavelengths at α=7° from Eq. (3.1), with the SCWL center wavelength set at 880 nm that experimentally achieves the brightest BUMA signals. This is calibrated by replacing the glass slide with a 0.1-mm-thick BBO crystal (type I, θ=27.8˚), and measuring the wavelength of the sum frequency generation (SFG) signal *in situ* (see below). The figure shows good consistency between theory and experimental data.

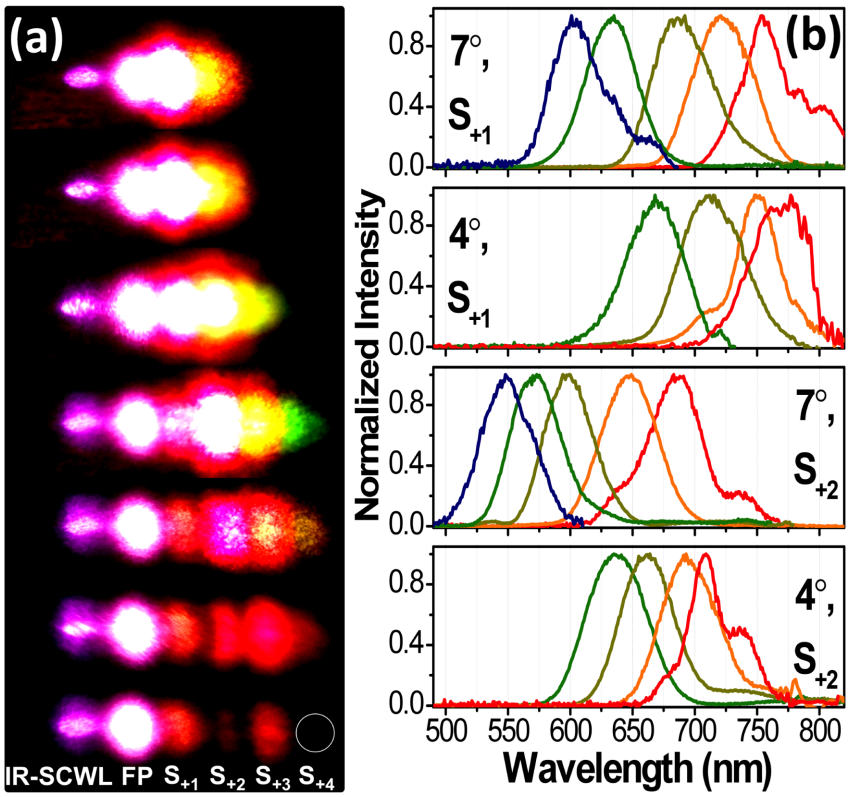

Figure 3.3 The experimentally achieved BUMA tunability (a) Photographs of the BUMA signals at different time delay between the fundamental and IR-SCWL pulses with a crossing angle of 4°. Beams are labeled at the bottom. (b) Normalized S_{+1} and S_{+2} spectra at different time delay with the crossing angles of 7° and 4°, respectively. The sideband tunability is crossing-angle-dependent while maintaining the broad bandwidth.

A notable feature in augmenting BUMA application potentials is the broadband tunability, denoted by double-arrowed lines in Figure 3.2b for S_{+i} (i=1–3). It is readily achieved by varying the time delay between the two incident pulses. Figure 3.3a shows time-dependent BUMA photographs with α=4°, accompanied by continuous and transverse change of the sideband angular dispersion. This represents a convenient way to separate out the desired sideband laser for spectroscopic implementation in the desirable background-free condition. Figure 3.3b shows the normalized spectra of the first (S_{+1}) and second-order (S_{+2}) sidebands with α=7° and 4° within ~150 fs delay time between FP and SCWL. The S_{+1} integrated intensity shows a temporal profile with ~80 fs fwhm (results not shown), consistent with the cross correlation between FP and SCWL in a 0.1-mm-thick BBO crystal.[13] The S_{+1} sideband at 7° is tunable from ~580 to 780 nm, while the higher-order S_{+2} manifests a blueshifted tunable range of ca. 500—720 nm. At α=4° and 10° (data not shown), fewer sidebands and narrower tunability are observed, which means an experimentally optimal crossing angle exists for effective BUMA generation.. The 7° crossing angle is larger than the optimized interaction angle of 2.9° found in a similar BK7 glass.[9] In difference from the 618 and 561 nm visible pulses used therein, we employ two broadband near-IR pulses that likely contribute to the different optimized crossing angle observed here.[23]

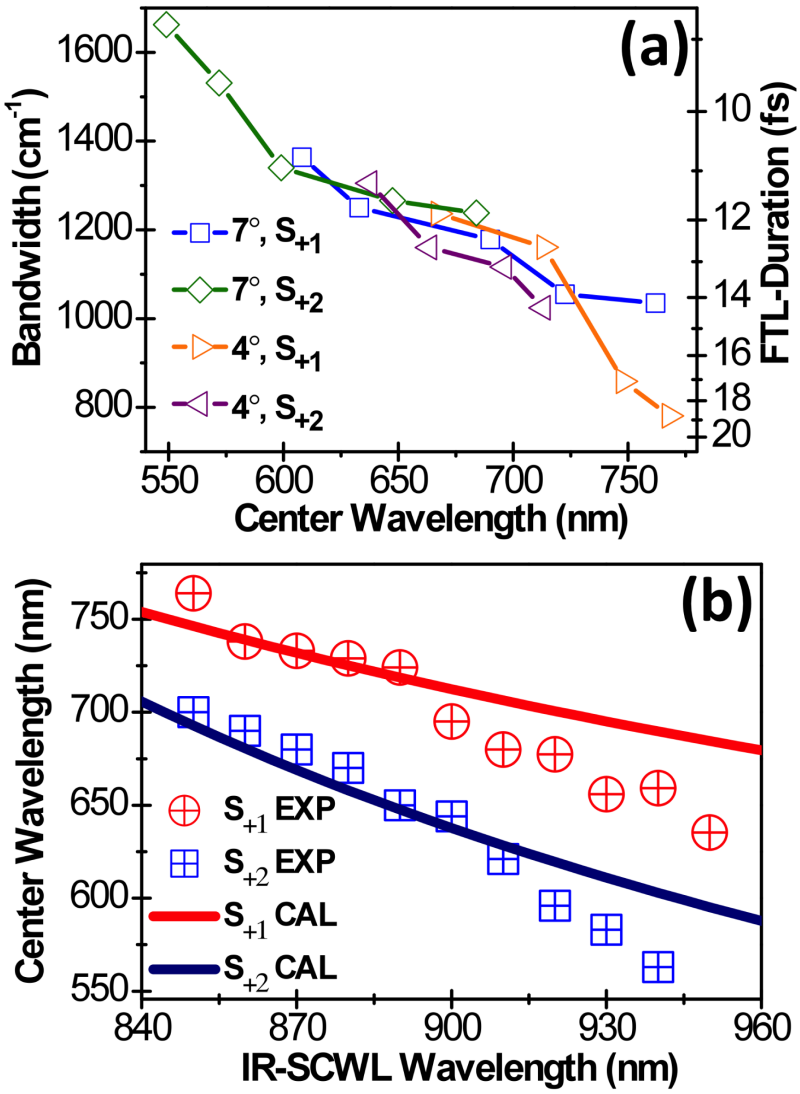

Figure 3.4 BUMA bandwidth and center wavelength (a) Bandwidths of the delay-time-dependent S_{+1} and S_{+2} spectra shown in Figure 3.3b versus their center wavelength at each time delay. The corresponding Fourier transform-limited time duration is plotted on the right axis. (b) Center wavelengths of S_{+1} and S_{+2} sidebands versus various spectral components of the positively chirped IR-SCWL pulse interacting with the 35 fs FP in the thin glass. Red circles (S_{+1}) and blue squares (S_{+2}): experimental data; solid lines: calculation results.

The bandwidths of time-dependent S_{+1} and S_{+2} signals at α=7° and 4° within 150 fs time delay are plotted in Figure 3.4a. These sideband lasers can be continuously tuned from 500 to 780 nm, wider than the typical NOPA tunable range in the visible (490—720 nm).[6] Furthermore, the S_{+1} and S_{+2} bandwidth at α=7° supports temporal compressibility <15 fs. The typical S_{+1} pulse duration was measured via cross correlation with another time-delayed weak FP beam and is ~75 fs, which resembles the SCWL pulse duration (~80 fs).[13] The chirp structure of the sideband is thus derived from the inherent chirp of the SCWL, and can be compensated by prism compression. As the sideband is tuned toward the blue, the bandwidth further increases. To understand this trend, we evaluate the wavevector mismatch between the exactly phase-matched beam calculated in the noncollinear geometry [see Eq. (3.1)] and the cascaded beam due to energy conservation. From the latter relation, the sideband wavevector in vacuum $k = \omega/c$, and c is the velocity of light. The wavevector magnitude in Eq. (3.1) is given by $k = 2\pi \cdot n(\lambda)/\lambda$, wherein $n(\lambda)$ is the wavelength-dependent refractive index in glass. The observed trend is qualitatively consistent with a BUMA phase-mismatch calculation that at a shorter center wavelength the material dispersion is better compensated by the noncollinear geometry, so broader bandwidth is achieved.[9]

In order to determine the exact spectral component of the positively chirped SCWL interacting with FP to generate the observed BUMA, we measure the center wavelengths of the first two sidebands through the entire tunable range. At each time delay, the experiment condition is kept while the thin BBO is switched into the setup instead of the

BK7 glass. The SFG signal wavelength is measured. Given that FP is centered at 800 nm, the SCWL component that coincides with FP can thus be derived. As shown in Figure 3.4b, calculations based on Eq. (3.1) reproduce the wavelength variation of both S_{+1} and S_{+2} at α=7° due to the interaction between FP and the specific spectral component of SCWL via tuning the time delay. In other words, the time separation between various spectral components in the chirped SCWL gives rise to the temporal tunability of BUMA. When the redder component of SCWL is used, the observed sideband center wavelength is bluer than the calculated value. The reason is that FP is a fs pulse with ~31 nm bandwidth, so wavelength components other than 800 nm (i.e., the monochromatic value used for FP in the PMC equation) may contribute. Moreover, when taken into account the ultrafast pulsed nature of the two input beams, a more precise description involving integral of the FWM nonlinear polarization density results in a blueshift of the computed signals.[10]

3.5 Sidebands used as the Raman probe in FSRS

The BUMA sidebands generated via nonresonant CFWM processes are ultrabroad and stable,[13] showing a power stability of ~1.5% RMS over a typical time period of 1 hour. The intensity of the sidebands is in the vicinity of ~50 μW, so they can be used as the probing light covering a wide spectral range (visible to near IR) in ultrafast spectroscopy. In contrast, the conventional SCWL in sapphire covers ca. 500—950 nm,[24-26] but cannot produce stable and ample photons in the visible to near IR to generate FSRS signals across a broad spectral window (with an 800 nm Raman pump), due to interference with the

residual, still very strong incident FP. We implement the newly generated S_{+1} signal as the Raman probe pulse in our FSRS setup. FSRS is an emerging ultrafast spectroscopic technique that provides structural dynamics information with high temporal and spectral resolution, though the detectable window is typically within 500—1800 cm^{-1}.[14,17,27-29] Above 1800 cm^{-1}, SCWL photons are scarce. Below 500 cm^{-1}, the interference between the probe fundamental and the generated SCWL hinders stimulated Raman with high signal-to-noise ratio (SNR). However, low-frequency modes are crucial for studying molecular conformational dynamics because underdamped coherent nuclear motions occur in that spectral regime,[5,15,16,30-32] whereas H-bonding dynamics can be tracked via O–H stretch above 2500 cm^{-1}.[4,33] Figure 3.5 shows the ground state FSRS spectrum of carbon tetrachloride:ethanol 1:1 (v/v) mixture solution. A phase-locked optical chopper is synchronized with the laser and chopping the Raman pump at 500 Hz, so we obtain one spectrum in 2 ms according to the formula: Stimulated Raman Gain/Loss = Raman-probe-$spectrum_{pump\text{-}on}$/Raman-probe-$spectrum_{pump\text{-}off}$ −1. Here we collect 60 sets of spectra, each set consisting of 3000 laser shots, so 90,000 spectra collected within ~3 minutes are efficiently averaged to generate one ground state anti-stokes FSRS spectrum[34-36] with sharp vibrational features from 100—4000 cm^{-1}. The result is in excellent agreement with spontaneous Raman data for the solvents. The remarkable SNR of FSRS incorporating the background-free, filter-free S_{+1} BUMA signal can be appreciated from the Figure 3.5 inset. The probe spectrum shows tiny yet noticeable dips corresponding to vibrational transitions upon Raman pump interaction, generating high-SNR stimulated Raman loss spectrum via efficient averaging and division performed by LabVIEW within minutes. Moreover, the

ps-fs pulsed nature of Raman pump-probe pair ensures the feasibility for time-resolved excited-state FSRS with the incorporation of a photoexcitation pulse.[5,14-17,28]

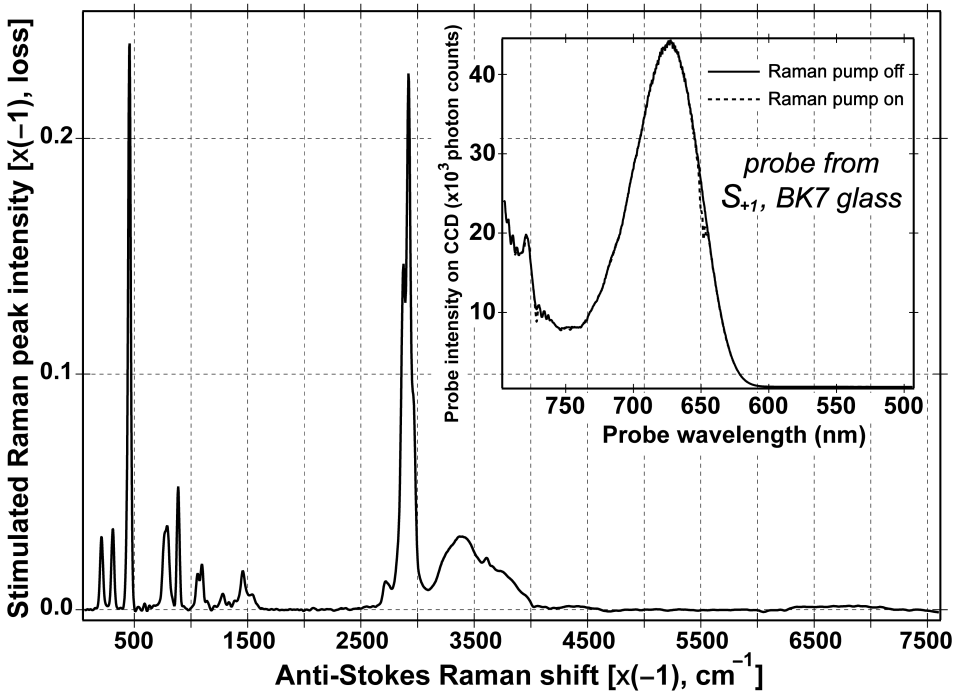

Figure 3.5 The ground-state FSRS spectrum of 1:1 carbon tetrachloride:ethanol mixed solution spanning a broad spectral range over 4000 cm^{-1}. The probe is the S_{+1} BUMA sideband generated in glass, specifically tuned to expose both the low- and high-frequency vibrational modes of the sample. The probe intensity profile has been used to normalize the Raman spectrum across the wide spectral window. The probe spectra with Raman pump on (dashed) and off (solid line) are shown in the inset with the tiny dips representing the detected Raman loss signal (shown as positive peaks in the main graph), manifesting the remarkable SNR of the FSRS methodology.

3.6 Conclusions

In summary, we report the convenient and economical generation of spatially dispersed BUMA signals via CFWM processes in a 0.15-mm-thick BK7 glass slide, using two weak near-IR fs laser pulses with various crossing angles (optimal α=7°). The spectral tunability from visible to near IR (500—780 nm) is readily achieved by tuning the time delay between the two incident pulses. The ultrabroad sideband laser generation using our versatile optical setup is applicable to nearly all transparent media due to their non-zero $\chi^{(3)}$ property.[9,10] The proof-of-principle FSRS experiment is conducted using one of the BUMA sidebands in the near-IR region, yielding a high-quality Raman spectrum spanning the broad detection window of 100—4000 cm^{-1} and free of interference in the low-frequency region. This advance enriches the existing FSRS methodology to be a powerful toolset for molecular structural dynamics studies on the ultrafast timescale.

3.7 References

[1] A. H. Zewail, *Femtochemistry: Ultrafast Dynamics of the Chemical Bond*. (World Scientific, Singapore, 1994).

[2] J. Zheng, K. Kwak, J. Asbury, X. Chen, I. R. Piletic, and M. D. Fayer, "Ultrafast Dynamics of Solute-Solvent Complexation Observed at Thermal Equilibrium in Real Time", *Science* **309** (5739), 1338-1343 (2005).

[3] G. S. Engel, T. R. Calhoun, E. L. Read, T.-K. Ahn, T. Mancal, Y.-C. Cheng, R. E. Blankenship, and G. R. Fleming, "Evidence for Wavelike Energy Transfer Through Quantum Coherence in Photosynthetic Systems", *Nature* **446**, 782-786 (2007).

[4] R. M. Hochstrasser, "Two-Dimensional Spectroscopy at Infrared and Optical Frequencies", *Proc. Natl. Acad. Sci. U.S.A.* **104** (36), 14190-14196 (2007).

[5] C. Fang, R. R. Frontiera, R. Tran, and R. A. Mathies, "Mapping GFP Structure Evolution during Proton Transfer with Femtosecond Raman Spectroscopy", *Nature* **462** (7270), 200-204 (2009).

[6] G. Cerullo and S. D. Silvestri, "Ultrafast Optical Parametric Amplifiers", *Rev. Sci. Instrum.* **74** (1), 1-16 (2003).

[7] R. Nietzke, P. Fenz, W. Elsasser, and E. O. Gobel, "Cascade Four-Wave Mixing in Semiconductor Lasers", *Appl. Phys. Lett.* **51** (17), 1298-1300 (1987).

[8] R. Danielius, P. D. Trapani, A. Dubietis, A. Piskarskas, D. Podenas, and G. P. Banfi, "Self-Diffraction through Cascaded Second-Order Frequency-Mixing Effects in Beta-Barium Borate", *Opt. Lett.* **18** (8), 574-576 (1993).

[9] H. Crespo, J. T. Mendonca, and A. Dos Santos, "Cascaded Highly Nondegenerate Four-Wave-Mixing Phenomenon in Transparent Isotropic Condensed Media", *Opt. Lett.* **25** (11), 829-831 (2000).

[10] J. Liu and T. Kobayashi, "Generation and Amplification of Tunable Multicolored Femtosecond Laser Pulses by Using Cascaded Four-Wave Mixing in Transparent Bulk Media", *Sensors* **10** (5), 4296-4341 (2010).

[11] W. Liu, L. Zhu, and C. Fang, "Observation of Sum-Frequency-Generation-Induced Cascaded Four-Wave Mixing Using Two Crossing Femtosecond Laser Pulses in a 0.1 mm Beta-Barium-Borate Crystal", *Opt. Lett.* **37** (18), 3783-3785 (2012).

[12] R. Weigand, J. T. Mendonca, and H. M. Crespo, "Cascaded Nondegenerate Four-Wave-Mixing Technique for High-Power Single-Cycle Pulse Synthesis in the Visible and Ultraviolet Ranges", *Phys. Rev. A* **79** (6), 063838 (2009).

[13] W. Liu, L. Zhu, L. Wang, and C. Fang, "Cascaded Four-Wave Mixing for Broadband Tunable Laser Sideband Generation", *Opt. Lett.* **38** (11), 1772-1774 (2013).

[14] D. W. McCamant, P. Kukura, S. Yoon, and R. A. Mathies, "Femtosecond Broadband Stimulated Raman Spectroscopy: Apparatus and Methods", *Rev. Sci. Instrum.* **75** (11), 4971-4980 (2004).

[15] W. Liu, F. Han, C. Smith, and C. Fang, "Ultrafast Conformational Dynamics of Pyranine during Excited State Proton Transfer in Aqueous Solution Revealed by

Femtosecond Stimulated Raman Spectroscopy", *J. Phys. Chem. B* **116**, 10535-10550 (2012).

16 F. Han, W. Liu, and C. Fang, "Excited-State Proton Transfer of Photoexcited Pyranine in Water Observed by Femtosecond Stimulated Raman Spectroscopy", *Chem. Phys.*, **422**, 204-219 (2013).

17 Y. Wang, W. Liu, L. Tang, B. G. Oscar, F. Han, and C. Fang, "Early Time Excited-State Structural Evolution of Pyranine in Methanol Revealed by Femtosecond Stimulated Raman Spectroscopy", *J. Phys. Chem. A*, **117** (29), 6024-6042 (2013).

18 T. Y. F. Tsang, "Optical Third-Harmonic Generation at Interfaces", *Phys. Rev. A* **52**, 4116-4125 (1995).

19 W. Liu, L. Wang, F. Han, and C. Fang, "Distinct Broadband Third-Harmonic Generation on a Thin Amorphous Medium-Air Interface", *Opt. Lett.*, Under review (2013).

20 J. Liu and T. Kobayashi, "Cascaded Four-Wave Mixing and Multicolored Arrays Generation in a Sapphire Plate by Using Two Crossing Beams of Femtosecond Laser", *Opt. Express* **16** (26), 22119-22125 (2008).

21 J. Liu and T. Kobayashi, "Wavelength-Tunable, Multicolored Femtosecond-Laser Pulse Generation in Fused-Silica Glass", *Opt. Lett.* **34** (7), 1066-1068 (2009).

22 J. L. Silva, R. Weigand, and H. M. Crespo, "Octave-Spanning Spectra and Pulse Synthesis by Nondegenerate Cascaded Four-Wave Mixing", *Opt. Lett.* **34** (16), 2489-2491 (2009).

23 J. T. Mendonca, H. Crespo, and A. Guerreiro, "A New Method for High-Harmonic Generation by Cascaded Four-Wave Mixing", *Opt. Commun.* **188** (5-6), 383-388 (2001).

24 A. Zheltikov, "Editorial: Supercontinuum Generation", *Appl. Phys. B* **77** (2-3), 143-147 (2003).

25 K. Wang, L. Qian, H. Luo, P. Yuan, and H. Zhu, "Ultrabroad Supercontinuum Generation by Femtosecond Dual-Wavelength Pumping in Sapphire", *Opt. Express* **14** (13), 6366-6371 (2006).

26 T. Imran and G. Figueira, "Intensity-Phase Characterization of White-Light Continuum Generated in Sapphire by 280 fs Laser Pulses at 1053 nm", *J. Opt.* **14** (3), 035201 (2012).

27 S. Shim and R. A. Mathies, "Generation of Narrow-Bandwidth Picosecond Visible Pulses from Broadband Femtosecond Pulses for Femtosecond Stimulated Raman", *Appl. Phys. Lett.* **89**, 121124 (2006).

28 R. R. Frontiera, C. Fang, J. Dasgupta, and R. A. Mathies, "Probing Structural Evolution along Multidimensional Reaction Coordinates with Femtosecond Stimulated Raman Spectroscopy", *Phys. Chem. Chem. Phys.* **14**, 405-414 (2012).

29 M. Yoshizawa and M. Kurosawa, "Femtosecond Time-Resolved Raman Spectroscopy Using Stimulated Raman Scattering", *Phys. Rev. A* **61** (1), 013808 (1999).

30 M. H. Vos, F. Rappaport, J.-C. Lambry, J. Breton, and J.-L. Martin, "Visualization of Coherent Nuclear Motion in a Membrane Protein by Femtosecond

Spectroscopy", *Nature* **363**, 320-325 (1993).

[31] L. Zhu, J. T. Sage, and P. M. Champion, "Observation of Coherent Reaction Dynamics in Heme Proteins", *Science* **266** (5185), 629-632 (1994).

[32] A. Douhal, S. K. Kim, and A. H. Zewail, "Femtosecond Molecular Dynamics of Tautomerization in Model Base Pairs", *Nature* **378** (16), 260-263 (1995).

[33] E. T. J. Nibbering, H. Fidder, and E. Pines, "Ultrafast Chemistry: Using Time-Resolved Vibrational Spectroscopy for Interrogation of Structural Dynamics", *Annu. Rev. Phys. Chem.* **56**, 337-367 (2005).

[34] R. R. Frontiera, S. Shim, and R. A. Mathies, "Origin of Negative and Dispersive Features in Anti-Stokes and Resonance Femtosecond Stimulated Raman Spectroscopy", *J. Chem. Phys.* **129** (6), 064507-064506 (2008).

[35] S. Umapathy, B. Mallick, and A. Lakshmanna, "Mode-Dependent Dispersion in Raman Line Shapes: Observation and Implications from Ultrafast Raman Loss Spectroscopy", *J. Chem. Phys.* **133** (2), 024505-024506 (2010).

[36] X. Qiu, X. Li, K. Niu, and S.-Y. Lee, "Inverse Raman Bands in Ultrafast Raman Loss Spectroscopy", *J. Chem. Phys.* **135**, 164502 (2011).

Chapter 4 A Versatile Femtosecond Stimulated Raman Spectroscopy Setup with Tunable Pulses in the Visible to Near Infrared

Liangdong Zhu, Weimin Liu, and Chong Fang*

Applied Physics Letters, **105** (4), 041106, July 28, 2014 DOI: 10.1063/1.4891766

4.1 Abstract

In this Chapter, we demonstrate a versatile and efficient setup to perform femtosecond stimulated Raman spectroscopy (FSRS). Technical innovations are implemented to achieve the wavelength tunability for both the picosecond narrowband Raman pump pulse and femtosecond broadband Raman probe pulse. Using a simplified one-grating scheme in a home-built second harmonic bandwidth compressor followed by a two-stage noncollinear optical parametric amplifier, we tune the Raman pump pulse from ca. 480—750 nm. To generate the suitable Raman probe pulse in tandem, we rely on our recently demonstrated broadband up-converted multicolor array technique that readily provides tunable broadband laser sidebands across the visible to near-infrared range. This unique setup has unparalleled flexibility for conducting FSRS. We measure the ground-state Raman spectra of a cyclohexane standard using tunable pump-probe pairs at various wavelengths across the visible region. The best spectral resolution is about 12 cm^{-1}. By tuning the pump wavelength closer to the electronic absorption band of a photoacid pyranine in water, we observe the pre-resonantly enhanced Raman signal. The stimulated Raman gain of the 1627 cm^{-1} mode is increased by over 15 times.

4.2 Introduction and motivation

Ultrafast spectroscopic techniques are powerful in tackling some of the most challenging problems in modern physics, chemistry, biology, and materials science with the advancement of femtosecond laser technologies.[1-4] Using sophisticated sequence of laser

pulses in specific geometries, researchers can unravel the microscopic atomic motions that play a crucial role leading to macroscopic functions. The key is to capture molecular structural snapshots with simultaneously high spectral and temporal resolution. In particular, studies of photophysical and photochemical events in life processes including photosynthesis and fluorescence as well as photolysis of metal-organic complexes in materials science demand a technique that can access nuclear coordinates in the electronic excited state.

In contrast to the commonly used transient absorption that infers molecular speciation in the electronic domain,[5-7] femtosecond stimulated Raman spectroscopy (FSRS) is an emerging structural dynamics technique that can acquire high signal-to-noise ratio excited-state vibrational spectrum free from fluorescence background.[3,8-10] In FSRS, a picosecond (ps) narrowband Raman pump pulse and a femtosecond (fs) broadband probe pulse are used to stimulate Raman scattering signals and produce sharp vibrational features across a wide spectral region. Since the resultant FSRS spectrum is obtained based on the equation, Raman gain = Raman probe spectrum with pump on / Raman probe spectrum with pump off – 1, a combination of 500-Hz optical chopper in the pump arm and a CCD camera synchronized with the 1-kHz laser repetition rate ensures that one stimulated Raman spectrum can be obtained in 2 ms.[11,12] Large quantities of data traces can thus be efficiently collected and averaged to improve the signal-to-noise ratio. Further advantages of using FSRS to study molecular motions either in the ground state or excited state are accomplished by tuning the Raman pump and probe pulses across a broad spectral range.

One can make use of resonance enhancement with a tunable pump[13-18] to increase the Raman signal, in conjunction with the probe improvement of generating a tunable broadband pulse to access the low-frequency region[10,19] as compared to conventional continuous-wave Raman or IR spectroscopy. Furthermore, the direct collection of dispersed spectral signal in the frequency domain essentially performs Fourier transform of the time-domain signal in a grating-based spectrograph, leading to much reduced data collection time and a better experimental platform to track photoinduced structural motions in an electronic excited state.

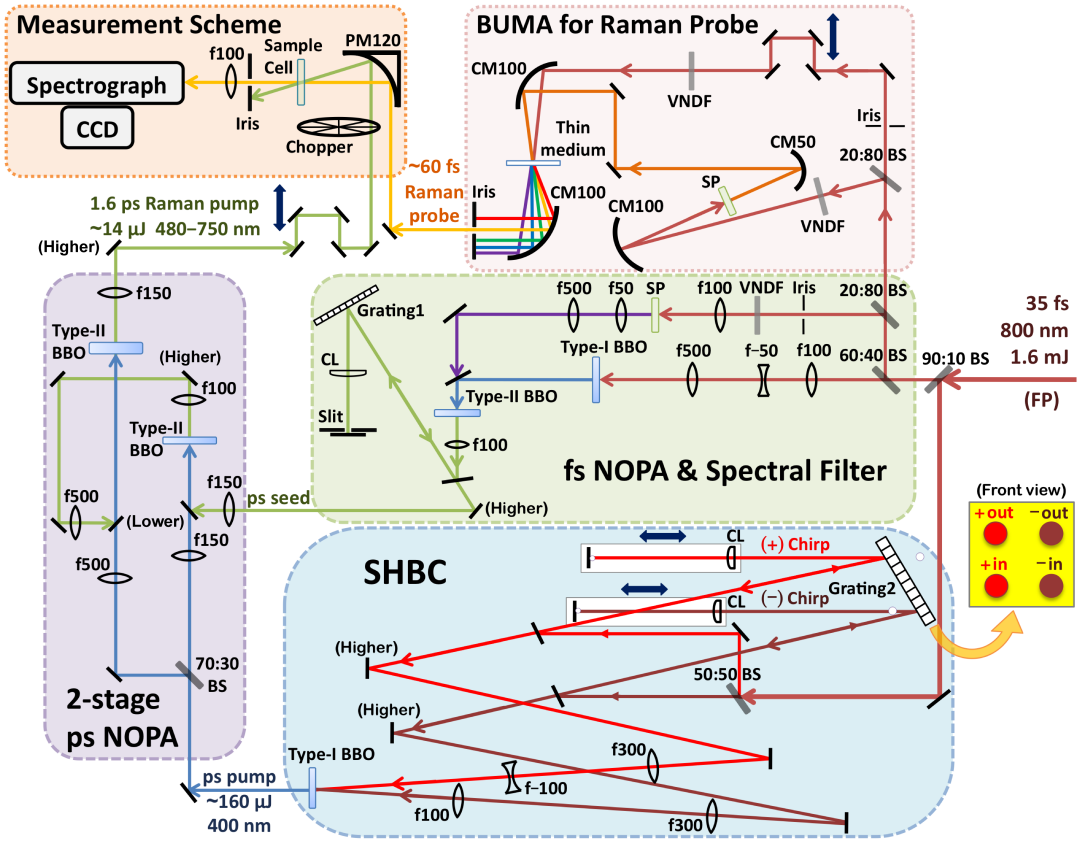

Figure 4.1 Schematic (top-view) of our experimental setup to perform tunable FSRS. The 800 nm fundamental pulse (FP) powers three distinct parts: SHBC (light blue shade), fs NOPA and spectral filter (light green), and BUMA apparatus (light red). The ps pump and seed pulses are combined in the two-stage single-pass ps NOPA (light violet) to generate tunable, ps Raman pump pulse in the visible. The Raman ps pump and fs probe pulses interrogate the sample in the measurement scheme (light orange). SP, sapphire plate; VNDF, variable neutral-density filter; BS, beamsplitter; f100, lens with focal length of 100 mm; CM, concave mirror; CL, cylindrical lens; PM, parabolic mirror. Grating1 (2) denotes the plane-ruled reflective grating with 1800 (1200) grooves/mm and 500 (1000) nm blaze. Most delay lines for time overlap are omitted for simplicity. The four-beam geometry on the single grating in SHBC is depicted on the right (yellow). The focal points are marked by small white circles beside Grating2. The 90:10 BS represents 90% Reflection, 10%

Transmission. In the NOPA setup, the *p*-polarized visible seed and *s*-polarized 400-nm pump beams are vertically displaced and overlapped in type-II BBO in a noncollinear geometry with a crossing angle of ~3º.

4.3 Experimental setup

In this Letter, we demonstrate an improved FSRS setup Figure 4.1 that can simultaneously tune the Raman pump (R_{pu}) pulse in the visible (ca. 480—750 nm) and the accompanying Raman probe (R_{pr}) pulse in the visible to near IR (ca. 450—850 nm). Notably, the broad spectral coverage is continuous without gaps. Briefly, the fs laser system consists of a mode-locked OPSL-technology-based Ti:Sapphire oscillator (Mantis-5) and regenerative amplifier (Legend Elite-USP-1K-HE, Coherent) that provides ~4 W fundamental pulse (FP) at 800 nm (35 fs, 1 kHz). About 1.6 mJ/pulse FP is used to generate the tunable pulses for FSRS. The R_{pu} generation consists of three parts: 1) second-harmonic bandwidth compressor (SHBC) that produces a 400-nm narrowband ps pump; 2) femtosecond noncollinear optical parametric amplifier (NOPA) and grating-slit-based spectral filter[13] that produce narrowband ps seed with wavelength tunability; and 3) a two-stage ps-NOPA that amplifies the ps seed with the ps pump to generate the intense, tunable ps R_{pu} output. In parallel, a broadband up-converted multicolor array (BUMA) setup (developed in our laboratory) provides a tunable broadband fs pulse as R_{pr}. Both the R_{pu} and R_{pr} pulses are then combined noncollinearly and focused onto the sample to perform ground-state FSRS measurements.[4,11,12]

The BUMA signal has been used as R_{pr} to collect an anti-stokes Raman spectrum of a solvent mixture with R_{pu}=800 nm.[10] Here, we aim to exploit the full potential of BUMA technology in tunable FSRS. In the BUMA setup (Figure 4.1, light red area), ~75 μJ/pulse FP passes through a 20R:80T (R, reflection; T, transmission) beamsplitter. The reflected arm is focused on a 2-mm-thick *Z*-cut single-crystal sapphire plate to generate supercontinuum white light (SCWL). The transmitted arm is attenuated before being focused on a 0.5-mm-thick transparent medium[19-23] (e.g., quartz plate) to noncollinearly pump SCWL with a crossing angle of ~6°. The diameters of both beams on the quartz surface are ~200 μm measured by a blade-on-a-translation-stage method. We use quartz due to its high optical damage threshold and better transmission for the UV light..[24] Depending on the R_{pu} wavelength, one of the first three BUMA sidebands (S_{+1} for R_{pu}>600 nm, S_{+2} for 520≤R_{pu}≤600 nm, and S_{+3} for R_{pu}<520 nm) is selected as R_{pr}. All the sidebands have the same *p*-polarization as the incident SCWL.

The advantages of the BUMA probe over the commonly used SCWL are the following. (1) Wavelength tunability is achieved by varying the time delay between the two incident pulses. (2) It is background free because the sidebands are spatially separated from FP. Traditionally, a broadband probe near 800 nm is difficult to obtain because of strong interference between the nascent SCWL and residual 800-nm FP. This limits our capabilities to investigate molecular systems with interesting electronic and/or vibrational features in this spectral regime. BUMA sidebands fill the void and the influence from residual FP can be minimized.[4] (3) BUMA sidebands are self-compressed to ca. 30—60 fs

pulse duration[19,23] so no additional compression is needed, in contrast to the complex compression system required for SCWL.[9,11] (4) Parametric amplification based on $\chi^{(3)}$ and $\chi^{(2)}$-nonlinearities[25] increases the sideband signal intensity so higher signal-to-noise ratio in FSRS can be achieved. Furthermore, compared to the NOPA probe,[15] the BUMA probe offers subsequent benefits. (1') It is economical and flexible.[10,19,23,25-27] Depending on applications such as fs Raman or optical switching, various media can be used that include BBO, sapphire, CaF_2, quartz, BK7 glass, etc. (2') Broadband sidebands are readily achieved and potentially on either side of FP.[25] It does not require precise tuning of the phase-matching angle[28] or manipulation of the input beams.[21,29]

To generate the intense picosecond R_{pu} from an femtosecond laser source, several conversion stages are needed. In the green shaded area of Figure 4.1, ~20 μJ of FP is attenuated and focused onto a 2-mm-thick sapphire plate to generate SCWL. About 60 μJ of FP undergoes beam size reduction through a telescope and frequency doubling in a 1-mm-thick type-I BBO to generate ~20 μJ SH pulses. The SCWL and 400-nm pulses are focused onto a 1-mm-thick type-II BBO as the signal and pump, respectively, in an fs-NOPA setup. The center wavelength of the amplified signal is tunable from ca. 480—750 nm via rotating the BBO crystal and adjusting the time delay between the two incident pulses. The NOPA output (~1 μJ/pulse) is dispersed by a reflective grating (1800 grooves/mm, 500 nm blaze at 26.7°; 10RG1800-500-1, Newport) and focused on an adjustable slit by a cylindrical lens (CL) to select a portion with ~12 cm^{-1} bandwidth.[13,14] The spectrally filtered pulse is used in the subsequent two-stage ps-NOPA as the ps seed.

Based on the effect of chirp elimination in second-harmonic generation (SHG) when the incident FPs have opposite temporal chirps,[30,31] chirp-free 400-nm ps pump is generated in a homemade SHBC (Figure 4.1, light blue area). The input FP is evenly split into the positive and negative-chirp arms. Instead of using one grating per arm in most commercial and research lab systems,[15-17] we achieve a compact and economical setup with just one reflective grating (1200 grooves/mm, 1000 nm blaze at 36.8°; 20RG1200-1000-2, Newport). In each arm, a CL and a back mirror on the focal point of the CL are placed on a translation stage. Dispersion depends on the distance between the CL and grating (denoted as d_1/ d_2 for the positive/negative-chirp arm). The two translation stages are placed that d_1/d_2 is smaller/larger than the CL focal length. To generate a chirp-free SH pulse, d_1 and d_2 need to be precisely tuned to equalize the magnitude of the two opposite chirps. Experimentally, this is achieved by sending one FP into both arms consecutively, and the duration of the output matches input when the two opposite chirps cancel each other.[32] The two chirped pulses are then telescoped to smaller beam sizes (~2 mm diameter)[15] and combined noncollinearly on a 1-mm-thick type-I BBO to generate the 400 nm, ~160 μJ, 2 ps SH pulse. Considering that each incident chirped-FP energy is ~300 μJ, the conversion efficiency reaches ~27%.

The SHBC output is divided by a beamsplitter (70%R) to pump a two-stage ps-NOPA system (Figure 4.1, light violet area) that ensures high conversion efficiency and output stability. The ps seed is amplified in the first ps-NOPA (3-mm-thick type-II BBO) to ~1 μJ, and further amplified up to 14 μJ in the second ps-NOPA (5-mm-thick type-II BBO).

This represents an overall conversion efficiency of ~1% (from fs FP to ps R_{pu}) that is adequate.[13-15,17] Higher efficiency can be obtained by changing the SHBC grating blaze (Figure 4.1) from 1 μm to 800 nm. After collimation, the ps pulse is ready to be used as the narrowband R_{pu} for tunable FSRS.

4.4 Characterization of pump and probe pulses

To characterize the ps R_{pu}, we measure its spectrum (e.g., centered at ~599 nm) using an Ocean Optics spectrometer (QE65-Pro, spectral range 520—690 nm) (see Figure 4.2a). The full-width-at-half-maximum (FWHM) is 1.02 nm (27.8 cm^{-1}). The pulse duration is obtained by a home-built SHG-autocorrelator with a 0.1-mm-thick type-I BBO. The FWHM of the autocorrelation signal is 2.27 ps (Figure 4.2b), corresponding to an incident pulse duration of ~1.6 ps. Autocorrelation profiles for other R_{pu} wavelengths (Figure 4.3a) are similar. The near-Gaussian temporal profile improves spectral resolution while minimizing unwanted spectral ringing in FSRS data.[18] The time-bandwidth product of the measured~44.5 ps·cm^{-1} is ~3 times the Fourier-transform limit of a Gaussian pulse (14.7 ps cm^{-1}),[14,17] indicative of a chirped R_{pu}. However, by adjusting the temporal and spatial overlap between the collimated Raman pump-probe pair, we can obtain high-quality FSRS data without the need to achieve the narrowest bandwidth for a chirp-free R_{pu}. This is because the broadband fs-R_{pr} induces the vibrational coherence only with a specific portion of R_{pu} during their time overlap,[9,11] and the amount of R_{pu} temporal chirp occurring during

the vibrational dephasing time is significantly less than the vibrational linewidth.[3,33] Therefore, the distorted FSRS lineshape is not apparent (see below).

In the measurement scheme (Figure 4.1, light orange area), the *p*-polarized R_{pu} and R_{pr} are spatially and temporally overlapped at the sample cell in a crossing geometry. The transmitted R_{pr} carrying the stimulated Raman scattering signal is dispersed by a 600-grooves/mm grating (400 nm blaze) in a spectrograph (MS127i, Oriel) and focused onto a 1430×100 CCD-array camera (PIXIS 100F, Princeton Instruments) synchronized at the laser repetition rate of 1kHz. Instrument control and initial data processing are performed by LabVIEW.

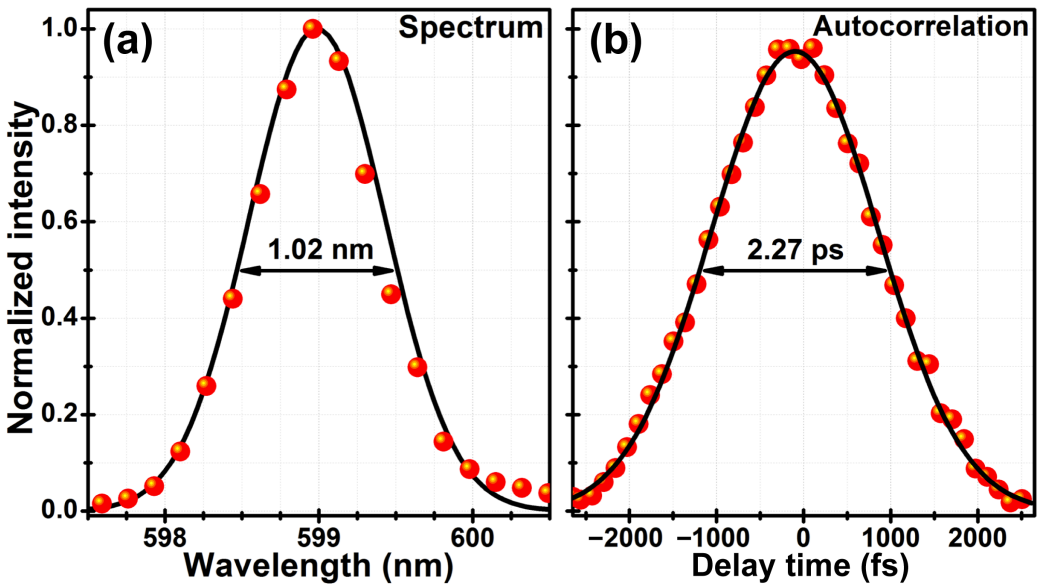

Figure 4.2 Characterization of a typical narrowband R_{pu} pulse. The spectral (a) and temporal (b) profile of the picosecond R_{pu} centered at 599 nm. Red spheres represent the experimental data while black solid lines are Gaussian fits. The FWHM values are indicated.

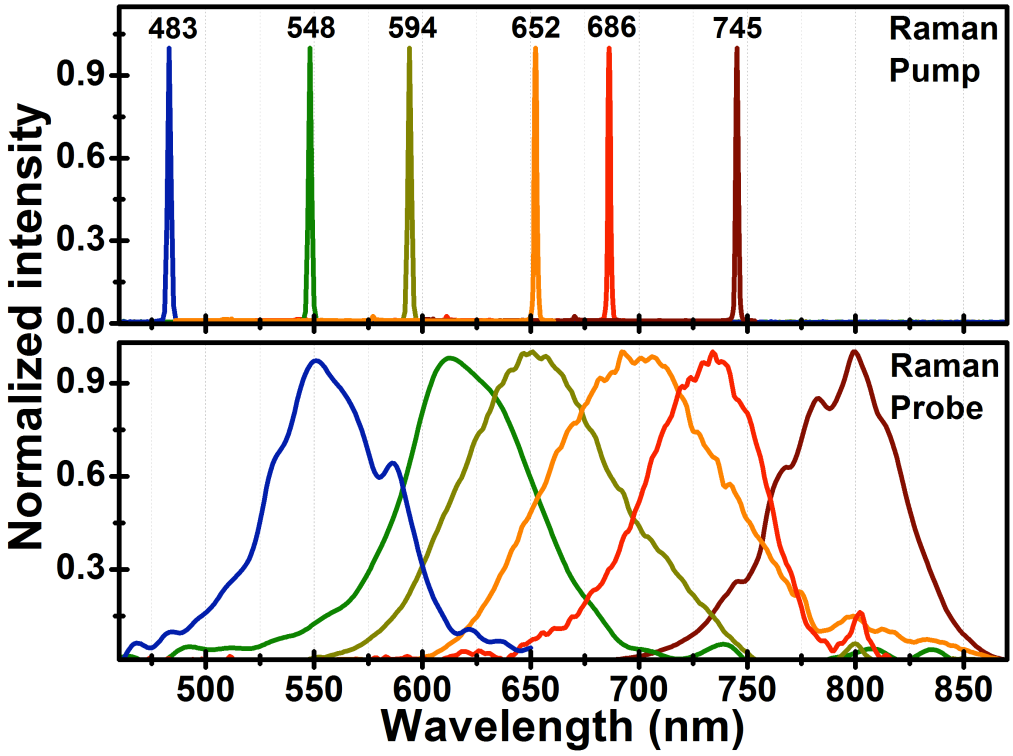

Figure 4.3 Broad tunability of the R_{pu} and R_{pr} pulses in pairs. Normalized experimental R_{pu} spectra at six different center wavelengths: 483, 548, 594, 652, 686, and 745 nm (top) and the corresponding R_{pr} spectra from BUMA sidebands (bottom). By tuning the BUMA apparatus and choosing the order of sidebands to cover various spectral regions, we can conveniently collect the stimulated Raman spectrum spanning from ca. 100—4000 cm^{-1} at each R_{pu} wavelength.

4.5 Tunability examination

To examine the tunability of our setup, we collect the ground-state FSRS spectra of cyclohexane (a solvent standard) at six different R_{pu} wavelengths with the power of 12±1 μJ/pulse. The broad tunable range of R_{pu}-R_{pr} pairs is exhibited in Figure 4.3, and resultant Raman spectra are shown in Figure 4.4. The FWHM of the 802 cm^{-1} mode varies from 27 cm^{-1} (R_{pu}=483 nm) to 12 cm^{-1} (R_{pu}=745 nm). The main factor that increases the R_{pu} bandwidth is spectral broadening by the ps-NOPA processes. In particular, the precision limit of the grating-mechanical-slit filter yields a broader R_{pu} bandwidth at shorter wavelengths. The small ringing near the main peak is likely due to our ~1.6 ps R_{pu} that still truncates the mode free induction decay to some extent (dephasing time of ~2.0 ps). Additional spectral filtering of R_{pu} has shown to be useful.[18] The 802 cm^{-1} mode gain varies from 28% (R_{pu}=652 nm) to 44% (R_{pu}=483 nm), displaying no clear trend versus the R_{pu} wavelength. Meanwhile, the intensity ratios between the 802, 1028, 1266, and 1445 cm^{-1} peaks remain unchanged throughout wavelength tuning, consistent with the intensity-corrected standard cyclohexane Raman spectrum acquired using 532 and 752-nm excitation.[34] We note that the solvent cyclohexane has no significant absorption in the visible range, hence the relatively small enhancement effect as R_{pu} is tuned toward the blue region (closer to the electronic absorption band of cyclohexane below 200 nm).

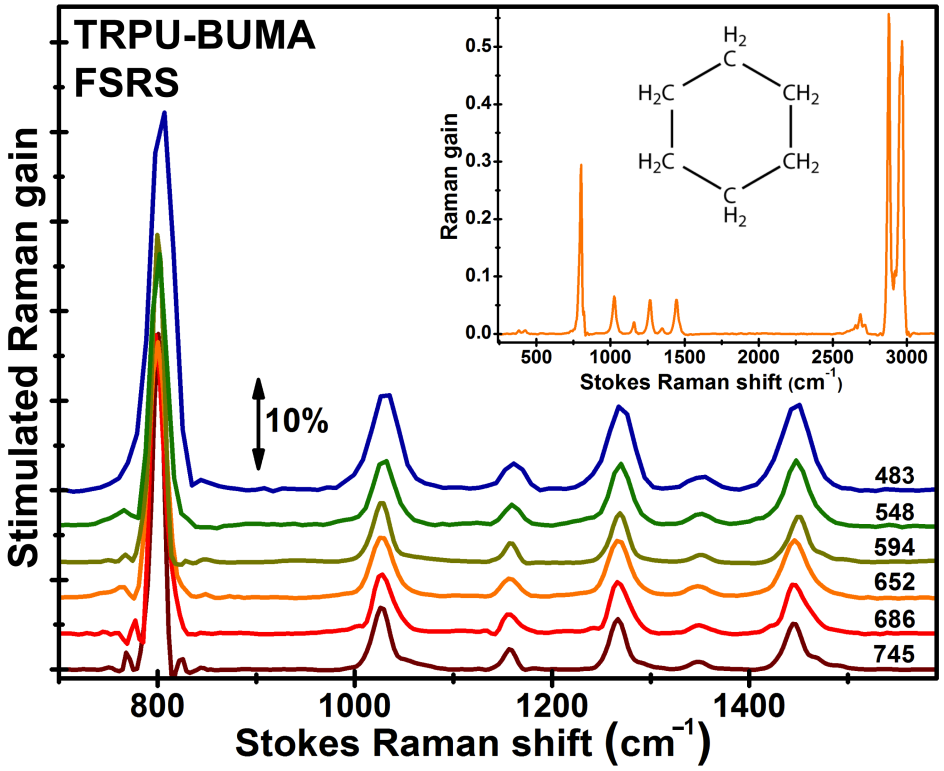

Figure 4.4 Ground-state FSRS spectra of cyclohexane collected at six different R_{pu} wavelengths. TRPU: tunable Raman pump. The inset shows the FSRS spectrum (R_{pu}=652 nm) spanning an ultrabroad range (ca. 200—3500 cm^{-1}). The chemical structure of cyclohexane is depicted. The double-sided arrow represents the Raman gain magnitude of 10%.

One major motivation to develop tunable FSRS is to exploit resonance enhancement to increase the signal-to-noise ratio of Raman spectrum.[35-37] We measure the ground-state FSRS signal of 10-mM photoacid pyranine (8-hydroxypyrene-1,3,6-trisulfonic acid, or HPTS)[11,12,38] in water (Figure 4.5) which has a strong absorption band near 400 nm.. Seven different R_{pu} wavelengths are used and the corresponding 1627 cm^{-1} mode intensities are plotted in the Figure 4.5 inset. The vibrational modes of HPTS are clearly resolved with different intensity ratios from previous results[12] at R_{pu}=800 nm. The intensity ratio of the 1627 over 1368 cm^{-1} modes drops from 2:1 at 483-nm pump to 3:2 at 745-nm pump. These findings are indicative of mode-dependent Raman excitation profiles that lead to relative Raman intensity changes as a function of excitation wavelength.[37] To minimize influence from the overlapping lower-frequency shoulder, we use multi-Gaussian fitting to retrieve the peak height of the main band. The Raman gain of 0.44% at R_{pu}=745 nm is similar to the aforementioned R_{pu}=800 nm data (0.22%). When R_{pu} is blue-tuned to 594 nm, small enhancement is observed (0.73% gain). As R_{pu} is tuned toward the ~400-nm electronic absorption band of HPTS in water,[12,38] strong pre-resonance enhancement occurs: the 1627 cm^{-1} mode gain is ~2.0%, 2.9%, and 6.7% for R_{pu}=548, 528, and 483 nm, respectively. Therefore, >15 times increase of the Raman gain is observed upon tuning R_{pu} from 745 to 483 nm. Signal enhancement is especially useful when the intrinsic Raman cross-section is small, and with an additional actinic pump to photoexcite the sample, we can better capture spectral signatures of transient species during chemical reactions such as excited-state proton transfer in biomolecules.[3,39]

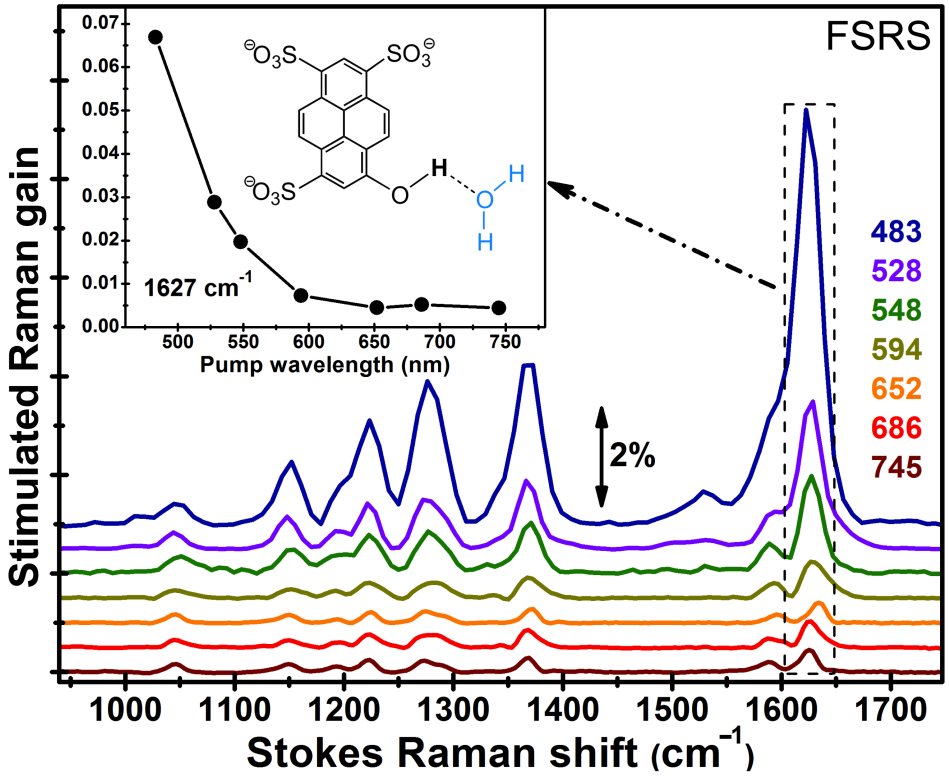

Figure 4.5 Ground-state FSRS spectra of pyranine (HPTS) collected at seven different R_{pu} wavelengths of 483, 528, 548, 594, 652, 686, and 745 nm. The amplitude of the strongest Raman peak at 1627 cm^{-1} is plotted against R_{pu} wavelength in the inset, where the chemical structure of HPTS molecule in H-bonding configuration with a nearby water molecule is illustrated. The double-sided arrow represents the Raman gain magnitude of 2%.

4.6 Conclusions

In summary, we have developed and implemented a unique FSRS setup with simultaneously tunable Raman pump and probe pulses in the visible from a single fs source. The narrowband ps Raman pump (480—750 nm, up to 14 μJ/pulse) offers the highest power among reported tunable FSRS setups,[13-18] while the SHBC design with one grating gives improved simplicity. The broadband fs Raman probe (450—850 nm, <100 nJ/pulse) arises from the spatially separated BUMA sidebands, which provide ultrabroad tunability with self-compression rooted in cascaded four-wave mixing.[20,23] In principle, we can extend the probe into the ultraviolet regime (i.e., <400 nm) using sum-frequency-generation/SHG-induced BUMA signals (see Chapter 6 below).[23,27,32] The convenience and versatility to broadly tune R_{pu}-R_{pr} pairs are manifested through the measurement of ground-state Raman spectrum of cyclohexane. Moreover, we achieve the pre-resonance enhancement of pyranine FSRS signals in aqueous solution by tuning R_{pu} toward the electronic absorption peak and the R_{pr} spectral profile in tandem. The combination of tunable ps and fs pulses from a commercially available fs-laser source will enable the elucidation of ultrafast structural dynamics by monitoring transient species with desirable specificity and sensitivity on the atomic level, thus paving the way for FSRS to be widely employed to tackle challenging problems[2-4,39] in materials, energy, and life sciences.

4.7 References

[1] G. S. Engel, T. R. Calhoun, E. L. Read, T.-K. Ahn, T. Mancal, Y.-C. Cheng, R. E. Blankenship, and G. R. Fleming, "Evidence for Wavelike Energy Transfer Through Quantum Coherence in Photosynthetic Systems", *Nature* **446**, 782-786 (2007).

[2] R. M. Hochstrasser, "Two-Dimensional Spectroscopy at Infrared and Optical Frequencies", *Proc. Natl. Acad. Sci. U.S.A.* **104** (36), 14190-14196 (2007).

[3] C. Fang, R. R. Frontiera, R. Tran, and R. A. Mathies, "Mapping GFP Structure Evolution during Proton Transfer with Femtosecond Raman Spectroscopy", *Nature* **462** (7270), 200-204 (2009).

[4] W. Wang, W. Liu, I.-Y. Chang, L. A. Wills, L. N. Zakharov, S. W. Boettcher, P. H.-Y. Cheong, C. Fang, and D. A. Keszler, "Electrolytic Synthesis of Aqueous Aluminum Nanoclusters and *in situ* Characterization by Femtosecond Raman Spectroscopy & Computations", *Proc. Natl. Acad. Sci. U.S.A.* **110** (46), 18397-18401 (2013).

[5] L. Zhu, J. T. Sage, and P. M. Champion, "Observation of Coherent Reaction Dynamics in Heme Proteins", *Science* **266** (5185), 629-632 (1994).

[6] M. Chattoraj, B. A. King, G. U. Bublitz, and S. G. Boxer, "Ultra-Fast Excited State Dynamics in Green Fluorescent Protein: Multiple States and Proton Transfer", *Proc. Natl. Acad. Sci. U.S.A.* **93** (16), 8362-8367 (1996).

[7] R. Berera, R. Grondelle, and J. M. Kennis, "Ultrafast Transient Absorption Spectroscopy: Principles and Application to Photosynthetic Systems", *Photosynth Res* **101** (2-3), 105-118 (2009).

[8] M. Yoshizawa and M. Kurosawa, "Femtosecond Time-Resolved Raman Spectroscopy Using Stimulated Raman Scattering", *Phys. Rev. A* **61** (1), 013808 (1999).

[9] D. W. McCamant, P. Kukura, S. Yoon, and R. A. Mathies, "Femtosecond Broadband Stimulated Raman Spectroscopy: Apparatus and Methods", *Rev. Sci. Instrum.* **75** (11), 4971-4980 (2004).

[10] L. Zhu, W. Liu, and C. Fang, "Tunable Sideband Laser from Cascaded Four-Wave Mixing in Thin glass for Ultra-Broadband Femtosecond Stimulated Raman Spectroscopy", *Appl. Phys. Lett.* **103** (6), 061110 (2013).

[11] W. Liu, F. Han, C. Smith, and C. Fang, "Ultrafast Conformational Dynamics of Pyranine during Excited State Proton Transfer in Aqueous Solution Revealed by Femtosecond Stimulated Raman Spectroscopy", *J. Phys. Chem. B* **116**, 10535-10550 (2012).

[12] F. Han, W. Liu, and C. Fang, "Excited-state proton transfer of photoexcited pyranine in water observed by femtosecond stimulated Raman spectroscopy", *Chem. Phys.* **422** (0), 204-219 (2013).

[13] S. Shim and R. A. Mathies, "Generation of Narrow-Bandwidth Picosecond Visible Pulses from Broadband Femtosecond Pulses for Femtosecond Stimulated Raman", *Appl. Phys. Lett.* **89**, 121124 (2006).

[14] D. T. Co, J. V. Lockard, D. W. McCamant, and M. R. Wasielewski, "Narrow-Bandwidth Tunable Picosecond Pulses in the Visible Produced by Noncollinear Optical Parametric Amplification with a Chirped Blue Pump", *Appl. Opt.* **49** (10), 1880-1885 (2010).

[15] S. A. Kovalenko, A. L. Dobryakov, and N. P. Ernsting, "An Efficient Setup for Femtosecond Stimulated Raman Spectroscopy", *Rev. Sci. Instrum.* **82** (6), 063102 (2011).

[16] H. Kuramochi, S. Takeuchi, and T. Tahara, "Ultrafast Structural Evolution of Photoactive Yellow Protein Chromophore Revealed by Ultraviolet Resonance Femtosecond Stimulated Raman Spectroscopy", *J. Phys. Chem. Lett.* **3** (15), 2025-2029 (2012).

[17] M. Nejbauer and C. Radzewicz, "Efficient Spectral Shift and Compression of Femtosecond Pulses by Parametric Amplification of Chirped Light", *Opt. Express* **20** (3), 2136-2142 (2012).

[18] E. Pontecorvo, C. Ferrante, C. G. Elles, and T. Scopigno, "Spectrally Tailored Narrowband Pulses for Femtosecond Stimulated Raman Spectroscopy in the Range 330-750 nm", *Opt. Express* **21** (6), 6866-6872 (2013).

[19] W. Liu, L. Zhu, L. Wang, and C. Fang, "Cascaded Four-Wave Mixing for Broadband Tunable Laser Sideband Generation", *Opt. Lett.* **38** (11), 1772-1774 (2013).

[20] H. Crespo, J. T. Mendonca, and A. Dos Santos, "Cascaded Highly Nondegenerate Four-Wave-Mixing Phenomenon in Transparent Isotropic Condensed Media", *Opt. Lett.* **25** (11), 829-831 (2000).

[21] J. Liu and T. Kobayashi, "Cascaded Four-Wave Mixing and Multicolored Arrays Generation in a Sapphire Plate by Using Two Crossing Beams of Femtosecond Laser", *Opt. Express* **16** (26), 22119-22125 (2008).

[22] M. Zhi, X. Wang, and A. V. Sokolov, "Broadband Coherent Light Generation in Diamond Driven by Femtosecond Pulses", *Opt. Express* **16** (16), 12139-12147 (2008).

[23] W. Liu, L. Zhu, and C. Fang, "Observation of Sum-Frequency-Generation-Induced Cascaded Four-Wave Mixing Using Two Crossing Femtosecond Laser Pulses in a 0.1 mm Beta-Barium-Borate Crystal", *Opt. Lett.* **37** (18), 3783-3785 (2012).

[24] A. A. Said, T. Xia, A. Dogariu, D. J. Hagan, M. J. Soileau, E. W. Van Stryland, and M. Mohebi, "Measurement of the Optical Damage Threshold in Fused Quartz", *Appl. Opt.* **34** (18), 3374-3376 (1995).

[25] L. Zhu, W. Liu, L. Wang, and C. Fang, "Parametric Amplification-Assisted Cascaded Four-Wave Mixing for Ultrabroad Laser Sideband Generation in a Thin Transparent Medium", *Laser Phys. Lett.* **11** (7), 075301 (2014).

[26] W. Liu, L. Wang, F. Han, and C. Fang, "Distinct broadband third-harmonic generation on a thin amorphous medium-air interface", *Opt. Lett.* **38** (17), 3304-3307 (2013).

[27] W. Liu, L. Wang, and C. Fang, "*In-situ* Weak-Beam and Polarization Control of Multidimensional Laser Sidebands for Ultrafast Optical Switching", *Appl. Phys.*

Lett. **104** (11), 111114 (2014).

[28] G. Cerullo and S. D. Silvestri, "Ultrafast Optical Parametric Amplifiers", *Rev. Sci. Instrum.* **74** (1), 1-16 (2003).

[29] D. V. Khakhulin, A. B. Savel'ev, and R. V. Volkov, "Efficient Broadband Optical Parametric Amplification of Supercontinuum in the Visible by Narrowband Pump", *Laser Phys. Lett.* **4** (5), 345 (2007).

[30] O. E. Martinez, "Grating and Prism Compressors in the Case of Finite Beam Size", *J. Opt. Soc. Am. B* **3** (7), 929-934 (1986).

[31] F. Raoult, A. C. L. Boscheron, D. Husson, C. Sauteret, A. Modena, V. Malka, F. Dorchies, and A. Migus, "Efficient Generation of Narrow-Bandwidth Picosecond Pulses by Frequency Doubling of Femtosecond Chirped Pulses", *Opt. Lett.* **23** (14), 1117-1119 (1998).

[32] S. Laimgruber, H. Schachenmayr, B. Schmidt, W. Zinth, and P. Gilch, "A Femtosecond Stimulated Raman Spectrograph for the Near Ultraviolet", *Appl. Phys. B* **85** (4), 557-564 (2006).

[33] P. Kukura, D. W. McCamant, S. Yoon, D. B. Wandschneider, and R. A. Mathies, "Structural Observation of the Primary Isomerization in Vision with Femtosecond-Stimulated Raman", *Science* **310**, 1006-1009 (2005).

[34] I. R. Lewis and H. Edwards, *Handbook of Raman Spectroscopy: From the Research Laboratory to the Process Line*, 1st ed. (CRC Press, New York, NY, 2001), p.1072.

[35] A. B. Myers and R. A. Mathies, in *Biological Applications of Raman Spectroscopy*, edited by T. G. Spiro (John Wiley & Sons, Inc., New York, 1987), Vol. 2, pp. 1-58.

[36] R. P. McLaughlin, B. P. Nyholm, and P. J. Reid, "Absolute Resonance Raman Intensity Analysis of Isopropyl Nitrate in the Condensed Phase", *J. Phys. Chem. A* **107** (43), 9105-9112 (2003).

[37] S. Shim, C. M. Stuart, and R. A. Mathies, "Resonance Raman Cross-Sections and Vibronic Analysis of Rhodamine 6G from Broadband Stimulated Raman Spectroscopy", *Chem. Phys. Chem.* **9** (5), 697-699 (2008).

[38] Y. Wang, W. Liu, L. Tang, B. G. Oscar, F. Han, and C. Fang, "Early Time Excited-State Structural Evolution of Pyranine in Methanol Revealed by Femtosecond Stimulated Raman Spectroscopy", *J. Phys. Chem. A* **117** (29), 6024-6042 (2013).

[39] B. G. Oscar, W. Liu, L. Tang, Y. Zhao, Y. Wang, R. E. Campbell, and C. Fang, "Excited State Structural Dynamics of a Dual-Emission Calmodulin-Green Fluorescent Protein Sensor for Calcium Ion Imaging", *Proc. Natl. Acad. Sci. U.S.A.*, **111** (28), 10191-10196. doi: 10.1073/pnas.1403712111. (2014).

Chapter 5 Parametric Amplification-Assisted Cascaded Four-Wave Mixing for Ultrabroad Laser Sideband Generation in a Thin Transparent Medium

Liangdong Zhu, Weimin Liu, Liang Wang, and Chong Fang*

Laser Physics Letters, **11** (7), 075301 (6pp), Published on May 22, 2014 DOI: 10.1088/1612-2011/11/7/075301

5.1 Abstract

We demonstrate distinct sets of broadband up-converted multicolour array (BUMA) signals in a thin transparent medium with an intense 800 nm fundamental pulse and a weak unfiltered super-continuum white light (SCWL) in a crossing geometry. Upon varying the time delay between the two incident laser pulses, continuously tunable BUMA signals in the visible to near-IR range sequentially emerge on either side of the fundamental pulse, in both BBO crystal and BK7 glass. Through numerical calculations at intrinsic phase-matching conditions, the BUMA signals on the SCWL side are shown to arise from the interaction mainly between $\chi^{(3)}$-based four-wave optical parametric amplification and cascaded four-wave mixing (CFWM) processes. The temporally controllable broadband BUMA signals with amplification and tunability all in one thin transparent medium are highly suitable for ultrafast laser spectroscopy and optical communication networks.

5.2 Introduction

Ultrafast laser sideband generation has found myriad applications in optical communication,[1-4] molecular spectroscopy,[5-7] and biomedical imaging.[8,9] By applying ultrafast optical lasers in different kinds of nonlinear media through various interaction mechanisms, the output beams span a wide spectral range and promote photonic applications.[10-14] Recently, nonlinear third-order ($\chi^{(3)}$) optical processes via cascaded four-wave mixing (CFWM) or Raman processes were observed to generate spatially dispersed multicolour arrays from UV to near IR[15-21] in various anisotropic and isotropic media. To amplify the signal, four-wave mixing optical parametric amplification (FWM-

OPA) has been achieved in noble gas and bulk solid-state media and was widely used in fiber optics[22,23] that exploits the material $\chi^{(3)}$ nonlinearity. Also, mixed cascading $\chi^{(2)}$ and $\chi^{(3)}$ processes to produce sideband pulses were demonstrated in β-barium borate (BBO) crystal.[24] It is thus desirable to simultaneously achieve the generation and interaction between various nonlinear processes *in situ* to propagate ultrafast laser sidebands into distinct directions and enhance coherent optical control for practical applications.

In this Letter, we use an unfiltered, chirped super-continuum white light (SCWL, ca. 500—950 nm) to interact with a much stronger fundamental pulse (FP) at various crossing angles in a thin transparent medium. Besides the previously reported broadband up-converted multicolour array (BUMA) on the FP side,[20] we demonstrate a new temporally controllable set of BUMA signals that are attributed to FP interacting with the visible part of SCWL, revealed to arise from a unique noncollinear OPA (NOPA)-assisted four-wave-mixing cascading process. The effective mixing of FWM-OPA with CFWM greatly enhances the tunability of output laser sidebands to be broader and stronger, which also exhibit a characteristic frequency-dependent spatial variation.

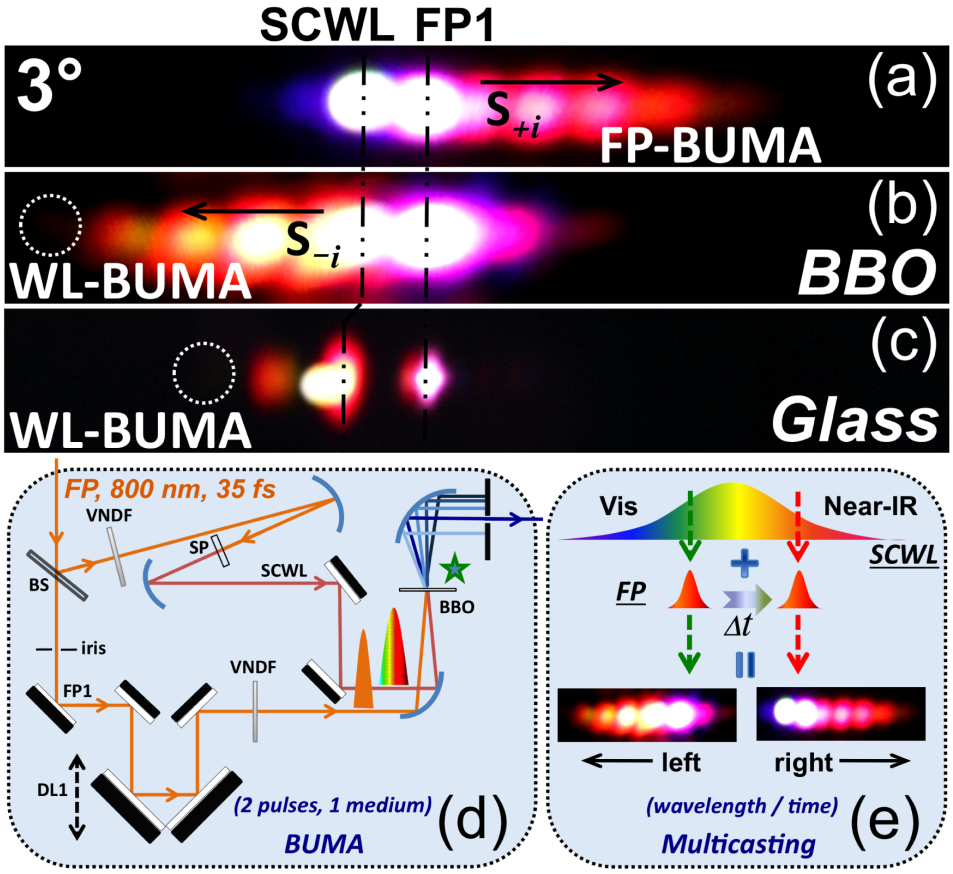

Figure 5.1 Photographs and schematic of (a) FP-BUMA with a crossing angle of 3˚ between the two incident beams in BBO; (b) WL- BUMA in BBO; and (c) WL-BUMA in BK7 glass. (d) Schematic of the optical setup for BUMA generation. BS, beam-splitter; SP, sapphire plate; VNDF, variable neutral density filter; DL, delay line stage. (e) Potential application if tailored to operate in the ~1.5 μm region for wavelength/time-multicasting or multiplexing [4] with temporally controllable BUMA signal generation.

5.3 Experimental results

The prototype of BUMA generation[20] employs a femtosecond mode-locked Ti:sapphire amplifier, providing 35 fs, 800 nm pulses at 1 kHz repetition rate (Figure 5.1d). Part of the laser output with ~1 μJ pulse energy is focused by a concave mirror onto a 2-mm-thick *Z*-cut sapphire plate to generate SCWL followed by beam collimation. The notable difference from previous work[20] is that no longpass filter is used so both the near-IR and visible parts of weak SCWL across ca. 500—950 nm range can contribute to the laser sideband generation. A stronger portion of the FP (~40 μJ/pulse, FP1) is used as the pump beam and attenuated by an iris and a variable-neutral-density filter. The two *p*-polarized beams with a crossing angle of ca. 3—8° are loosely focused onto a 0.1-mm-thick BBO crystal (Type I, θ=27.7°) by an f=10 cm concave mirror. The beam diameters at the foci are measured to be ~150 μm (e.g., using a blade on a translation stage). When collecting the spectrum of each sideband, a pinhole is used before the spectrometer to filter out unwanted spectral components. Notably, the crystal cutting angle slightly differs from the optimal value of 29.2° for maximal second-harmonic generation (SHG) at 800 nm; however, we aim to enhance interaction between the 800 nm fundamental pulse and broadband SCWL. This work adopts the phase-matching angle to minimize SHG in BBO. Control experiments are performed in a 0.15-mm-thick BK7 glass plate.

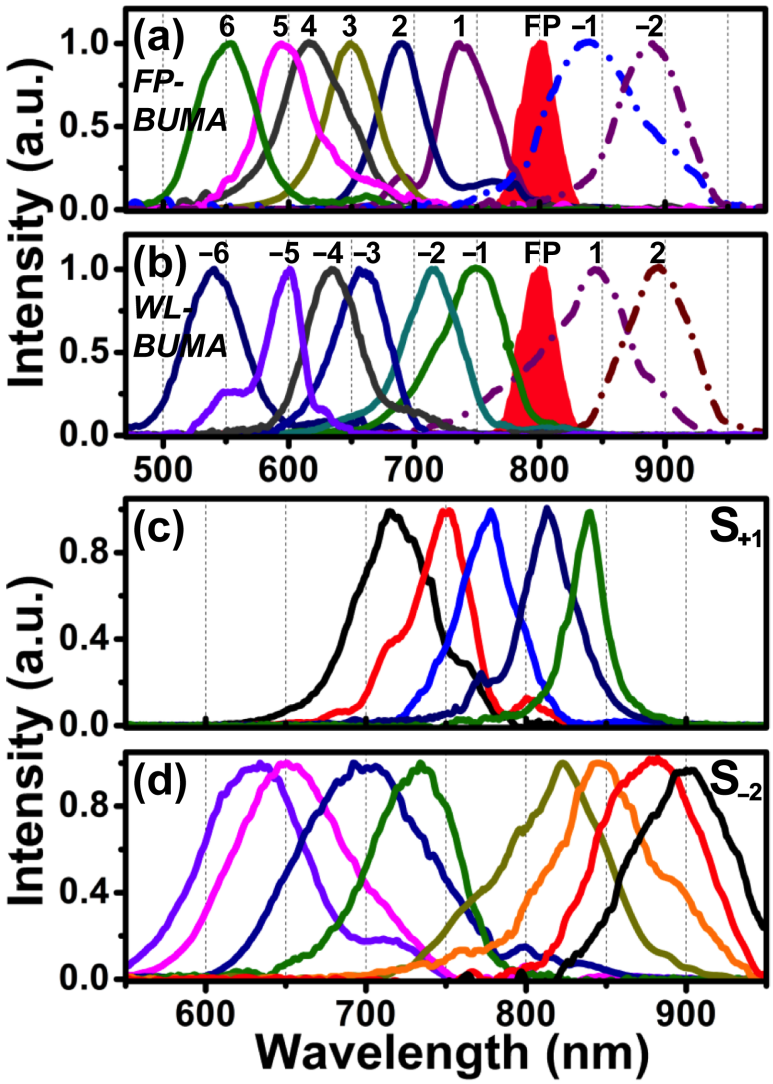

Figure 5.2 Normalized spectra of (a) FP-BUMA, and (b) WL-BUMA signals in BBO with an incident beam-crossing angle of 3˚. Two additional CFWM sidebands emerging on the opposite side of the fundamental pulse are shown in dash-dotted lines. The FP at ~800 nm is in red, while the ultrabroad SCWL is not shown. Normalized spectra of tunable (c) S_{+1} and (d) S_{-2} sidebands at different delay time between the two incident pulses.

Previously, BUMAs were generated by rotating BBO or time-delaying the two incident pulses at various phase-matching conditions.[20] In particular, when we set the BBO at the rotation angle to minimize SHG, a dominant CFWM array (ca. 360—780 nm) appeared on the FP1 side (see Figure 5.1a). We hereby reduce the crossing angle from 6˚ to 3˚ but keep FP1 pulse energy at ~7 μJ,[20] and observe a reduced number of sidebands that coalesce in space and frequency[7] which is now labeled as FP-BUMA (Figure 5.1a, S_{+i}). In this experiment, upon delaying FP1 ~100 fs away from the time point for maximal FP-BUMA generation, we discover a new set of brighter BUMA (S_{-i}) on the SCWL side that is called WL-BUMA (Figure 5.1b) while FP-BUMA signals diminish. The crossing-angle-dependent measurement of WL-BUMA yields an optimal tuning range of ca. 3—4˚. The normalized spectra of FP-BUMA at 3˚ are shown in Figure 5.2a. Besides six sidebands, two concomitant CFWM sidebands in the near-IR wavelength range on the SCWL side are also collected, spanning a combined spectral region of ca. 550—900 nm. The WL-BUMA displays a similar wavelength range (Figure 5.2b), and these sidebands all have ultrabroad bandwidth of ca. 1000—2000 cm^{-1}, corresponding to the Fourier transform-limited pulse duration of ca. 7—15 fs if assumed Gaussian line shape and simple chirp structure. This type of sideband generation with sub-20 fs time duration has been demonstrated in much thicker media (e.g., 1-mm-thick fused silica plate) with chirped incident pulses.[25] The S_{+1} integrated intensity is measured to show a similar temporal profile (~80 fs fwhm) to the SCWL cross correlation with FP1,[20] indicative of a common chirp and pulse compressibility. The ultrabroad bandwidth of all the laser sidebands achieved herein is thus mainly due to the femtosecond broadband incident pulses (i.e. both FP1 and SCWL), thinness of the transparent medium providing small enough phase mismatching, and

an optimized crossing angle to satisfy $\chi^{(3)}$-based phase matching over a broad frequency range for BUMA generation.[7,26]

Furthermore, broadband tunability of these sidebands can be readily achieved by varying the time delay between FP1 and SCWL (Figure 5.2c and d). The S_{+1} in FP-BUMA can be continuously tuned (ca. 700—850 nm) within ~100 fs of time delay, indicating the participation of the visible wavelength components in unfiltered SCWL to push S_{+1} beyond 800 nm.[7] Notably, the smaller crossing angle of 3˚ leads to a relatively smaller tuning range in comparison to the previously observed range with a larger crossing angle, e.g., 6—7˚.[7,20] The S_{-2} in WL-BUMA exhibits a broader wavelength tunability of >300 nm. This broader tunability of S_{-2} arises from two facts: first, the spectral range of SCWL in the visible (ca. 500—780 nm) is larger than that in the near IR region (ca. 820—950 nm); second, during WL-BUMA generation the assist from amplification process facilitates the expanded wavelength tunability. On the potential application side, the root-mean-square (RMS) power stability of the sideband signals is measured to be <1.5% over a typical time period of one hour, similar to the incident SCWL stability,[20] while the pulse energy of the sidebands is below ~50 nJ (typical value)[7] with self compression.[19] The weak BUMA signals are thus highly suitable to act as probe pulses in ultrafast spectroscopy.[6,7]

5.4 Phase matching condition

The similar spectral range of S_{+i} and S_{-i} is intriguing, which can be explained by the underlying physics. The FP-BUMA signals stem from CFWM between FP1 and the near-IR component of

chirped SCWL.[20] Since the newly observed WL-BUMA emerges as FP1 is tuned away by ~100 fs, the involving CFWM processes likely arise from the interaction between FP1 and the visible part of SCWL (see Figure 5.1e). This crucial point is confirmed by two control experiments that (i) WL-BUMA cannot be observed if SCWL is filtered[20] with a longpass filter (RG830, Newport, Inc.), and (ii) only WL-BUMA is observed if a visible bandpass filter is inserted into the SCWL beam path. More quantitative analysis of the observed BUMA signals requires theoretical calculations of the nascent sideband wavelength using the relevant phase-matching equation, which is described in detail below.

In CFWM processes, two sets of temporally separated BUMAs generated by the fundamental pulse and unfiltered SCWL are governed by the intrinsic phase-matching conditions: $k_m=(m+1)k_1-mk_2(t)$, where $m=0, \pm1, \pm2\ldots$ is the beam order of the sideband signal, and k_m, k_1, and $k_2(t)$ represent the laser sideband, FP1, and the time-delayed SCWL component, respectively. Given that the two incident laser beams copropagate and interact noncollinearly,[15,19] the phase-matching equation for the mth-order up-converted beam with the crossing angle α is given by

$$k_m = \left\{ \left[(m+1)k_1 + mk_2(t) \right]^2 - 4m(m+1)k_1 k_2(t) \cos^2\left(\frac{\alpha}{2}\right) \right\}^{\frac{1}{2}} \tag{5.1}$$

The experimental and calculated center wavelengths of the sidebands using Eq. (5.1) are shown in Figure 5.3. Two sets of largely symmetrical BUMA signals on either side of FP1 match well with calculations on the FP1 interacting with different parts of SCWL with a beam crossing angle of 3°.

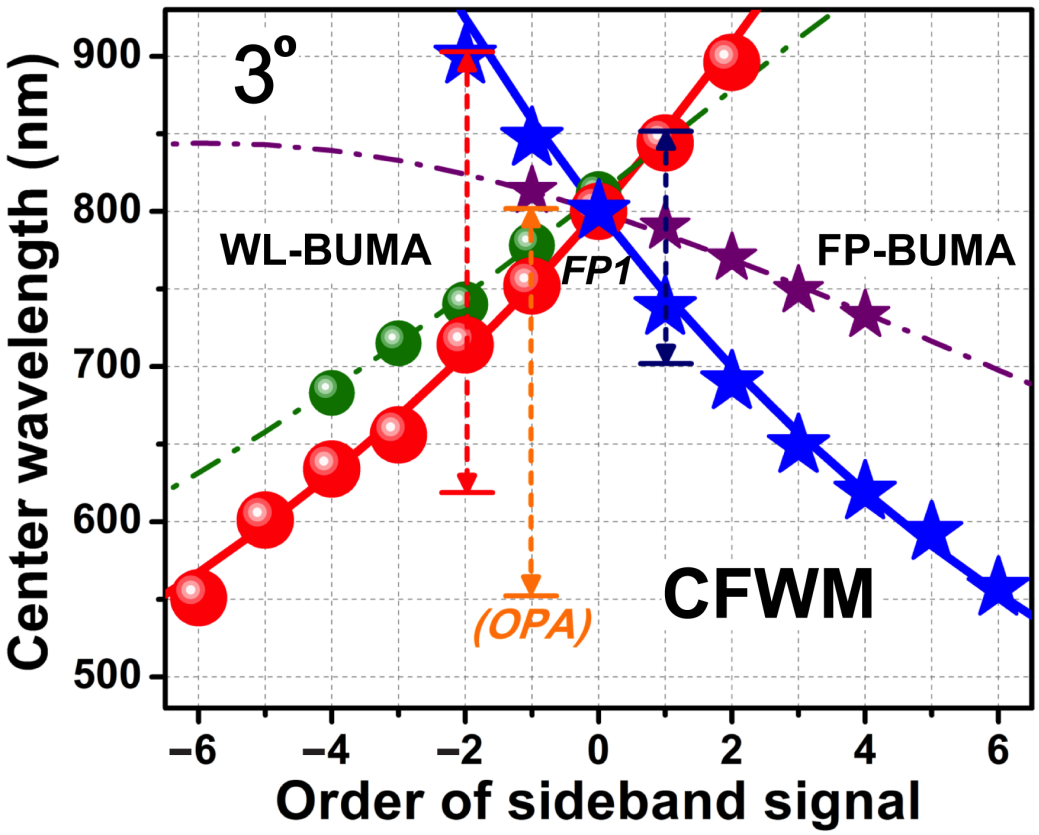

Figure 5.3 Broadband tunability of distinct sets of BUMAs at the incident beam-crossing angle of 3°. Blue stars (red circles) represent the experimental center wavelengths of FP-BUMA (WL-BUMA). Solid lines are theoretical calculations on the CFWM interaction between strong FP and weak SCWL with a crossing angle of 3° using the phase-matching Eq. (5.1). Violet stars (green circles) show the experimental data of FP-BUMA (WL-BUMA) generated from two interacting FPs in the control experiment as discussed in the main text. Calculations of the control experiment data yield the two contributing fundamental pulse center wavelengths of 813 and 800 nm (778 and 811 nm) for FP-BUMA (WL-BUMA) signals. The tunability of S_{-2} and S_{+1} sidebands is depicted by double-arrowed vertical dashed lines. The tunable range for S_{-1} the parametrically amplified signal is shown by the orange vertical dashed line.

Moreover, we perform an important control experiment by moving the sapphire plate away from the beam focal point so a chirped weak fundamental pulse instead of SCWL is utilized to generate BUMA with the intense FP1. Two sets of BUMAs solely from the two fundamental pulses (Figure 5.3, dash-dotted lines) are observed instead in the wavelength range of ca. 680—820 nm with the bandwidth of ~1000 cm^{-1}, which is still much broader than a previous report using two strong chirped near-IR pulses.[27] Calculations based on Eq. (5.1) reveal that the two interacting pulses for nearly degenerate CFWM are both within the FP bandwidth (800 nm center wavelength, 32 nm full-width-at-half-maximum or FWHM), and the varying time delay determines the exact FP frequency component for the CFWM interaction. This explains the significantly reduced tunable range than the BUMA signals generated from a strong fundamental pulse and a weak, much broader SCWL. Specifically, two dashed lines on the S_{-2} and S_{+1} signals manifest the individual broad tunable range (ca. 300 and 150 nm) from visible to near IR achievable by simply varying the time delay between the two incident laser pulses, mainly supported by the ultrabroad bandwidth of unfiltered SCWL.

5.5 Parametric amplification process

What is the fundamental basis for the observation of WL-BUMA using the visible part of SCWL? We capture the dramatic parametric amplification of SCWL spectral components (S_{-1} signal) pumped by FP1, which essentially supports the subsequent WL-BUMA generation. About 15 times intensity amplification is observed by measuring the S_{-1} spectrum centered at ~740 nm with

and without FP1 at ~24 μJ/pulse (Figure 5.4a). The unamplified SCWL seed spectrum is collected for calculation of the signal gain. The SCWL seed center wavelength of ~740 nm is chosen due to its highest gain; the S_{-1} amplification gain drops to ~2 when the seed pulse is blue-tuned to ~540 nm. The observed amplification of SCWL in BBO is reminiscent of the efficient broadband FWM-OPA of a weak seed pulse in bulk Kerr medium such as silicon or fused silica,[23,26] although the medium thickness is much smaller in our setup.

Notably, the S_{+1} in Figure 5.2b exhibits broader width, likely due to the contribution from both the CFWM sideband at the FP side and the idler pulse from the aforementioned FWM-OPA process. The calculation of the wavelength of the nascent sideband from energy conservation relation is $2\omega_p=\omega_s+\omega_i$, wherein the pump ($\omega_p$) and signal ($\omega_s$) beam is respectively at 800 nm (FP) and 740 nm (S_{-1}), the idler (ω_i) beam center wavelength will be ~870 nm. This result agrees well with the spectral data in Figure 5.2b. A more in-depth calculation taken into account the experimental noncollinear phase-matching geometry of the involving beams is carried out using Eq. (5.1), and the corresponding CFWM sideband center wavelengths are shown in Figure 5.3.

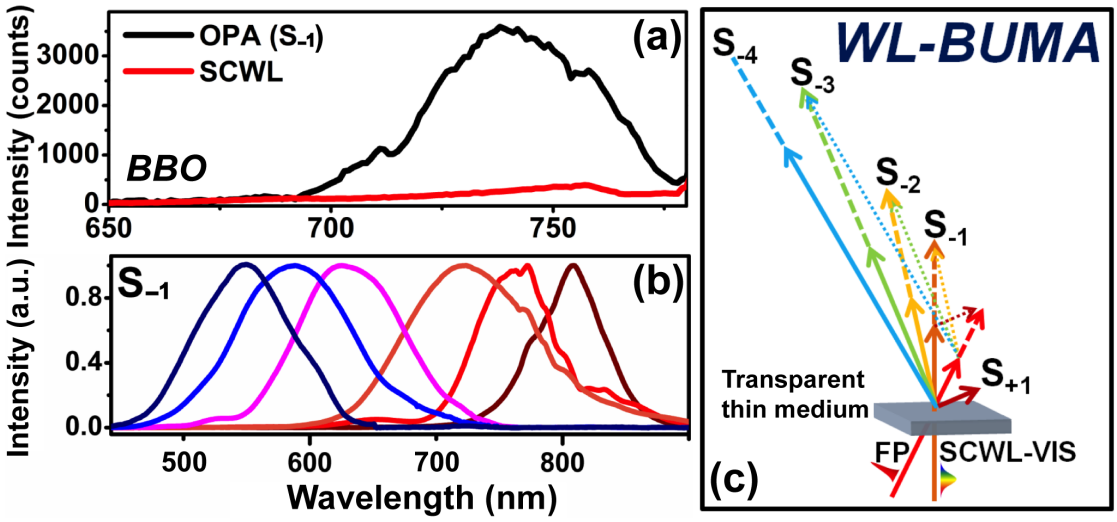

Figure 5.4 Parametric amplification of the S_{-1} signal for WL-BUMA generation. (a) The incident SCWL seed and amplified S_{-1} spectrum with the center wavelength of ~740 nm in BBO. (b) Tunable range of S_{-1} with various delay time between FP and SCWL. (c) Wavevector diagrams illustrating the phase-matching conditions responsible for FWM-OPA to generate amplified S_{-1} and the subsequent CFWM sidebands in a thin transparent medium.

To ascertain the optical basis and generation mechanism for wavelength-tunable WL-BUMA, Figure 5.4b shows that upon varying the time overlap between FP1 and SCWL, the FWM-OPA supports tunable broadband signal amplification of S_{-1} across a wide wavelength range of ca. 550—800 nm. This translates to the broadband tunability of the cascaded higher-order sidebands ($m = -2, -3, ...$) as marked in Figure 5.3. It is notable that the observed tunable range for S_{-2} reaches ~910 nm because WL-BUMA eventually transitions to FP-BUMA as we continuously tune the incident pulse delay across a ~260 fs time window. The cascading phase-matching geometries from the incident fundamental pulse and SCWL are sketched in Figure 5.4c, which are responsible for the spatially separated WL-BUMA sidebands. Notably, without the parametric amplification of S_{-1} that is collinear with SCWL (see Figure 5.4a), the much weaker SCWL does not possess enough energy to contribute two photons during phase matching to generate the observed WL-BUMA signals. Furthermore, the broader bandwidth observed for S_{-2} than S_{+1} (Figure 5.2d vs. c) may be indicative of the additional contribution from cross-phase modulation[28,29] in conjunction with FWM-OPA to simultaneously amplify and compress weak sideband pulses. This has been previously reported using much stronger incident pulses with a similar crossing angle (~3˚) in a thicker glass plate.[25]

To experimentally evaluate the OPA efficiency, one relevant yet indirect parameter is the FP1 energy loss passing through the thin medium with and without SCWL. Though the FP1 energy loss is not identical to the sideband signal conversion efficiency,[25] it is very useful to infer the signal generation mechanism. The measurement in BBO yields ~6% FP1 depletion for FP-BUMA generation, which is ~2 times larger than that for WL-BUMA generation. In contrast, as we sample

all the phase-matching angles in a 0.15-mm-thick BK7 glass, the FP1 depletion for maximal FP-BUMA or WL-BUMA generation remains <1% (Figure 5.1c). Therefore, FWM-OPA process cannot be solely responsible for signal amplification in BBO because otherwise the FP1 energy loss will be comparable in transparent media such as BBO and glass, which have a similar bulk $\chi^{(3)}$ nonlinearity within a factor of 2.[30,31] We speculate that an additional $\chi^{(2)}$-based OPA process could further amplify S_{-1} and enhance the cascaded $\chi^{(3)}$-based WL-BUMA generation in BBO crystal. The validity of this hypothesis can be provided by the analysis of current experimental parameters. Notably even at the BBO rotation angle to minimize SHG, the intense *p*-polarized FP1 still generates some *s*-polarized 400 nm pulse in BBO. Given the incident beam-crossing angle of 3—4˚, phase matching can be satisfied between an *s*-polarized pump and a *p*-polarized seed pulse from ca. 550—800 nm,[10] because the required phase-matching angle in a type-I BBO is ca. 26.6—28.0˚ (close to 27.7˚ our BBO cutting angle) and we are also using femtosecond broadband pulses. The resulting S_{-1} signal is *p*-polarized, and it interacts with FP1 via CFWM pathway (Figure 5.4c) to generate the *p*-polarized higher-order WL-BUMA signals. We can thus conclude that an additional $\chi^{(2)}$-based OPA process likely co-exists with the ubiquitous $\chi^{(3)}$-based FWM-OPA for BUMA generation.

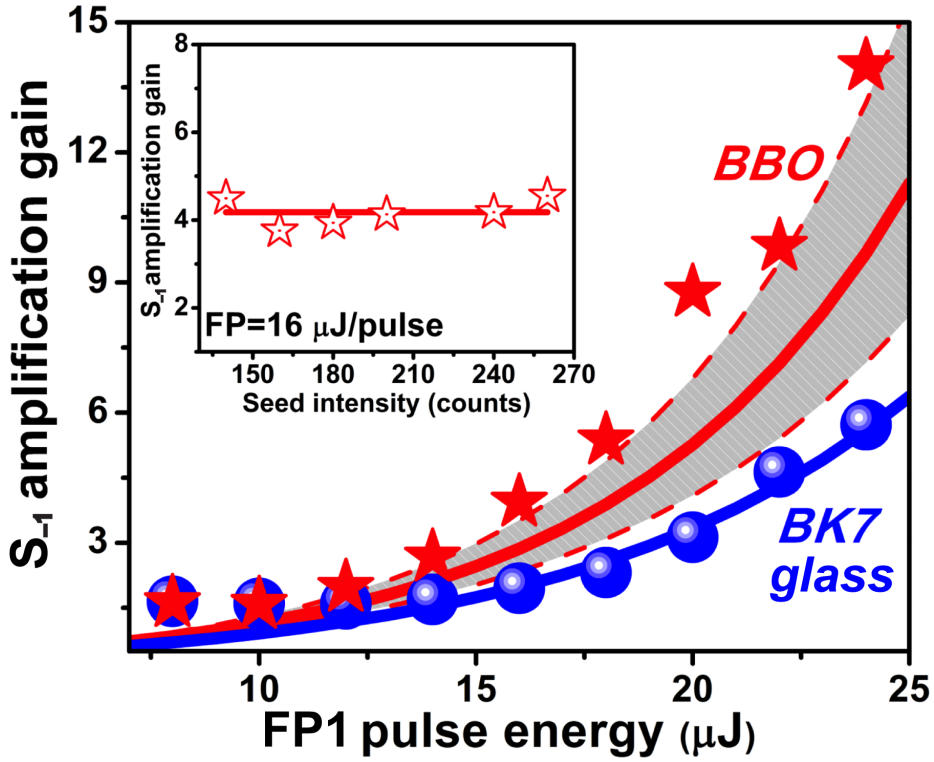

Figure 5.5 Power-dependent parametric amplification gain curve of S-1 in BBO crystal and BK7 glass with the incident beam-crossing angle at 4˚. The FP1-power-dependent S_{-1} signal gain in BBO (glass) are shown in red stars (blue circles), and the simulation results based on bulk $\chi^{(3)}$ nonlinearity of BBO (glass) with 800 nm pump wavelength are shown in solid red (blue) lines. The shaded area surrounding the red trace indicates calculation results within ±10% uncertainty of the average n_2 value (see text).[31] The SCWL-seed-power-dependent S_{-1} gain in BBO with the fundamental pulse energy of 16 μJ is shown in the inset.

To quantitatively dissect the $\chi^{(3)}$ nonlinearity contribution, we measure the FP1-power-dependent S_{-1} signal amplification in BBO, and in BK7 glass as a control experiment. Since the isotropic glass lacks quadratic nonlinearity, the S_{-1} amplification can only be due to $\chi^{(3)}$-based FWM-OPA. By varying the FP1 pulse energy from 7—25 μJ, we observe an exponentially increasing S_{-1} signal amplification gain (see Figure 5.5) from ca. 2—15 in BBO (red filled stars) and 2—6 in BK7 glass (blue filled circles), respectively. Experimental results also reveal that the S_{-1} amplification gain is independent of the SCWL seed pulse power in this weak seed regime (inset of Figure 5.5).[26]

Considering that the incident strong fundamental pulse remains largely undepleted, the S_{-1} wavelength of ~740 nm is close to $\lambda_{FP} \approx$ 800 nm, the amplified signal gain at the phase-matching condition owing to bulk $\chi^{(3)}$ nonlinearity[22,23] can be estimated as

$$G_{Signal} \approx \exp(2\gamma P_{FP} l)/4 \tag{5.2}$$

$$\gamma = \omega_{pump} n_2 / c A_{eff} \tag{5.3}$$

where γ is the $\chi^{(3)}$-derived effective nonlinearity coefficient, ω_{pump} is the angular frequency of the pump pulse, A_{eff} is the effective area of the propagating beam, n_2 is the nonlinear index coefficient, P_{FP} is the peak power of the pump pulse, and l is the interaction length of two incident beams that equals the medium thickness. In our setup, the incident fundamental pulse energy of 7—25 μJ corresponds to the pump peak power of ca. 0.2—0.71 GW owing to its 35 fs pulse duration. This very high peak density is the main factor contributing to significant signal gain observed in the 0.1-mm-thick BBO crystal and 0.15-mm-thick glass, which is much thinner than the media used in previous reports.[23,24,26] The simulation results for BK7 glass show excellent agreement with the

experimental data (Figure 5.5, blue), however, the S_{-1} amplification gain observed in BBO clearly differs from the solely $\chi^{(3)}$-based simulation (Figure 5.5, red).[31] Given the large spread of the reported n_2 values, we take the average value of 6.0×10^{-20} m^2/W and calculate the BBO signal gain curve with 800 nm pump wavelength (solid red curve, Figure 5.5). The data points approximately ride above the top of the shaded area (upper dashed red curve), which represents the calculation results with $n_2 = 6.6\times10^{-20}$ m^2/W. This means that in order to attribute the observed S_{-1} gain to purely $\chi^{(3)}$-based phenomenon, the average n_2 value has to be enlarged by at least 10%. An alternative and more reasonable interpretation based on our observation is that $\chi^{(2)}$-based OPA plays an auxiliary role in the WL-BUMA amplification processes, because BBO is a quadratic medium with a large $\chi^{(2)}$ coefficient. The aforementioned fundamental pulse energy loss data in BBO crystal contrasting with BK7 glass corroborate this mechanistic interpretation. Moreover, our BBO cutting angle at 27.7° favors SHG of an 800—1000 nm broadband pulse. Therefore, as the near-IR part of SCWL (i.e., 800—1000 nm wavelength range) overlaps with the fundamental pulse to generate FP-BUMA, it may readily satisfy the phase-matching condition for the $\chi^{(2)}$-based amplification of the observed sideband signals[20,25] in addition to the $\chi^{(3)}$-based FWM-OPA contribution.

5.6 Conclusions

In summary, we report a new optical methodology to generate two distinct sets of temporally controllable BUMA signals at the condition disfavoring SHG in a 0.1-mm-thick type-I BBO

crystal with two femtosecond laser pulses. The dominant process is revealed to be cascaded four-wave mixing between the strong fundamental pulse and the near-IR or OPA-coupled visible component of the weak, chirped SCWL. Ultrabroad bandwidth of 1000—2000 cm^{-1} is readily obtained for all the sidebands in their individual phase-matching directions. Based on the pump-power-dependent S_{-1} signal amplification and the simulation results in BBO crystal and BK7 glass, we reveal that the newly observed WL-BUMA mainly arises from $\chi^{(3)}$-based FWM-OPA-coupled CFWM processes, while $\chi^{(2)}$-assisted OPA likely contributes to S_{-1} signal amplification and WL-BUMA generation in BBO as well. These broadband BUMA signals with versatile intrinsic amplification and wide experimental tunability can be readily used as probe beams in multicolour ultrafast spectroscopy,[6,7] can be coherently combined to generate single-cycle pulses[18] and also be potentially implemented[32] (see Figure 5.1e) in optical communication networks.[1,4]

5.7 References

[1] J. Zheng, K. Kwak, J. Asbury, X. Chen, I. R. Piletic, and M. D. Fayer, "Ultrafast Dynamics of Solute-Solvent Complexation Observed at Thermal Equilibrium in Real Time", *Science* **309** (5739), 1338-1343 (2005).

[2] G. P. Agrawal, *Nonlinear Fiber Optics*, 4th ed. (Academic Press, Waltham, MA, 2006).

[3] G. Ma, J. Shen, Z. Zhang, Z. Hua, and S. H. Tang, "Ultrafast All-Optical Switching in One-Dimensional Photonic Crystal with Two Defects", *Opt. Express* **14** (2), 858-865 (2006).

[4] S. Gao and X. Xiao, "All-Optical Wavelength Multicasting Based on Cascaded Four-Wave Mixing with a Sngle Pump in Highly Nonlinear Fibers", *Opt. Commun.* **285** (5), 784-789 (2012).

[5] W. Xiong and M. T. Zanni, "Signal Enhancement and Background Cancellation in Collinear Two-Dimensional Spectroscopies", *Opt. Lett.* **33** (12), 1371-1373 (2008).

[6] W. Wang, W. Liu, I.-Y. Chang, L. A. Wills, L. N. Zakharov, S. W. Boettcher, P. H.-Y. Cheong, C. Fang, and D. A. Keszler, "Electrolytic Synthesis of Aqueous Aluminum Nanoclusters and *in situ* Characterization by Femtosecond Raman Spectroscopy & Computations", *Proc. Natl. Acad. Sci. U.S.A.* **110** (46), 18397-18401 (2013).

[7] L. Zhu, W. Liu, and C. Fang, "Tunable Sideband Laser from Cascaded Four-Wave Mixing in Thin glass for Ultra-Broadband Femtosecond Stimulated Raman Spectroscopy", *Appl. Phys. Lett.* **103** (6), 061110 (2013).

[8] W. Min, S. Lu, M. Rueckel, G. R. Holtom, and X. S. Xie, "Near-Degenerate Four-Wave-Mixing Microscopy", *Nano Lett.* **9** (6), 2423-2426 (2009).

[9] P. Mahou, N. Olivier, G. Labroille, L. Duloquin, J.-M. Sintes, N. Peyriéras, R. Legouis, D. Débarre, and E. Beaurepaire, "Combined Third-Harmonic Generation and Four-Wave Mixing Microscopy of Tissues and Embryos", *Biomed. Opt. Express* **2** (10), 2837-2849 (2011).

[10] G. Cerullo and S. D. Silvestri, "Ultrafast Optical Parametric Amplifiers", *Rev. Sci. Instrum.* **74** (1), 1-16 (2003).

[11] Z. Jin, H. Ma, G. Li, Y. Xu, G. Ma, and Z. Cheng, "Ultrafast Dynamics of the Mn_{3+} d-d Transition and Spin-Lattice Interaction in $YMnO_3$ Film", *Appl. Phys. Lett.* **100** (2), 021106 (2012).

[12] G. K. Kitaeva, "Terahertz Generation by Means of Optical Lasers", *Laser Phys. Lett.* **5** (8), 559-576 (2008).

[13] G. K. Kitaeva, S. P. Kovalev, I. I. Naumova, R. A. Akhmedzhanov, I. E. Ilyakov, B. V. Shishkin, and E. V. Suvorov, "Quasi-Phase-Matched Probe-Energy Electro-Optic Sampling as a Method of Narrowband Terahertz Detection", *Appl. Phys. Lett.* **96** (7), 071106 (2010).

[14] T.-D. Wang, Y.-C. Huang, M.-Y. Chuang, Y.-H. Lin, C.-H. Lee, Y.-Y. Lin, F.-Y. Lin, and G. K. Kitaeva, "Long-Range Parametric Amplification of THz Wave with Absorption Loss Exceeding Parametric Gain", *Opt. Express* **21** (2), 2452-2462 (2013).

[15] H. Crespo, J. T. Mendonca, and A. Dos Santos, "Cascaded Highly Nondegenerate Four-

Wave-Mixing Phenomenon in Transparent Isotropic Condensed Media", *Opt. Lett.* **25** (11), 829-831 (2000).

[16] M. Zhi and A. V. Sokolov, "Broadband Coherent Light Generation in a Raman-Active Crystal Driven by Two-Color Femtosecond Laser Pulses", *Opt. Lett.* **32** (15), 2251-2253 (2007).

[17] J. Liu and T. Kobayashi, "Cascaded Four-Wave Mixing and Multicolored Arrays Generation in a Sapphire Plate by Using Two Crossing Beams of Femtosecond Laser", *Opt. Express* **16** (26), 22119-22125 (2008).

[18] R. Weigand, J. T. Mendonca, and H. M. Crespo, "Cascaded Nondegenerate Four-Wave-Mixing Technique for High-Power Single-Cycle Pulse Synthesis in the Visible and Ultraviolet Ranges", *Phys. Rev. A* **79** (6), 063838 (2009).

[19] W. Liu, L. Zhu, and C. Fang, "Observation of Sum-Frequency-Generation-Induced Cascaded Four-Wave Mixing Using Two Crossing Femtosecond Laser Pulses in a 0.1 mm Beta-Barium-Borate Crystal", *Opt. Lett.* **37** (18), 3783-3785 (2012).

[20] W. Liu, L. Zhu, L. Wang, and C. Fang, "Cascaded Four-Wave Mixing for Broadband Tunable Laser Sideband Generation", *Opt. Lett.* **38** (11), 1772-1774 (2013).

[21] A. Ryabtsev, B. Nie, and M. Dantus, "45 fs Optical Pulses from Phase Corrected Broadband Cascaded Four Wave Mixing Products", *Laser Phys. Lett.* **10** (12), 125109 (2013).

[22] J. Hansryd, P. A. Andrekson, M. Westlund, J. Li, and P.-O. Hedekvist, "Fiber-Based Optical Parametric Amplifiers and Their Applications", *IEEE J. Sel. Topics Quantum Electron.* **8** (3), 506-520 (2002).

[23] M. A. Foster, A. C. Turner, J. E. Sharping, B. S. Schmidt, M. Lipson, and A. L. Gaeta, "Broad-Band Optical Parametric Gain on a Silicon Photonic Chip", *Nature* **441** (7096), 960-963 (2006).

[24] A. Varanavičius, A. Dubietis, A. Beržanskis, R. Danielius, and A. Piskarskas, "Near-Degenerate Cascaded Four-Wave Mixing in an Optical Parametric Amplifier", *Opt. Lett.* **22** (21), 1603-1605 (1997).

[25] J. Liu and T. Kobayashi, "Generation and Amplification of Tunable Multicolored Femtosecond Laser Pulses by Using Cascaded Four-Wave Mixing in Transparent Bulk Media", *Sensors* **10** (5), 4296-4341 (2010).

[26] H. Valtna, G. Tamošauskas, A. Dubietis, and A. Piskarskas, "High-Energy Broadband Four-Wave Optical Parametric Amplification in Bulk Fused Silica", *Opt. Lett.* **33** (9), 971-973 (2008).

[27] H. Zhang, H. Liu, J. Si, W. Yi, F. Chen, and X. Hou, "Low Threshold Power Density for the Generation of Frequency Up-Converted Pulses in Bismuth Glass by Two Crossing Chirped Femtosecond Pulses", *Opt. Express* **19** (13), 12039-12044 (2011).

[28] R. R. Alfano, P. L. Baldeck, P. P. Ho, and G. P. Agrawal, "Cross-Phase Modulation and Induced Focusing due to Optical Nonlinearities in Optical Fibers and Bulk Materials", *J. Opt. Soc. Am. B* **6** (4), 824-829 (1989).

[29] M. Spanner, M. Y. Ivanov, V. Kalosha, J. Hermann, D. A. Wiersma, and M. Pshenichnikov, "Tunable Optimal Compression of Ultrabroadband Pulses by Cross-Phase Modulation", *Opt. Lett.* **28** (9), 749-751 (2003).

[30] M. Thalhammer and A. Penzkofer, "Measurement of Third-Order Nonlinear Susceptibilities by Non-Phase Matched Third-Harmonic Generation", *Appl. Phys. B* **32** (3), 137-143 (1983).

[31] M. Bache, H. Guo, B. Zhou, and X. Zeng, "The Anisotropic Kerr Nonlinear Refractive Index of the Beta-Barium Borate (β-BaB_2O_4) Nonlinear Crystal", *Opt. Mater. Express* **3** (3), 357-382 (2013).

[32] W. Liu, L. Wang, and C. Fang, "*In-Situ* Weak-Beam and Polarization Control of Multidimensional Laser Sidebands for Ultrafast Optical Switching", *Appl. Phys. Lett.* **104** (11), 111114 (2014).

Chapter 6 Sum-Frequency-Generation-Based Laser Sidebands for Tunable Femtosecond Raman Spectroscopy in the Ultraviolet

Liangdong Zhu, Weimin Liu, Yanli Wang and Chong Fang*

Applied Science, **5** (2), 48-61, Published on April 16, 2015 Part of the "Multi-Color Laser Emission for the Generation of Ultrashort Optical Pulse" Special Issue. DOI: 10.3390/app5020048. (Open Access)

6.1 Abstract

Femtosecond stimulated Raman spectroscopy (FSRS) is an emerging molecular structural dynamics technique for functional materials characterization typically in the visible to near-IR range. To expand its applications we have developed a versatile FSRS setup in the ultraviolet (UV) region. We use the combination of a narrowband, ~400 nm Raman pump from a home-built second harmonic bandwidth compressor (SHBC) and a tunable broadband probe pulse from sum-frequency-generation-based cascaded four-wave mixing (SFG-CFWM) laser sidebands in a thin BBO crystal. The ground state Raman spectrum of a laser dye Quinolon 390 in methanol that strongly absorbs at ~355 nm is systematically studied as a standard sample to provide previously unavailable spectroscopic characterization in the vibrational domain. Both the Stokes and anti-Stokes Raman spectra can be collected by selecting different orders of SFG-CFWM sidebands as the probe pulse. The stimulated Raman gain with the 402 nm Raman pump is >21 times larger than that with the 550 nm Raman pump when measured at the 1,317 cm^{-1} peak for the aromatic ring deformation and ring-H rocking mode of the dye molecule, demonstrating that pre-resonance enhancement is effectively achieved in the unique UV-FSRS setup. This added tunability in the versatile and compact optical setup enables FSRS to better capture transient conformational snapshots of photosensitive molecules that absorb in the UV range.

6.2 Introduction

The advent of femtosecond (fs) lasers has ushered in an exciting era of modern quantum chemistry and molecular spectroscopy [1,2] which has provided previously unavailable or hidden insights about structural dynamics, chemical reactivity, material properties and biological functionality.[2-7] The ultrafast time duration of the incident laser pulses is key to dissect the electronic potential energy surface of the molecular system under investigation, and a time-delayed pump-probe setup is typically implemented to measure the system response on the intrinsic molecular timescale. In comparison to the widely used transient absorption technique that records the electronic responses as a function of time, vibrational spectroscopy is intimately related to molecular structure and the associated normal modes, making the observed vibrational frequencies highly sensitive to the local environment of the chemical bond. By incorporating a preceding actinic pump pulse that induces photochemistry or other chemical reactions, vibrational transitions of the molecular system can be tracked in real time via IR absorption or Raman processes with ultrafast IR or visible laser pulses, typically on the fs to picosecond (ps) timescale which can report on the incipient stage of photoinduced processes.

To exploit the full potential of ultrafast vibrational spectroscopy to characterize functional materials and biomolecules, we have developed femtosecond stimulated Raman spectroscopy (FSRS) as an emerging structural dynamics technique that has simultaneously high spectral and temporal resolutions.[7-13] The approach measures the ensemble average of

system response so the observed structural evolution is insensitive to stochastic fluctuations but useful to report on collective functional atomic motions that are previously challenging to measure experimentally.[2,7] The conventional FSRS technique (see Chapter 2) consists of an ~800 nm, ps Raman pump pulse from a grating-based spectral filter and a ca. 840—920 nm, fs Raman probe pulse from supercontinuum white light (SCWL) generation.[9-11] A preceding ~400 nm or 520—660 nm actinic pump pulse from second harmonic generation or noncollinear optical parametric amplification needs to be incorporated when the excited state molecular transformation is studied. One limiting factor for wider applications of FSRS is the wavelength tunability of incident pulses, particularly concerning the ps pump-fs probe pair that performs the stimulated Raman scattering process either in the electronic ground state (S_0) or excited state (e.g., S_1). Notably, different molecules have different potential energy landscapes so the vibrational energy levels and resonance Raman conditions vary greatly from sample to sample.[14] To turn FSRS into a more powerful and versatile spectroscopic toolset readily accessible to tackle a wide range of problems in energy and biology related fields, more technical innovations and optical advances are warranted.

In our earlier work, we reported the implementation of cascaded four-wave mixing (CFWM) in a thin transparent medium such as BK7 glass to generate broadband up-converted multicolor array (BUMA) signals.[15] One of these tunable, ultrabroad laser sidebands was used as the Raman probe in conjunction with an 800 nm Raman pump to

collect the anti-Stokes Raman spectrum of a 1:1 v/v carbon tetrachloride:ethanol mixed standard solution[16] (Chapter 3) with high signal-to-noise ratio. We have also reported the BUMA sidebands in a 0.1-mm-thick BBO crystal at phase-matching condition for maximal second harmonic generation (SHG).[17] The resultant SHG/sum-frequency-generation(SFG) assisted cascaded four-wave mixing processes lead to fs sideband signals from ca. 350—490 nm that are simultaneously enhanced due to $\chi^{(2)}$ and $\chi^{(3)}$-based four-wave optical parametric amplification (Chapter).[18] Can this expanded versatility and tunability help expand the available optical methods for fs Raman probe generation? Can we investigate sample systems that primarily absorb in the UV, such as DNA/RNA molecules, metal-organic complexes that undergo ligand-metal charge transfer upon photoexcitation, and the functionally relevant amino acids (e.g., Trp and Tyr) in proteins and enzymes? Notably, the near-UV probe pulse can work well in conjunction with a ps Raman pump pulse, which is available from a second harmonic bandwidth compressor (SHBC) using the commercially available femtosecond 800 nm laser source.[19] In addition, the UV photoexcitation pulse at 267 nm can be readily generated from third harmonic generation of the 800 nm fundamental pulse with a BBO crystal.

In this Chapter, we build on our previous results and report the construction and characterization of a versatile UV-FSRS setup incorporating both home-built second harmonic bandwidth compressor and SFG-based cascaded four-wave mixing. We demonstrate the feasibility of this setup in capturing the ground-state FSRS spectra of a

laser dye Quinolon 390 (7-Dimethylamino-1-methyl-4-methoxy-8-azaquinolone-2, $C_{12}H_{15}N_3O_2$; Exciton Catalog No. 03900, or LD390) that has an absorption/emission peak at 355/390 nm in methanol. By tuning the ps Raman pump wavelength from visible (e.g., 550, 487 nm) to UV (e.g., 402 nm) and fs Raman probe wavelength in tandem based on supercontinuum white light (SCWL) generation as well as the broadband up-converted multicolor array technology, we achieve the pre-resonance enhancement factor of >21 for the stimulated Raman modes over a wide spectral window of >1400 cm^{-1}. These new results showcase the utility of tunable BUMA laser pulses in advancing the emerging FSRS technique, broadening its application potential to expose equilibrium and transient vibrational signatures of a wider array of photosensitive molecular systems that absorb in the UV to near-IR range.[10,12]

6.3 Experimental section

Our main optical setup to achieve tunable FSRS in the UV range uses a portion of the fundamental pulse (FP) output from a Ti:sapphire-based fs laser regenerative amplifier (Legend Elite-USP-1K-HE, Coherent, Inc.) seeded by a mode-locked Ti:sapphire oscillator (Mantis-5, Coherent). The FP of ~1 W at 800 nm center wavelength with 35 fs time duration (full-width-half-maximum, or fwhm) and 1 kHz repetition rate is split into two parts with a 9:1 ratio to pump the home-built second harmonic bandwidth compressor and the broadband up-converted multicolor array setup, respectively (see Figure 6.1). In the second harmonic

bandwidth compressor section, the input beam is separated evenly into two arms, which go through reflective grating and cylindrical lens pairs and are stretched from fs to ps pulses with opposite chirps tuned to have the same magnitude (Chapter 4).[20] After recombining the two arms at a 1-mm-thick Type-I BBO crystal (θ = 29.2°) we achieve the chirp-free narrowband ps pulse centered at ~402 nm as a result of the chirp elimination effect [21]. The time duration of the second harmonic pulse is characterized by the optical Kerr effect (OKE) measurement with another 400 nm pulse from second harmonic generation of the FP followed by prism compression (40 fs, acting as the gate pulse), yielding a temporal profile with ~1.45 ps fwhm (Figure 6.2). To obtain the spectral width, we disperse the pulse with a 1200 grooves/mm, 500 nm blaze ruled reflective grating and image onto a CCD camera. After wavelength calibration with a mercury argon source (HG-1, Ocean Optics) across the UV/Vis range, the fwhm of the picosecond 402 nm pulse is measured to be ~11 cm^{-1}. This represents a time-bandwidth product of ~15.9 $ps \cdot cm^{-1}$ that is close to the Fourier-transform limit of a Gaussian-profile pulse (~14.7 $ps \cdot cm^{-1}$), indicating that the 402 nm pulse is largely chirp-free and can be used as the narrowband Raman pump pulse in FSRS.

In the broadband up-converted multicolor array setup, an FP and an SCWL (alternatively referred to as WL) pulse are loosely focused onto a 0.1-mm-thick BBO crystal to generate multiple sidebands via SFG-based cascaded four-wave mixing.[17] The crossing angle between the two incident fs pulses is ~6° to achieve balance between conversion efficiency and spatial separation of nascent sidebands.[15,22,23] The phase-matching condition of the

BBO crystal is set to favor SFG. The first sideband on either the FP (S_{+1}) or WL (S_{-1}) side is selected with an iris diaphragm and used as the Raman probe (Figure 6.1). The pulse-to-pulse intensity stability is within 5%, which can be effectively averaged out by repeatedly collecting FSRS signals over several minutes (see below). Notably, the highly nonlinear pulse generation does not incur substantial intensity noise because we use low pump power to generate laser sidebands in the background-free directions (see Figure 6.1) so the interference effect with fundamental incident pulses is much reduced. Furthermore, the bandwidth of S_{+1} and S_{-1} is measured to be ca. 1400 and 1700 cm^{-1}, respectively, which supports the self-compression of these CFWM-induced sidebands to fs pulses.[15,17] To potentially achieve transform-limited pulses, further compression with accurate chirp compensation is needed.[24,25]

The selected BUMA sideband and the SHBC output pulse are focused onto a 1-mm-thick quartz sample cell by an f = 12 cm off-axis parabolic mirror to avoid introducing additional chirps (e.g., if we use a focusing lens instead). Both incident beams pass through the sample solution containing 15 mM LD390 laser dye in methanol (Figure 6.1). The Raman pump is then blocked while the Raman probe pulse carrying the stimulated Raman scattering signal is re-collimated and focused into the spectrograph with a 1200 grooves/mm, 500 nm blaze ruled reflective grating. The dispersed signal is collected by a CCD array camera (Princeton Instruments, PIXIS 100F) that is synchronized with the laser at 1 kHz repetition rate to achieve shot-to-shot spectral acquisition. A phase-stable optical chopper (Newport 3501) in

the Raman pump beampath at 500 Hz (also synchronized with the laser) ensures that one Raman spectrum can be collected within 2 ms through dividing the Raman probe profile with "Raman pump on" by "Raman pump off" (see Equation 6.1).

Therefore, the recorded FSRS signal strength is typically expressed in the stimulated Raman gain:

$$\text{Raman Gain} = \text{Probe\_spectrum}_{\text{pump-on}} / \text{Probe\_spectrum}_{\text{pump-off}} - 1 \qquad (6.1)$$

We routinely collect the Raman spectrum with 3,000 laser shots per point and 100 sets, so 150,000 Raman spectra are averaged to yield the final Raman spectrum as shown in Figure 6.3a and Figure 6.4a with much improved signal-to-noise ratio. Experimentally we do not observe sharp noises that affect the detection sensitivity of the system, and the highly efficient data averaging within ~3 seconds for each recorded data trace largely removes the broad baseline fluctuations of the probe pulse (e.g., mostly up and down in intensity profile, not left and right along the frequency axis). All the experiments are performed at room temperature (21.9 °C) and ambient pressure (1 atm). To investigate the resonance Raman enhancement effect, we use the previously developed tunable FSRS in the visible to generate the ps Raman pump pulse (at 487 and 550 nm) in conjunction with an fs Raman probe pulse (to the red side of the pump) based on supercontinuum white light generation in a 2-mm-thick *Z*-cut sapphire plate followed by prism compression. Figure 6.3a displays

the detailed comparison between ground-state FSRS spectra collected at various Raman pump-probe wavelengths, wherein the intensity noise level does not increase significantly as Raman pump wavelength approaches the electronic absorption peak. Figure 6.3b shows the computed Raman modes from density functional theory (DFT) B3LYP calculations in the electronic ground state using 6-311G+(d, p) basis sets for LD390 in methanol solution and the integral equation formalism polarizable continuum model (IEFPCM – methanol), performed by the Gaussian 09 software program.[26]

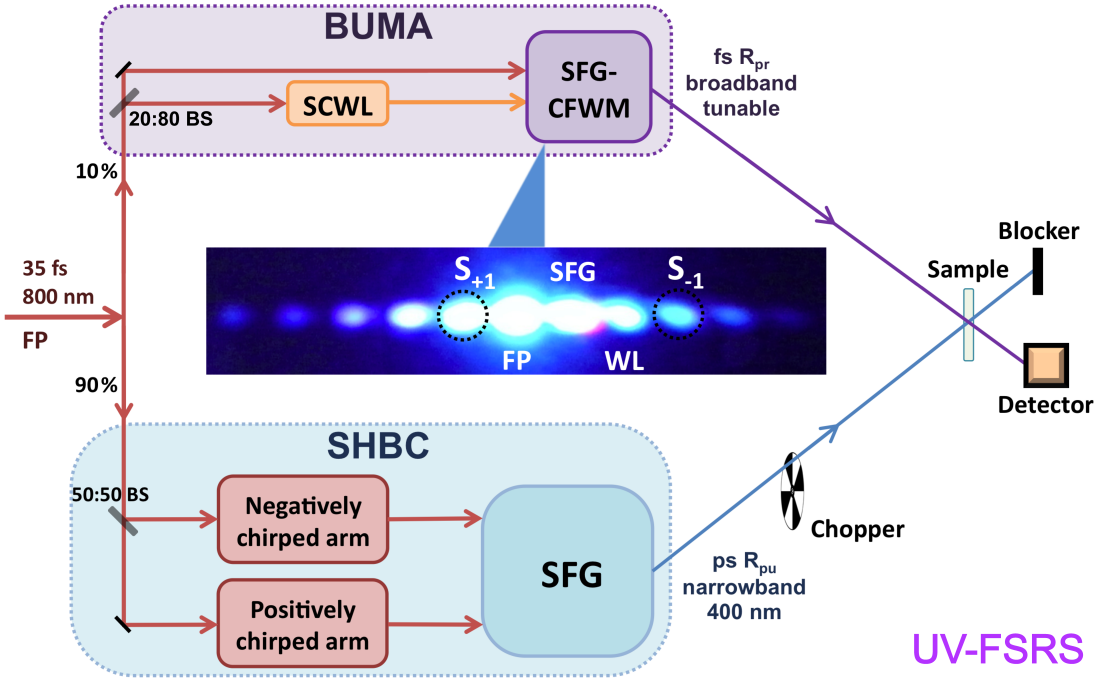

Figure 6.1 Schematic of the UV-FSRS experimental setup. The fundamental laser output is split to separately pump a home-built second harmonic bandwidth compressor (SHBC, light blue shaded area) and a broadband up-converted multicolor array (BUMA, light violet shaded area) based on the unique SFG-based cascaded four-wave mixing (CFWM) in a thin BBO crystal. A photograph of SFG-CFWM sideband signals on a sheet of white paper is shown with the first sideband on either side of SFG highlighted by black dotted circles. The first sideband either on the FP side (S_{+1}) or on the WL side (S_{-1}) is used as the Raman probe pulse in conjunction with the narrowband SHBC output as the Raman pump to record anti-Stokes and Stokes stimulated Raman spectrum, respectively. The 20:80 BS represents 20% Reflection and 80% Transmission.

6.4 Results and discussion

The FSRS technology has been successfully applied to a number of important photosensitive molecular systems including rhodopsin,[27] bacteriorhodopsin,[28] phytochrome,[29] organic dyes in solar cells,[30] Fe(II) spin crossover in solution,[31] fluorescent proteins,[7,32,33] and calcium-ion-sensing protein biosensors.[34-36] The main goal of this work is to construct a versatile, tunable FSRS setup that extends the wavelength detection window to the UV regime with desired resonance Raman enhancement. As a result, a wider range of photochemical reaction pathways can be elucidated particularly for metal-organic complexes in solution (absorption peak below 300 nm) and tyrosine residues in proteins (max absorption at ~276 nm) in conjunction with a femtosecond actinic pump pulse. Because FSRS is a stimulated Raman technique, the concomitant generation of a pair of ps-Raman-pump and fs-Raman-probe pulses is required.

6.4.1 **UV-FSRS Setup with SHBC and SFG-CFWM**

Starting from the fs 800 nm laser amplifier system, we choose to exploit a home-built single-grating-based second harmonic bandwidth compressor to produce a ~400 nm, ps pulse[20] as the Raman pump. To conveniently generate an accompanying Raman probe, we rely on the SFG-CFWM method that can be readily tuned by varying the time delay between the two incident pulses or selecting a different sideband on either side of the FP beam (see Figure

6.1, middle). The wavelength tunability of those sidebands has been discussed in our previous reports.[15,17] Figure 6.2a shows temporal characterization of the second harmonic bandwidth compressor output at 402 nm with ~1.45 ps pulse duration (fwhm). Figure 6.2b displays the relative spectral position of the narrowband Raman pump and two distinct femtosecond BUMA sidebands from SFG-CFWM processes in a thin BBO crystal, S_{+1} and S_{-1}, which enable the collection of anti-Stokes and Stokes Raman spectrum, respectively. Furthermore, we have demonstrated the SFG-CFWM sidebands spanning a broad UV to visible spectral range from ca. 350—490 nm,[17] which can be potentially pushed toward shorter wavelengths upon increasing the pump power and/or reducing the incident beam crossing angle.[23,24]

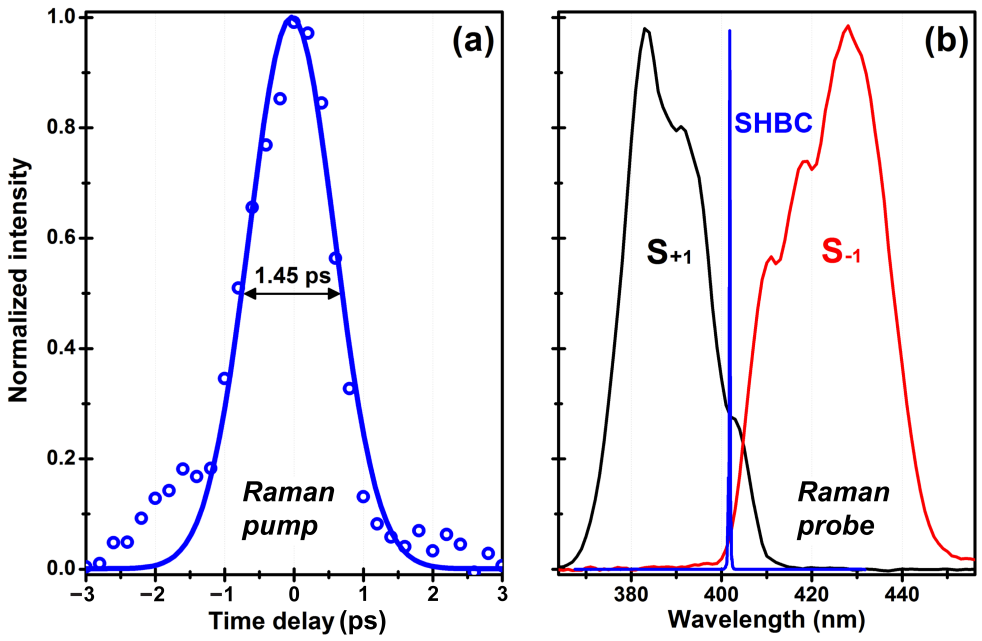

Figure 6.2 Spectral characterization of the Raman pump and probe pulse pair for FSRS. (a) Temporal profile of the narrowband Raman pump measured from OKE. The pulse duration of ~1.45 ps is obtained from the fwhm of the Gaussian fit (blue solid curve) to the time-resolved experimental data points (blue open circles). (b) Spectra of the SHBC output as the Raman pump in (a) (blue) and the first two BUMA sidebands as the Raman probe, S_{+1} on the FP side (black) and S_{-1} on the WL side (red), respectively.

6.4.2 **Ground-State FSRS of Laser Dye LD390**

To demonstrate the feasibility of the aforementioned UV-FSRS setup, we select LD390 as the molecular sample system because this laser dye in methanol strongly absorbs 355 nm light, while the solvent only has two major Raman peaks at ~1033 and 1460 cm^{-1}. To our best knowledge, the standard or spontaneous Raman spectrum of LD390 has not been reported, so the measurement here represents a new spectroscopic characterization of this commercial laser dye molecule and its vibrational motions in solution. After equal amount of solution and solvent data collection, average and subtraction which remove most of the systematic noise and laser fluctuation effect, the pure ground-state Raman spectrum of LD390 is shown in Figure 6.3a that has a number of prominent peaks between ca. 300—1700 cm^{-1}. These are Stokes Raman spectra because the probe pulse is S_{-1} on the WL side (Figure 6.1) and to the red of the pump pulse (Figure 6.2b).

Based on the UV/Vis spectrum of LD390 in Figure 6.3a inset, the 402 nm Raman pump represents the closest frequency position to the electronic absorption peak (i.e., 355 nm) among the three Raman pump wavelengths being used, and the pre-resonance enhancement factor reaches >21 at the 1317/1348 cm^{-1} peak doublet while all the other experimental conditions are unchanged. The observed peak intensity decreases if the Raman pump wavelength is tuned away from the electronic absorption peak position, but the ultrafast Raman approach is still beneficial for collecting vibrational signatures due to the high incident laser peak density (vs. continuous-wave source for example). Notably, minimal

interference below 400 cm^{-1} makes it feasible to study lower frequency regime of the Raman spectrum. This likely arises from good solubility of the dye molecule in methanol and less Raman pump scattering into the Raman probe beampath (i.e., FSRS signal direction).[11,13]

Since the standard Raman spectrum of LD390 is not readily available from literature and it is useful to correlate observed peaks to characteristic nuclear motions, we perform electronic ground-state DFT calculations in *Gaussian* program[26] to facilitate vibrational normal mode assignment. The overall match between the experimental and calculated spectrum is very good with a frequency scaling factor of 0.99.[37] The major vibrational modes are listed in

Table 6.1.

Notably, the correspondence between the calculated Raman spectrum and the measured one

S_0 calc.[a] (cm^{-1})	S_0 FSRS[b] (cm^{-1})	Vibrational mode assignment[c]
665	663	Ring in-plane asymmetric deformation
711	714	Ring asymmetric breathing with N1–CH_3 stretching
1068	1069	A-ring deformation and H rocking, B-ring small-scale breathing, and N13–$(CH_3)_2$ H twisting
1312	1317	N1–C2 stretching with ring asymmetric deformation and ring-H rocking, and (N1)–CH_3 methyl group bending
1357	1348	C7–N8 stretching and A-ring H rocking, A-ring in-plane deformation with some C9–C10 stretching
1393	1390	N1–CH_3 stretching and methyl group symmetric bending, A-ring in-plane deformation, and ring-H rocking
1613	1615	Ring C=C and C=N stretching, ring-H rocking with C2=O11 stretching

is not exact (Figure 6.3). This is understandable because the Gaussian DFT calculation concerns an "unrestricted" single molecule in a polarizable continuum to model solvation

effects (i.e., we used IEFPCM – methanol, see above). In the real spectroscopic measurement, the ensemble average of solvated dye molecules LD390 in methanol solution is measured and the Raman mode polarizability is intimately determined by the extensive hydrogen (H)-bonding network around the chromophore. For example, the calculated strong modes between ca. 1450—1600 cm^{-1} (see Figure 6.3b) become much weaker in the ground-state FSRS spectrum (Figure 6.3a), suggesting that the corresponding mode polarizability decreases significantly and/or mode frequency shifts as a result of H-bonding matrix particularly in the chromophore local environment. It is also notable that the two strongest peaks observed at ~1317, 1348 cm^{-1} both consist of C–N stretching and ring-H rocking motions plus ring in-plane deformations on both aromatic rings of the dye molecule. The large change in conjugation and electronic polarizability over the two-ring system leads to the observed strong Raman gain in comparison to other vibrational modes. Moreover, the amplification of the Stokes Raman spectrum primarily applies to the solute signal but not to spectral noise, so the experimental signal-to-noise ratio is greatly enhanced with the ~400 nm Raman pump and should be beneficial to characterize functional materials and molecular systems with intrinsically small electric polarizabilities.[20,38]

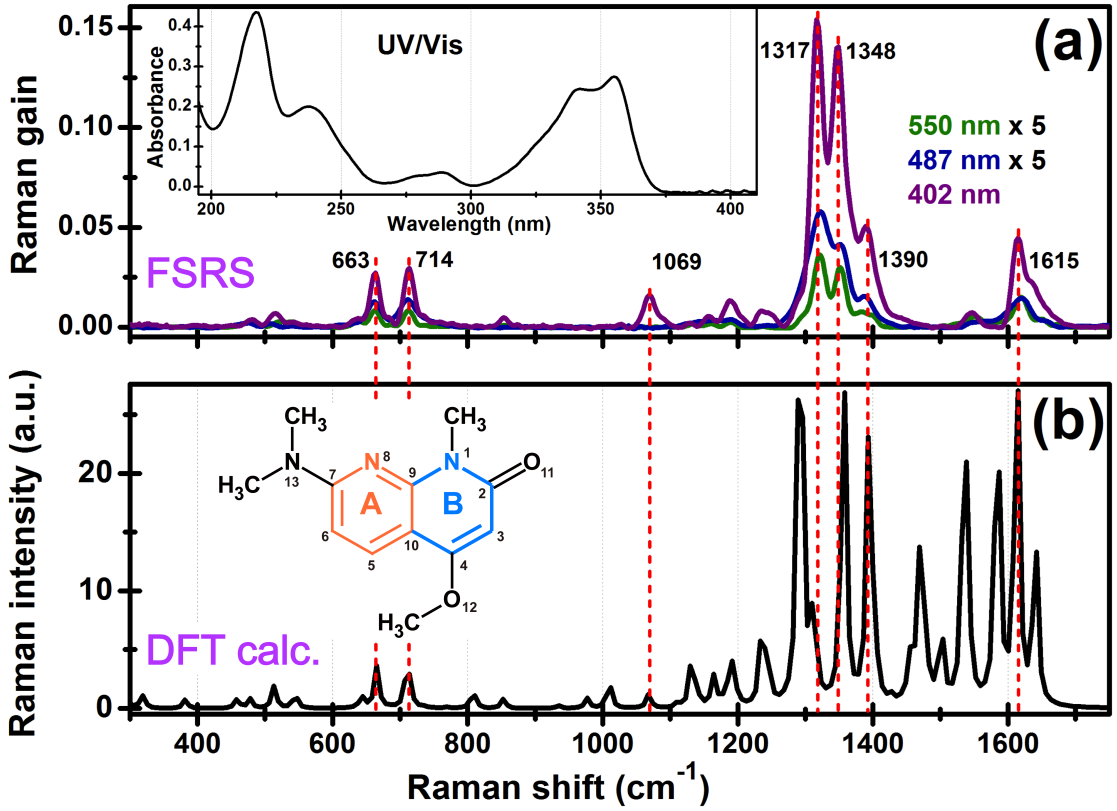

Figure 6.3 Ground-state Stokes FSRS of LD390 in methanol. (a) Experimental stimulated Raman spectra in S_0 with the Raman pump at 550 nm (green), 487 nm (blue), and 402 nm (violet) and Raman probe to its red side, respectively. The former two spectral traces are enlarged by 5 times for direct comparison with the spectrum collected with 402 nm pump. Prominent vibrational peaks are marked with frequencies labeled in black. The UV/Vis electronic absorption spectrum is shown in the inset. (b) DFT-based *Gaussian* calculated spectrum of LD390 in methanol with a uniform peak width of 8 cm^{-1} (i.e., default fwhm in the program). The molecular structure of the dye is depicted in the inset with two aromatic rings labeled in A (orange) and B (cyan). The key atomic sites are numbered from 1–13.

Table 6.1 Ground-state FSRS vibrational peak frequencies and mode assignments aided by calculations

S_0 calc.[a] (cm^{-1})	S_0 FSRS[b] (cm^{-1})	Vibrational mode assignment[c]
665	663	Ring in-plane asymmetric deformation
711	714	Ring asymmetric breathing with N1–CH_3 stretching
1068	1069	A-ring deformation and H rocking, B-ring small-scale breathing, and N13–$(CH_3)_2$ H twisting
1312	1317	N1–C2 stretching with ring asymmetric deformation and ring-H rocking, and (N1)–CH_3 methyl group bending
1357	1348	C7–N8 stretching and A-ring H rocking, A-ring in-plane deformation with some C9–C10 stretching
1393	1390	N1–CH_3 stretching and methyl group symmetric bending, A-ring in-plane deformation, and ring-H rocking
1613	1615	Ring C=C and C=N stretching, ring-H rocking with C2=O11 stretching

[a] Vibrational normal mode frequencies are obtained from DFT B3LYP calculations in S_0 using 6-311G+(d, p) basis sets for LD390 in methanol with Gaussian 09 program.[26] The scaling factor of 0.99 is used to compare the calculated frequency with experimental result.

[b] The experimentally observed frequencies of the ground-state Raman peaks of 15 mM LD390 in pure methanol using tunable FSRS technology in the UV to visible range.

[c] Vibrational motions are assigned based on DFT calculation results. Only major vibrational modes are listed with the atomic numbering defined in Figure 6.3b inset.

6.4.3 **Comparison between the Stokes and Anti-Stokes FSRS**

It is notable that both the Stokes and anti-Stokes Raman spectra can be conveniently captured by FSRS gain/loss measurement depending upon the relative wavelengths of the Raman pump and probe pulses, while the latter can be switched between various BUMA sidebands (e.g., shifting the pinhole position) or tuned within the same sideband (e.g., varying the time delay between FP and WL) with ease (see Figure 6.1). Based on partition functions in thermodynamics, there is less population on the first excited vibrational state (i.e., quantum number v=1) than that on the ground state (v=0). At room temperature the thermal energy 1 k_BT amounts to ~200 cm^{-1} so all the vibrational modes (e.g., >300 cm^{-1} in Figure 6.3a) should display weaker anti-Stokes spontaneous Raman peaks than the corresponding Stokes peaks particularly for high-frequency modes. In contrast, FSRS signal strength is normalized by the probe intensity (see Equation 6.1) but is typically proportional to Raman pump power[9,39] and to the square of the SRS nonlinear coefficient for either the Stokes or anti-Stokes signal.[40,41] Figure 6.4a shows that the ground-state FSRS anti-Stokes Raman spectrum we collected using S_{+1} on the FP side as the probe (i.e., to the blue of the 402 nm pump pulse in Figure 6.2b) is much stronger than the Stokes spectrum. This unusual, opposite trend indicates that some other factors contribute to the Raman signal strength beyond the Raman pump power and third-order nonlinear polarizabilities.[41] Recent experimental work in our lab has shed more light on the anti-Stokes FSRS technique and applications in tracking vibrational cooling with photochemical reactions (e.g., in S_1).[42,43]

Can the observed intensity difference arise from resonance enhancement because this is a stimulated Raman technique?[14,44] If so, how does the Raman pump wavelength compare to the 0–0 vertical transition energy between the electronic ground state and excited state of LD390 in both FSRS measurements?

We list all the anti-Stokes over Stokes peak intensity ratios in Figure 6.4a inset and it becomes apparent that the two modes below 750 cm^{-1} have a modest ratio below 1.8 while the modes above 1000 cm^{-1} all have a larger ratio above 3.0. The overall trend is that the Raman peak gets stronger as the vibrational frequency increases. Given that the anti-Stokes process originates from the higher-lying vibrational state (e.g., v=1) and terminates at the lower-lying vibrational state (e.g., v=0), this experimental trend can be explained by the principle of resonance Raman enhancement because the 402 nm pump pulse being used still falls short of the LD390 electronic absorption peak of ~355 nm (Figure 6.4b). As a result, for the anti-Stokes transition, the 663 (1615) cm^{-1} modes correspond to an "effective" Raman pump wavelength of 392 (377) nm, making the latter Raman mode much stronger because a 377 nm pump is in closer proximity to the 355 nm electronic gap than a 392 nm pump. This reasoning is further corroborated by experimental data in Figure 6.3a, and paves the way to enhance higher-frequency Raman modes regardless of their intrinsic electronic polarizability. For the Stokes spectrum that starts from the ground state and ends on the v=1 state in S_0, the vibrational transition frequency does not affect the energy relation between the 402 nm Raman pump and the 355 nm electronic energy gap (i.e., no addition of the

vibrational frequency can occur to bring the 402 nm Raman pump closer to the solute S_1 state, see Figure 6.4b), hence the intensity ratio between Raman peaks is mostly determined by the mode-dependent polarizability.[13,45] We note that this interpretation is based on the first "excitatory" interaction of the system with Raman pump; interestingly, the principle holds true for a first interaction with the Raman probe case as well because the Raman pump still needs to interact with the system as part of the four-wave-mixing process (e.g., inverse Raman process as one of the anti-Stokes FSRS signal generation pathways). In other words, the "de-excitatory" Raman pump induces a downward transition in the anti-Stokes FSRS process to generate the vibrational coherence that undergoes free induction decay (FID). Due to the energy difference between the Raman pump and the electronic transition gap, higher frequency vibrational modes still achieve a better resonance enhancement compared to those lower frequency modes as shown in Figure 6.4a.

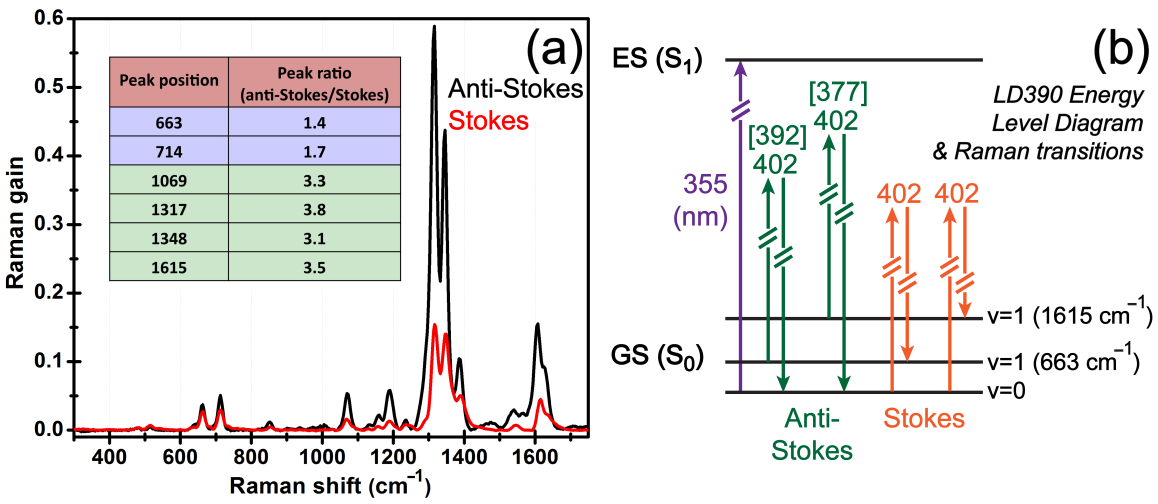

Figure 6.4 (a) Comparison between the Stokes (red) and anti-Stokes (black) ground-state FSRS data for LD390 in methanol solution. The first-order UV-BUMA sideband S_{+1}/S_{-1} on the FP/WL side acts as the Raman probe for anti-Stokes/Stokes FSRS with the 402 nm Raman pump pulse, respectively. The frequency axes are calibrated and for direct spectral comparison, the anti-Stokes Raman shift axis as well as the Raman peak intensities are multiplied by –1. The inset tabulates the observed peak intensity ratios of several major vibrational modes between 600—1700 cm^{-1}. (b) The spectroscopic origin of the observed Raman intensity ratios can be understood by a representative molecular energy level diagram of LD390. Two characteristic vibrational modes are shown (vibrational quantum number v=1) with the relative energy differences between various Raman transition configurations depicted by colored vertical arrowed lines. The numbers in brackets represent effective Raman pump wavelengths in nm unit with possible light-matter interaction pathways enabled by the nonlinear spectroscopic approach (see text for details).

6.5 Conclusions

In summary, we have developed a unique UV-FSRS setup with a home-built second harmonic bandwidth compressor output (~400 nm center wavelength, 1.5 ps fwhm) as the Raman pump and various broadband up-converted multicolor array (BUMA) sideband laser pulses (ca. 360—460 nm, fs) as the Raman probe to obtain the stimulated Raman spectrum. The BUMA signals in this work arise from SFG/SHG-based cascaded four-wave mixing processes in a thin BBO crystal. Two other Raman pump wavelengths are achieved using a tunable FSRS setup in the visible range and the resultant Stokes spectrum of 15 mM LD390 in methanol is >21 times weaker due to larger mismatch between the Raman pump wavelength and the electronic absorption peak frequency of the laser dye. This manifests the advantage of using tunable ps pulses to study molecules with different absorption profiles over a wide spectral range. The Raman spectrum of LD390 is collected over a ~1400 cm^{-1} detection window for the first time with vibrational mode assignments aided by *Gaussian* DFT calculations. Using a ~400 nm ps Raman pump, the anti-Stokes Raman spectrum turns out to be much stronger than the Stokes spectrum mainly due to pre-resonance enhancement involving the vibrational energy gap in S_0, which is confirmed by the relative intensity ratio change between the low- and high-frequency vibrational modes. The Raman pump and probe wavelengths are important factors to improve the SNR.

The versatile and compact approach of generating tunable probe pulses in the UV should make the FSRS technology more accessible to many laboratories for elucidation of

molecular conformational dynamics in the electronic ground state, as well as excited state upon incorporation of a preceding fs photoexcitation pulse (see Chapter 8).[10,11,13] This methodology also paves the way to harness the broadband tunability of multicolor laser sidebands to study molecules that primarily absorb in the UV which include metal-organic complexes such as triphenylbismuth in methanol solution (see Chapter 7) and biomolecules such as DNA and tyrosine derivatives in water.

6.6 References

[1] A. H. Zewail, *Femtochemistry: Ultrafast Dynamics of the Chemical Bond*. (World Scientific, Singapore, 1994).

[2] R. M. Hochstrasser, "Two-Dimensional Spectroscopy at Infrared and Optical Frequencies", *Proc. Natl. Acad. Sci. U.S.A.* **104** (36), 14190-14196 (2007).

[3] J. Zheng, K. Kwak, J. Asbury, X. Chen, I. R. Piletic, and M. D. Fayer, "Ultrafast Dynamics of Solute-Solvent Complexation Observed at Thermal Equilibrium in Real Time", *Science* **309** (5739), 1338-1343 (2005).

[4] C. Fang, A. Senes, L. Cristian, W. F. DeGrado, and R. M. Hochstrasser, "Amide Vibrations Are Delocalized Across the Hydrophobic Interface of a Transmembrane Helix Dimer", *Proc. Natl. Acad. Sci. U.S.A.* **103** (45), 16740-16745 (2006).

[5] G. S. Engel, T. R. Calhoun, E. L. Read, T.-K. Ahn, T. Mancal, Y.-C. Cheng, R. E. Blankenship, and G. R. Fleming, "Evidence for Wavelike Energy Transfer Through Quantum Coherence in Photosynthetic Systems", *Nature* **446**, 782-786 (2007).

[6] C. Fang, J. D. Bauman, K. Das, A. Remorino, E. Arnold, and R. M. Hochstrasser, "Two-Dimensional Infrared Spectra Reveal Relaxation of the Nonnucleoside Inhibitor TMC278 Complexed with the HIV-1 Reverse Transcriptase", *Proc. Natl. Acad. Sci. U.S.A.* **105** (5), 1472-1477 (2008).

[7] C. Fang, R. R. Frontiera, R. Tran, and R. A. Mathies, "Mapping GFP Structure Evolution during Proton Transfer with Femtosecond Raman Spectroscopy", *Nature* **462** (7270), 200-204 (2009).

[8] M. Yoshizawa and M. Kurosawa, "Femtosecond Time-Resolved Raman Spectroscopy Using Stimulated Raman Scattering", *Phys. Rev. A* **61** (1), 013808 (1999).

[9] D. W. McCamant, P. Kukura, S. Yoon, and R. A. Mathies, "Femtosecond Broadband Stimulated Raman Spectroscopy: Apparatus and Methods", *Rev. Sci. Instrum.* **75** (11), 4971-4980 (2004).

[10] R. R. Frontiera, C. Fang, J. Dasgupta, and R. A. Mathies, "Probing Structural Evolution along Multidimensional Reaction Coordinates with Femtosecond Stimulated Raman Spectroscopy", *Phys. Chem. Chem. Phys.* **14** (2), 405-414 (2012).

[11] W. Liu, F. Han, C. Smith, and C. Fang, "Ultrafast Conformational Dynamics of Pyranine during Excited State Proton Transfer in Aqueous Solution Revealed by Femtosecond Stimulated Raman Spectroscopy", *J. Phys. Chem. B* **116** (35), 10535-10550 (2012).

[12] J. Dasgupta, R. R. Frontiera, C. Fang, and R. A. Mathies, in *Encyclopedia of Biophysics*, edited by Gordon C. K. Roberts (Springer Berlin Heidelberg, 2013), pp. 745-759.

[13] F. Han, W. Liu, and C. Fang, "Excited-State Proton Transfer of Photoexcited Pyranine in Water Observed by Femtosecond Stimulated Raman Spectroscopy",

Chem. Phys. **422** (0), 204-219 (2013).

14 A. B. Myers and R. A. Mathies, in *Biological Applications of Raman Spectroscopy*, edited by T. G. Spiro (John Wiley & Sons, Inc., New York, 1987), Vol. 2, pp. 1-58.

15 W. Liu, L. Zhu, L. Wang, and C. Fang, "Cascaded Four-Wave Mixing for Broadband Tunable Laser Sideband Generation", *Opt. Lett.* **38** (11), 1772-1774 (2013).

16 L. Zhu, W. Liu, and C. Fang, "Tunable Sideband Laser from Cascaded Four-Wave Mixing in Thin glass for Ultra-Broadband Femtosecond Stimulated Raman Spectroscopy", *Appl. Phys. Lett.* **103** (6), 061110 (2013).

17 W. Liu, L. Zhu, and C. Fang, "Observation of Sum-Frequency-Generation-Induced Cascaded Four-Wave Mixing Using Two Crossing Femtosecond Laser Pulses in a 0.1 mm Beta-Barium-Borate Crystal", *Opt. Lett.* **37** (18), 3783-3785 (2012).

18 L. Zhu, W. Liu, L. Wang, and C. Fang, "Parametric Amplification-Assisted Cascaded Four-Wave Mixing for Ultrabroad Laser Sideband Generation in a Thin Transparent Medium", *Laser Phys. Lett.* **11** (7), 075301 (2014).

19 S. Laimgruber, H. Schachenmayr, B. Schmidt, W. Zinth, and P. Gilch, "A Femtosecond Stimulated Raman Spectrograph for the Near Ultraviolet", *Appl. Phys. B* **85** (4), 557-564 (2006).

20 L. Zhu, W. Liu, and C. Fang, "A Versatile Femtosecond Stimulated Raman Spectroscopy Setup with Tunable Pulses in the Visible to Near Infrared", *Appl. Phys. Lett.* **105** (4), 041106 (2014).

21 F. Raoult, A. C. L. Boscheron, D. Husson, C. Sauteret, A. Modena, V. Malka, F. Dorchies, and A. Migus, "Efficient Generation of Narrow-Bandwidth Picosecond Pulses by Frequency Doubling of Femtosecond Chirped Pulses", *Opt. Lett.* **23** (14), 1117-1119 (1998).

22 H. Crespo, J. T. Mendonca, and A. Dos Santos, "Cascaded Highly Nondegenerate Four-Wave-Mixing Phenomenon in Transparent Isotropic Condensed Media", *Opt. Lett.* **25** (11), 829-831 (2000).

23 J. Liu and T. Kobayashi, "Cascaded Four-Wave Mixing and Multicolored Arrays Generation in a Sapphire Plate by Using Two Crossing Beams of Femtosecond Laser", *Opt. Express* **16** (26), 22119-22125 (2008).

24 R. Weigand, J. T. Mendonca, and H. M. Crespo, "Cascaded Nondegenerate Four-Wave-Mixing Technique for High-Power Single-Cycle Pulse Synthesis in the Visible and Ultraviolet Ranges", *Phys. Rev. A* **79** (6), 063838 (2009).

25 O. Shitamichi, Y. Kida, and T. Imasaka, "Chirped-Pulse Four-Wave Raman Mixing in Molecular Hydrogen", *Appl. Phys. B* **117** (2), 723-730 (2014).

26 M. J. Frisch, G. W. Trucks, H. B. Schlegel, G. E. Scuseria, M. A. Robb, J. R. Cheeseman, G. Scalmani, V. Barone, B. Mennucci, G. A. Petersson, H. Nakatsuji, M. Caricato, X. Li, H. P. Hratchian, A. F. Izmaylov, J. Bloino, G. Zheng, J. L. Sonnenberg, M. Hada, M. Ehara, K. Toyota, R. Fukuda, J. Hasegawa, M. Ishida, T. Nakajima, Y. Honda, O. Kitao, H. Nakai, T. Vreven, J. J. A. Montgomery, J. E. Peralta, F. Ogliaro, M. Bearpark, J. J. Heyd, E. Brothers, K. N. Kudin, V. N.

Staroverov, R. Kobayashi, J. Normand, K. Raghavachari, A. Rendell, J. C. Burant, S. S. Iyengar, J. Tomasi, M. Cossi, N. Rega, J. M. Millam, M. Klene, J. E. Knox, J. B. Cross, V. Bakken, C. Adamo, J. Jaramillo, R. Gomperts, R. E. Stratmann, O. Yazyev, A. J. Austin, R. Cammi, C. Pomelli, J. W. Ochterski, R. L. Martin, K. Morokuma, V. G. Zakrzewski, G. A. Voth, P. Salvador, J. J. Dannenberg, S. Dapprich, A. D. Daniels, Ö. Farkas, J. B. Foresman, J. V. Ortiz, J. Cioslowski, and D. J. Fox, *Gaussian 09, Revision B.1* (Gaussian, Inc., Wallingford, CT, 2009).

[27] P. Kukura, D. W. McCamant, S. Yoon, D. B. Wandschneider, and R. A. Mathies, "Structural Observation of the Primary Isomerization in Vision with Femtosecond-Stimulated Raman", *Science* **310**, 1006-1009 (2005).

[28] S. Shim, J. Dasgupta, and R. A. Mathies, "Femtosecond Time-Resolved Stimulated Raman Reveals the Birth of Bacteriorhodopsin's J and K Intermediates", *J. Am. Chem. Soc.* **131**, 7592-7597 (2009).

[29] J. Dasgupta, R. R. Frontiera, K. C. Taylor, J. C. Lagarias, and R. A. Mathies, "Ultrafast Excited-State Isomerization in Phytochrome Revealed by Femtosecond Stimulated Raman Spectroscopy", *Proc. Natl. Acad. Sci. U.S.A.* **106** (6), 1784-1789 (2009).

[30] R. R. Frontiera, J. Dasgupta, and R. A. Mathies, "Probing Interfacial Electron Transfer in Coumarin 343 Sensitized TiO_2 Nanoparticles with Femtosecond Stimulated Raman", *J. Am. Chem. Soc.* **131** (43), 15630-15632 (2009).

[31] A. L. Smeigh, M. Creelman, R. A. Mathies, and J. K. McCusker, "Femtosecond Time-Resolved Optical and Raman Spectroscopy of Photoinduced Spin Crossover: Temporal Resolution of Low-to-High Spin Optical Switching", *J. Am. Chem. Soc.* **130** (43), 14105-14107 (2008).

[32] H. Kuramochi, S. Takeuchi, and T. Tahara, "Ultrafast Structural Evolution of Photoactive Yellow Protein Chromophore Revealed by Ultraviolet Resonance Femtosecond Stimulated Raman Spectroscopy", *J. Phys. Chem. Lett.* **3** (15), 2025-2029 (2012).

[33] M. Creelman, M. Kumauchi, W. D. Hoff, and R. A. Mathies, "Chromophore Dynamics in the PYP Photocycle from Femtosecond Stimulated Raman Spectroscopy", *J. Phys. Chem. B* **118** (3), 659-667 (2014).

[34] B. G. Oscar, W. Liu, Y. Zhao, L. Tang, Y. Wang, R. E. Campbell, and C. Fang, "Excited-State Structural Dynamics of a Dual-Emission Calmodulin-Green Fluorescent Protein Sensor for Calcium Ion Imaging", *Proc. Natl. Acad. Sci. U.S.A.* **111** (28), 10191-10196 (2014).

[35] L. Tang, W. Liu, Y. Wang, Y. Zhao, B. G. Oscar, R. E. Campbell, and C. Fang, "Unraveling Ultrafast Photoinduced Proton Transfer Dynamics in a Fluorescent Protein Biosensor for Ca^{2+} Imaging", *Chem. Eur. J.*, **21** (17), 6481-6490 (2015).

[36] Y. Wang, L. Tang, W. Liu, Y. Zhao, B. G. Oscar, R. E. Campbell, and C. Fang, "Excited State Structural Events of a Dual-Emission Fluorescent Protein Biosensor for Ca^{2+} Imaging Studied by Femtosecond Stimulated Raman Spectroscopy", *J.*

Phys. Chem. B **119** (6), 2204-2218 (2015).

[37] V. Tozzini and R. Nifosì, "Ab Initio Molecular Dynamics of the Green Fluorescent Protein (GFP) Chromophore: An Insight into the Photoinduced Dynamics of Green Fluorescent Proteins", *J. Phys. Chem. B* **105** (24), 5797-5803 (2001).

[38] W. Wang, W. Liu, I.-Y. Chang, L. A. Wills, L. N. Zakharov, S. W. Boettcher, P. H.-Y. Cheong, C. Fang, and D. A. Keszler, "Electrolytic Synthesis of Aqueous Aluminum Nanoclusters and *in situ* Characterization by Femtosecond Raman Spectroscopy & Computations", *Proc. Natl. Acad. Sci. U.S.A.* **110** (46), 18397-18401 (2013).

[39] R. R. Frontiera, S. Shim, and R. A. Mathies, "Origin of Negative and Dispersive Features in Anti-Stokes and Resonance Femtosecond Stimulated Raman Spectroscopy", *J. Chem. Phys.* **129** (6), 064507-064506 (2008).

[40] S. Y. Lee and E. J. Heller, "Time‐Dependent Theory of Raman Scattering", *J. Chem. Phys.* **71** (12), 4777-4788 (1979).

[41] S.-Y. Lee, D. Zhang, D. W. McCamant, P. Kukura, and R. A. Mathies, "Theory of Femtosecond Stimulated Raman Spectroscopy", *J. Chem. Phys.* **121** (8), 3632-3642 (2004).

[42] W. Liu, L. Tang, B. G. Oscar, Y. Wang, C. Chen, and C. Fang, "Tracking Ultrafast Vibrational Cooling during Excited-State Proton Transfer Reaction with Anti-Stokes and Stokes Femtosecond Stimulated Raman Spectroscopy", *J. Phys. Chem. Lett.* **8** (5), 997-1003 (2017).

[43] B. G. Oscar, C. Chen, W. Liu, L. Zhu, and C. Fang, "Dynamic Raman Line Shapes on an Evolving Excited-State Landscape: Insights from Tunable Femtosecond Stimulated Raman Spectroscopy", *J. Phys. Chem. A* **121** (29), 5428-5441 (2017).

[44] S. Shim, C. M. Stuart, and R. A. Mathies, "Resonance Raman cross-sections and vibronic analysis of Rhodamine 6G from broadband stimulated Raman spectroscopy", *ChemPhysChem* **9**, 697-699 (2008).

[45] J. L. McHale, *Molecular Spectroscopy*. (Prentice-Hall, Upper Saddle River, NJ, 1999).

Chapter 7 Simultaneous Solution-Based Generation and Characterization of Crystalline Bismuth Thin Film by Femtosecond Laser Spectroscopy

Liangdong Zhu, Sumit Saha, Weimin Liu, Yanli Wang, Douglas A. Keszler, and Chong Fang*

Applied Physics Letters, **107** (6), 061901, August 10, 2015 DOI: 10.1063/1.4928483

7.1 Abstract

We demonstrate generation and characterization of crystalline bismuth thin film from triphenyl bismuth in methanol. Upon ultraviolet (267 nm) femtosecond laser irradiation of the solution, a thin film of elemental bismuth forms on the inner side of the sample cuvette, confirmed by detection of the coherent A_{1g} optical phonon mode of crystalline bismuth at ~90 cm^{-1}. Probe pulses at 267 and 400 nm are used to elucidate the excited state potential energy surface and photochemical reaction coordinate of triphenyl bismuth in solution with femtosecond resolution. The observed phonon mode blueshifts with increasing irradiation time, likely due to the gradual thickening of nascent bismuth thin film to ~80 nm in 90 min. From femtosecond transient absorption (fs-TA) with the 400 nm probe, we observe a dominant ~4 ps decay time constant of the excited-state absorption signal, which is attributed to a characteristic metal-ligand bond-weakening/breaking intermediate enroute to crystalline metallic thin film from the solution precursor molecules. Our versatile optical setup combining fs-TA and FSRS thus opens an appealing avenue to characterize the laser-induced crystallization process *in situ* and prepare high-quality thin films and nanopatterns "in one pot" directly from solution phase.

7.2 Introduction

Among heavy metals and semimetals, bismuth (Bi) is considered to be a relatively green and environmentally benign element. With growing environmental concerns and the need for greener reagents, interest in Bi and its compounds has steadily increased in the past decade for wide applications in semiconductors, medicine, photocatalysis, gas sensing, optical coating, radiation detection, and thermoelectrics.[1-3] In particular, triphenyl bismuth (Ph_3Bi) has been used as an X-ray contrast agent in orthopedic bone cements,[4] additives for plastics in dentistry,[5] and in medical implants and sutures.[6] From the molecular perspective, this compound contains photolabile Bi–C bonds and is highly soluble in many organic solvents. As a result, the photochemistry of Ph_3Bi can be studied in solution as a precursor to Bi-centered radicals and Bi-containing solids.[7,8] Such photochemistry is also fundamentally relevant to the emerging area of metal oxide photoresists, which now exhibit the highest patterning performance among all known extreme ultraviolet (EUV) materials.[9]

It is known that Ph_3Bi has strong absorption in the UV and experiences homolytic bond cleavage under UV irradiation.[7,10,11] The timescale for relevant radical formation, however, remains unclear. Such studies are challenging because chemical bond rupture could occur on the molecular timescale down to the femtosecond (fs) regime. Therefore, ultrafast spectroscopic methods are needed to study excited state dynamics of such metal-organic complexes in solution,[12-14] particularly regarding the photoinduced metal-to-ligand charge transfer (MLCT) process or metal-ligand bond dissociation. In this work, we study the

photochemistry of Ph_3Bi as a model system for metal-carbon bond breaking. We generate a thin film of Bi directly from Ph_3Bi in methanol solution via fs-laser-induced photolysis and crystallization without use of a chemical reductant. We simultaneously characterize the nascent Bi thin film by analysing a dominant optical phonon mode at ~90 cm^{-1} from spectral oscillations of fs transient absorption. The spectral data with characteristic picosecond (ps) time constants shed light on the photochemical scission of Ph_3Bi in solution, revealing the formation of an intermediate electronic state on the ~4 ps timescale. This *in-situ* methodology thus provides unique insights into Bi–C bond weakening/breaking events and the transition from molecule to condensed solid.

7.3 Experimental design

Our fs laser system consists of a mode-locked Ti:sapphire oscillator (Mantis-5) and regenerative amplifier (Legend Elite-USP-1K-HE, Coherent), providing the fundamental pulse (FP) at 800 nm with 35 fs pulse duration, 4.1 mJ pulse energy at 1 kHz repetition rate. Part of the FP passes through a 1-mm-thick type-I BBO crystal for second harmonic generation (SHG) to obtain the 400 nm pulse. A calcite plate provides compensation for group velocity delay and a zero-order dual waveplate ($\lambda/2$ at 800 nm and λ at 400 nm) is subsequently used to achieve parallel polarization of the 800 and 400 nm pulses. The FP residual and SHG pulses are directed through another 1-mm-thick type-I BBO to generate

the third-harmonic pulse at 267 nm, which is selected with a dichroic mirror to act as the UV pump with ~0.5 μJ pulse energy (Figure 7.1).

Another portion of FP is used to generate either a 400-nm pulse via SHG in BBO or a 267-nm pulse via the broadband up-converted multicolor array technology in a 1-mm-thick calcite crystal plate.[15,16] The probe pulse energy is set at ~100 nJ. A high-resolution motor-controlled delay stage (07EAS504, CVI Melles Griot) is used to tune the time delay between the *s*-polarized pump and probe pulses, which are focused onto the sample solution using an *f*=10 cm lens or UV-enhanced Al-coated concave mirror with ca. 0.2-mm beam diameter at the focal point. The 267-nm probe past the sample is selected through a UV bandpass filter (FGUV11, Thorlabs), then focused and measured by a Si-biased photodiode detector. The time-dependent signal is collected via a lock-in amplifier synchronized to the optical chopper at 500 Hz. For the 400-nm probe, we recollimate the beam and focus it into the spectrograph (MS127i, Oriel) with a 600-grooves/mm, 400-nm blaze grating. The dispersed signal is collected by a CCD array camera (Princeton Instruments, PIXIS 100F) that is synchronized with the laser source to achieve shot-to-shot spectral acquisition. A typical pump-probe scan with enough time delay points and signal averaging takes ~10 minutes. Ph_3Bi was purchased from Alfa Aesar and used without further purification. HPLC-grade methanol (EMD Millipore) was dried by standard procedures and freshly distilled prior to use. All experiments are carried out at atmospheric pressure (1 atm) and room temperature (72 °F). To aid the ground-state Raman mode

assignment, Ph_3Bi is computed in *Gaussian* at the RHF/LANL2DZ level with IEFPCM (integral equation formalism polarizable continuum model)-methanol to include the solution effect on the vibrational normal modes (with the frequency scaling factor of 0.96).[17]

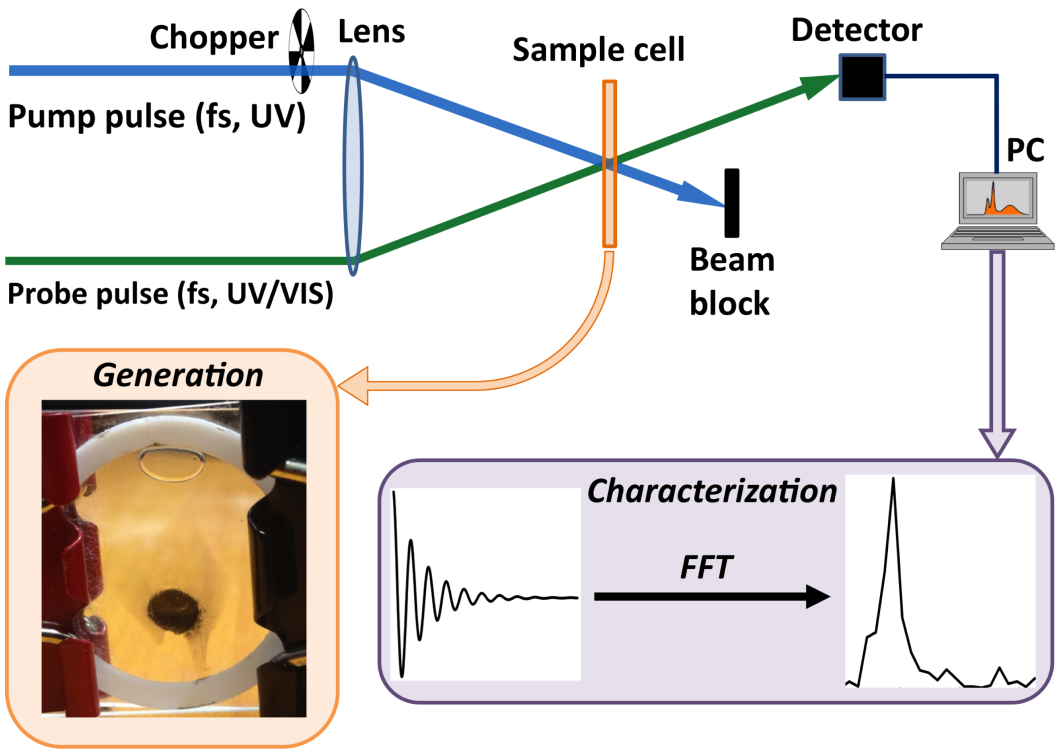

Figure 7.1 Schematic of the experimental setup. In typical noncollinear pump-probe geometry, both laser pulses are focused onto the sample cell while the pump pulse is being chopped. Depending on the probe wavelength, two different detection schemes are used: a lock-in amplifier with Si photodiode for the 267 nm probe, and a dispersive spectrograph with CCD array for the 400 nm probe. Bismuth nanocrystal thin film forms on the inner surface of sample cuvette under femtosecond UV-laser irradiation with ~5-mm beam diameter (bottom left). The characteristic phonon mode is revealed after applying fast Fourier transform (FFT) of the observed spectral oscillations in femtosecond transient absorption (bottom right).

7.4 Results and Discussion

We first irradiate 0.25-M Ph_3Bi in methanol solution in a 1-mm-pathlength quartz cell (Spectrosil 1-Q-1, Starna Cells) with 267-nm pump (ca. 2 μJ/pulse, 5-mm beam diameter) for 20 min. A black thin film forms on the inner side of the front surface (facing incident light) of the sample cuvette, while the solution remains clear and colorless (Figure 7.1 bottom). Interestingly, after ~30 min if we stop the UV irradiation, this black film becomes invisible. Alternatively, if we open the cell to air, the film rapidly becomes visibly transparent, making it difficult to further characterize the thin film. Given that the black film likely consists of Bi metal as the dominant species (see below), the observed film "disappearance" can be explained as Bi being oxidized to form bismuth oxide (Bi_2O_3).[7] Notably, in comparison to pulsed-laser deposition of bismuth thin film in vacuum chamber,[18,19] our solution-based crystallization method is much simpler with less energy footprint.[16] For instance, our pump-laser fluence at $\sim 1\times10^{-5}$ J/cm^2 is much lower than previously used values[18-20] above ~1 mJ/cm^2 because we use a pump pulse with fs time duration.

To substantiate the merit of fs-laser-induced Bi crystallization, we performed an airtight control. In a 50-mL Schlenk flask, 300-mg Ph_3Bi was dissolved in 20-mL dry methanol (sample concentration ≈ 34 mM), stirred for 5 min under an atmosphere of Argon, and irradiated by a mercury UV lamp (Porta-Cure 1000, American Ultraviolet, output wavelength 185–400 nm, non-focused) at 125-W/inch setting for 75 min. After 15 min, the

colorless solution changed to light yellow; after 60 min, it became dark brown. The solvent was removed *in vacuo* to yield a black powder, which mainly contains graphitic carbon and an insignificant amount of elemental Bi as revealed by XRD analysis.[21] Decreasing the Ph_3Bi concentration to 1 mM produces a light yellow solution without formation of black powder even after 120 min under the same condition. Changing the flask to the 1-mm-thick quartz cuvette makes no clear difference. It shows that the UV lamp cannot effectively generate Bi from Ph_3Bi solution, which could be due to much less excitation energy density, more heat-induced degradation, and/or additional photochemistry driven by wavelengths in the UV lamp spectrum that are not in the ultrafast laser bandwidth.

In the UV pump-probe setup with 267 nm pulses, the time-resolved probe transmittance on 1-mM Ph_3Bi in methanol solution as a function of irradiation time is presented in Figure 7.2. The initial dip in transmittance (Figure 7.2a) arises from two-photon absorption of methanol, reflecting the cross correlation between the pump and probe pulses (i.e., ~100 fs instrument response time). This negative peak diminishes with time, which is consistent with the production and crystallization of Bi along the beampath; a control experiment with pure methanol shows the negative peak unchanged with irradiation time. The Bi film formed on the cuvette absorbs at 267 nm, so later datasets develop a positive feature after ~100 fs that is indicative of electronic ground-state bleaching of Bi crystals.[22] After ~30 min, a clear exponential decay of the positive ΔT with oscillations appears with the time constant of ~1 ps (Figure 7.2b). By subtracting the fitted curve from the time-resolved ΔT

trace, the oscillatory residual is obtained (Figure 7.2c). Using fast Fourier transform (FFT), the underlying coherent modulation mode is retrieved at ~90 cm^{-1}, which matches well with the A_{1g} phonon mode of crystalline Bi (Figure 7.2d).[20,23,24] The phonon lifetime is ~500 fs by least-squares fitting the oscillatory trace to a damped sine wave.[24,25] This result indicates that fs-UV pump pulse generates crystalline Bi on the cuvette inner surface, while the transient coherent optical phonon mode is impulsively excited and detected by the pump and probe pulses, respectively.[26-28] We conjecture that the focused fs-pump has sufficient peak density to trigger photolysis of solvated Ph_3Bi to generate crystalline Bi. After a certain amount of film is formed, the pump pulse induces A_{1g} coherent phonons in the Bi nanocrystal film that modulate its ground-state bleaching signal. The aforementioned phonon decay on the sub-ps timescale is mainly due to scattering with the incoherent population elements including thermal phonons, lattice defects, and electrons.[20,25] The observed ~1-ps exponential decay in Figure 7.2b corresponds to the excited-state population relaxation time of Bi crystal.[20]

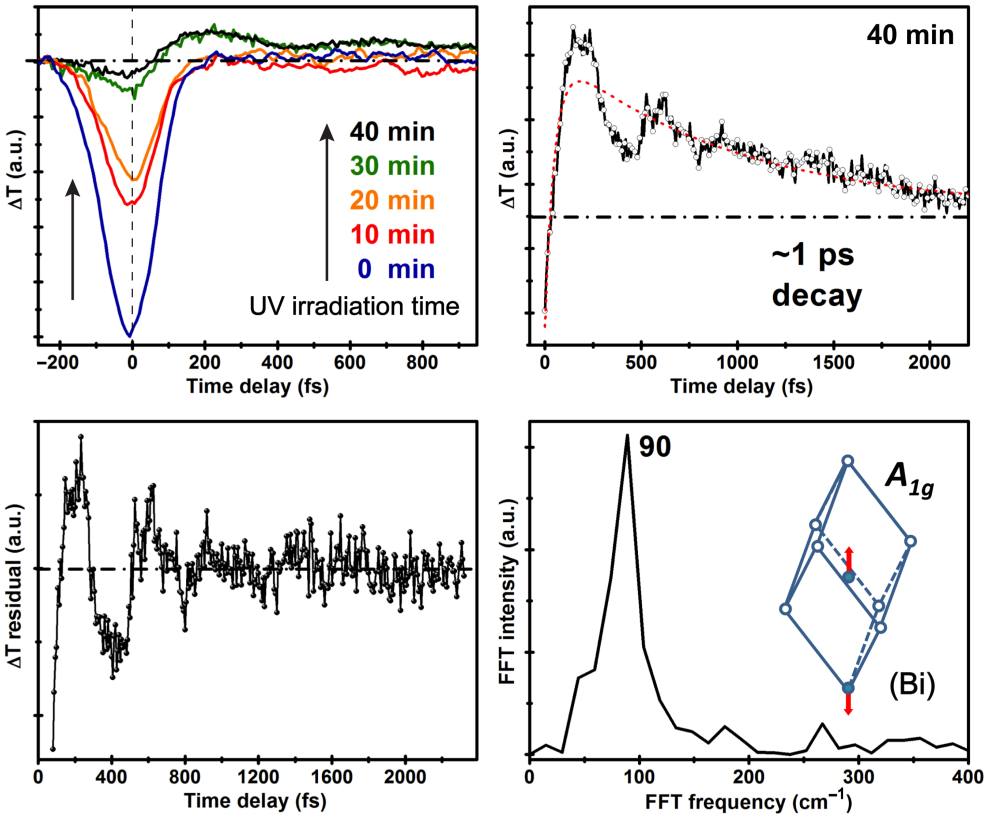

Figure 7.2 Pump-probe spectroscopy on 1-mM Ph_3Bi in methanol solution with 267 nm pulses. (a) Spectral oscillations after ~100 fs become prominent in the time-resolved probe transmittance after ~30 min. The dash-dotted line represents the zero trace. (b) The ΔT plot over a ~2 ps time window (black solid line) shows a ~1 ps exponential decay process (red dashed line). (c) The residual ΔT plot after removing the exponential fit in (b). (d) FFT analysis of the observed coherent oscillations in (c) yields a dominant 90 cm^{-1} mode, attributed to the A_{1g} phonon motion in a rhombohedral unit cell of crystalline Bi (inset).

In order to resolve the phonon dynamics with higher frequency resolution, we further analyze the transient absorption data using discrete Fourier transform (DiFT) without zero padding. Figure 7.3b shows that the phonon mode blueshifts within ~30 min, i.e., from ~86 to 98 cm^{-1}. This result is consistent with the formation and growth of the thin film, because it is observed that the Raman-active A_{1g} mode undergoes a frequency blueshift with increasing thickness and stiffening of the nanocrystal film.[29,30] Meanwhile, because Ph_3Bi absorbs in the UV, we implement tunable femtosecond stimulated Raman spectroscopy (FSRS) using the ps 400-nm Raman pump via a home-built second harmonic bandwidth compressor[31] and the first sideband of sum-frequency-generation-based broadband up-converted multicolor array (SFG-BUMA)[32,33] as Raman probe to characterize the Ph_3Bi precursor. Figure 7.3a presents the anti-Stokes FSRS data with pre-resonance Raman enhancement.[33,34] A number of Raman modes are clearly resolved within a ~1600 cm^{-1} spectral window,[35] suggesting that the Franck-Condon region of photoexcited Ph_3Bi involves significant benzene ring motions and some degree of Bi–C stretching on the sub-ps timescale.[36] Notably, we did not observe a 90 cm^{-1} mode in the ground-state FSRS data of Ph_3Bi solution (Figure 7.3a), corroborating that the phonon mode is associated with the newly generated Bi thin film after photoexcitation (Figure 7.3b).

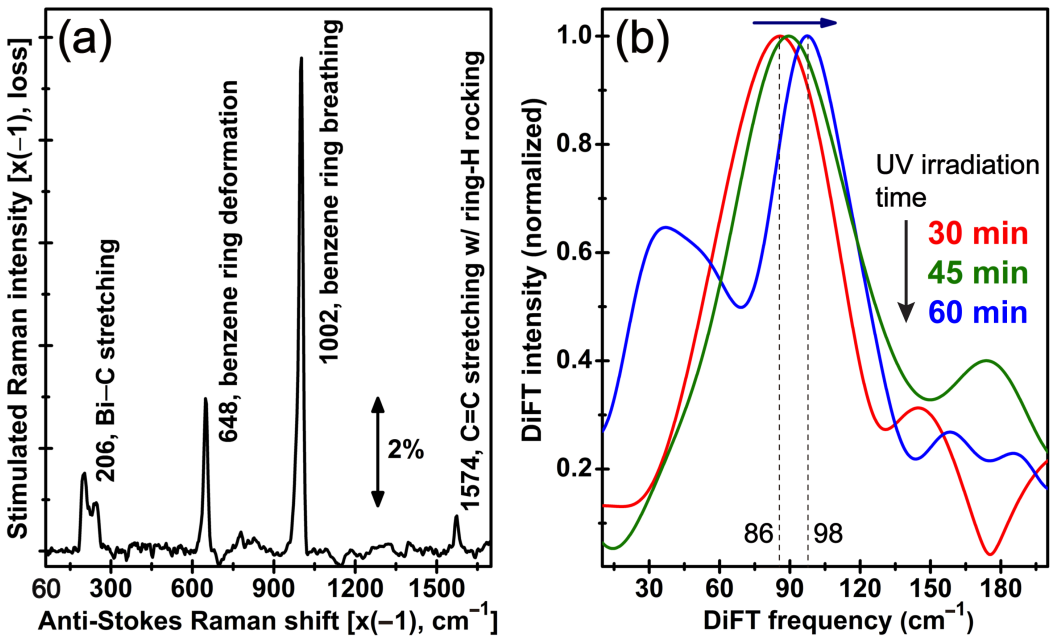

Figure 7.3 Vibrational characterization of the reactant and product species during crystalline Bi thin film formation. (a) Ground-state FSRS spectrum with 400-nm Raman pump of 0.25-M Ph_3Bi in methanol. Major atomic motions are labeled. (b) DiFT result of transient absorption data (e.g., Figure 7.2c) after different time of UV irradiation. The ~90 cm^{-1} mode blueshift as a function of reaction time is indicated by the horizontal arrow.

To provide deeper insights into a different region of the multidimensional potential energy surface of Ph_3Bi in the photoexcited state, we use a 400-nm probe with the 267-nm pump. The transient electronic dynamics differ between datasets with increasing irradiation time, except that a dominant excited-state absorption feature, i.e., positive ΔOD, with a 4.0±0.6 ps exponential decay constant is observed (Figure 7.4 inset b). The time-resolved data trace after ~30 min UV irradiation exhibits an oscillation of ~350 fs period superimposed on the 4-ps decay (Figure 7.4 inset a). The phonon lifetime from least-squares fit of the oscillatory component is ~1 ps, which is consistent with the characteristic damping time of impulsively excited coherent phonons to return to unperturbed positions.[20,27] After the initial decay, the first dataset collected immediately following irradiation (0 min) shows an additional ~165 ps decay (30% weight) that could be related to further bond breaking events. The subsequent negative ΔOD signal recovers on the nanosecond time scale (beyond our current experimental time window of ~600 ps), which is indicative of stimulated emission from a reaction intermediate state. In contrast, following 30 min of UV irradiation the transient data exhibit complex dynamics, wherein, after reaching the minimum at ~20 ps, the negative ΔOD experiences a slow rise (i.e., decay of its magnitude) with nanosecond time constant (see Figure 7.4).

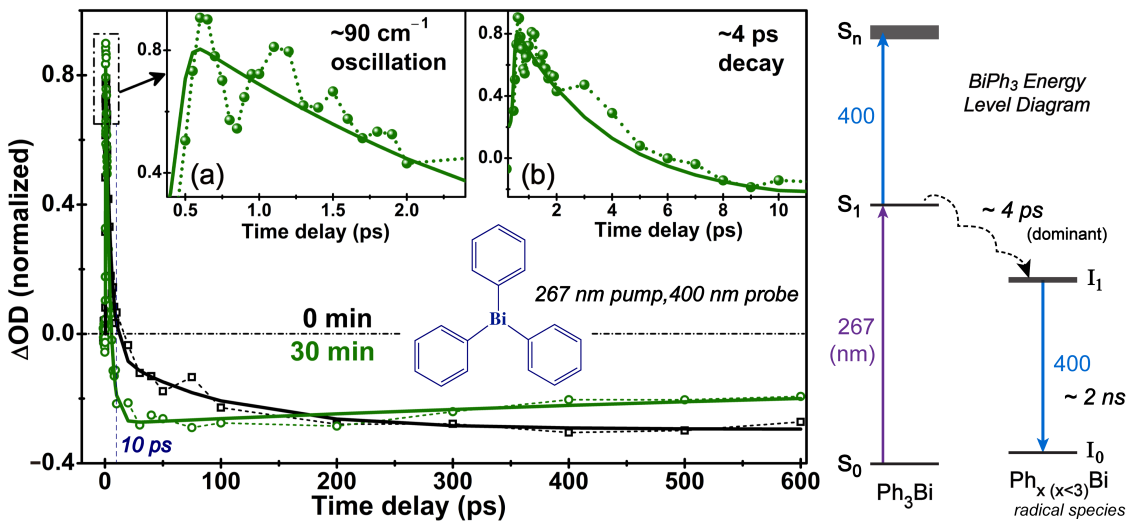

Figure 7.4 . Femtosecond transient absorption spectroscopy of 1-mM Ph_3Bi in methanol solution with 267-nm pump and 400-nm probe pulses. Experimental data at 0 min (black, hollow squares) and 30 min (green, hollow circles) are fitted with multiple exponentials, respectively. Inset (a): Time-resolved spectral oscillations within the first ~2.5 ps after photoexcitation exhibit a dominant ~90 cm^{-1} modulation mode. Inset (b): The ~4 ps initial decay constant from the least-squares fit (solid line) of the excited-state absorption peak kinetic trace up to ~10 ps. The chemical structure of Ph_3Bi is depicted in the inset (below, blue). The proposed main energy level diagram of solvated Ph_3Bi is depicted in the right panel.

This unique series of transient absorption data collected *in situ* during Bi formation provide mechanistic insights into the Ph_3Bi photochemistry in solution. At 0 min, the fs-UV pump pulse excites Ph_3Bi molecules from ground state (S_0) to first singlet excited state (S_1, MLCT), which can further go to a higher lying excited state, e.g., S_2 or S_n. The 4-ps exponential decay of Ph_3Bi excited-state absorption signal reflects the S_1 state relaxation. If all the S_1 population returns to S_0 on the ps timescale, the transient absorption signal would diminish to zero, but we observe an evolving negative signal. The least-squares fitting reveals a ~2 ns recovery process that likely arises from stimulated emission of an intermediate state (I_1) after photoexcited Ph_3Bi navigates out of the Franck-Condon region toward the photolytic reaction state (Figure 7.4, right panel). Before all three Bi–C bonds dissociate to form Bi, some reactive $Ph_2Bi\cdot$ or PhBi: radical species may form in a multi-quantum process without dominant intramolecular electron transfer.[12,37] After ~30 min of UV irradiation, the nascent crystalline Bi absorbs the 400 nm probe to some degree[22] and contributes the ~1 ps decay (~45% weight) of ground-state bleaching (Figure 7.2b), which is coupled to stimulated emission of the I_1 state (~2 ns decay, 55% weight), leading to the observed complex dynamics. Notably, the observation that the ~90 cm^{-1} oscillation associated with impulsively excited A_{1g} coherent phonon motions from the Bi film is pronounced in the 30 min trace (Figure 7.4a) further substantiates this mechanism. Furthermore, after checking the 400-nm probe counts on CCD camera for each pump-probe scan, we note at ~30, 60, and 90 min the transmitted probe intensity decreases by ~74%, 90%, and 93%, respectively. Since the penetration depth of crystalline Bi upon absorbing

400-nm light (~3.1 eV) is ~30 nm[24] while Ph_3Bi in methanol solution does not absorb at 400 nm, we estimate that the thickness of the nascent crystalline Bi film is ~40, 70, and 80 nm after 30, 60, and 90 minutes of UV (267 nm) irradiation, respectively, corroborating the observed phonon frequency blueshift in Figure 7.3b. The fs-laser-induced Bi thin film formation below 100 nm directly from a reactant solution is a notable result of this work.

To elucidate the ultrafast structural dynamics of this photochemical reaction, tunable FSRS with a UV excitation pulse is needed. The ground-state Raman measurement using SFG-BUMA as Raman probe pulse was performed[33] and three peaks of solvated Ph_3Bi stand out in Figure 7.3a: 206 cm^{-1}, Bi–C stretching and Ph_3Bi symmetric stretching; 648 cm^{-1}, benzene ring asymmetric in-plane deformation; and 1002 cm^{-1}, benzene ring breathing motion.[38] Following photoexcitation, the time-resolved FSRS data of Ph_3Bi in solution will expose transient atomic motions by tracking multiple vibrational mode frequencies and intensities[35,36] which reveal molecular structural evolution at the chemical bond level beyond the electronic domain (Figure 7.2 and Figure 7.4). We are in the process of tuning the Raman pump to enhance excited-state FSRS features[31,33] particularly within the first ~10 ps (see Figure 7.4 left panel, vertical dashed line) and unravel the initial photolysis reaction coordinate that leads to the metal thin film. The recent pulse compression in the lab using chirped mirrors for the Raman probe (see Chapter 2) could help acquire FSRS data with improved signal-to-noise ratio and less temporal chirp that may complicate structural dynamics interpretation.

7.5 Conclusions

In conclusion, we use fs 267-nm pump pulse to generate a crystalline Bi thin film directly from Ph_3Bi in methanol and simultaneously monitor the non-equilibrium reactant consumption and product formation with a time-delayed fs-probe pulse either at 267 or 400 nm. We reveal a ~4 ps time constant associated with the excited-state relaxation of Ph_3Bi, which likely involves an intermediate state with weakened and/or broken Bi–C bonds. After a certain thickness (~40 nm) of Bi film is generated, the coherent A_{1g} phonon mode at ~90 cm^{-1} of crystalline Bi is detected in the fs transient absorption and transmittance traces, inferring the dominant electron-lattice coupling in the functional crystalline material. As the nascent Bi film thickens (up to ~80 nm) with time (90 min), a blueshift of the totally symmetric phonon mode is observed. Our setup offers a convenient and viable approach to use fs-laser pulses to generate crystalline metallic thin films from inexpensive solution precursors while offering the opportunity to simultaneously characterize in real time photochemical reaction pathways in electronic and vibrational domains.

7.6 References

[1] G. G. Briand and N. Burford, "Bismuth Compounds and Preparations with Biological or Medicinal Relevance", *Chem. Rev.* **99** (9), 2601-2658 (1999).

[2] N. M. Leonard, L. C. Wieland, and R. S. Mohan, "Applications of Bismuth(III) Compounds in Organic Synthesis", *Tetrahedron* **58** (42), 8373-8397 (2002).

[3] D. G. Cahill, P. V. Braun, G. Chen, D. R. Clarke, S. Fan, K. E. Goodson, P. Keblinski, W. P. King, G. D. Mahan, A. Majumdar, H. J. Maris, S. R. Phillpot, E. Pop, and L. Shi, "Nanoscale Thermal Transport. II. 2003-2012", *Appl. Phys. Rev.* **1** (1), 011305 (2014).

[4] H. R. Rawls, R. J. Granier, J. Smid, and I. Cabasso, "Thermomechanical Investigation of Poly (methylmethacrylate) Containing an Organobismuth Radiopacifying Additive", *J. Biomed. Mater. Res.* **31** (3), 339-343 (1996).

[5] L. O. Reis, M. R. Kaizer, F. A. Ogliari, F. M. Collares, and R. R. Moraes, "Investigation on the Use of Triphenyl Bismuth as Radiopacifier for (Di)Methacrylate Dental Adhesives", *Int. J. Adhes. Adhes.* **48**, 80-84 (2014).

[6] J. Smid, I. Cabasso, A. Obligin, and H. R. Rawls, United States Patent No. 4882392 (Nov. 21, 1989).

[7] D. H. Webber and R. L. Brutchey, "Photochemical Synthesis of Bismuth Selenide Nanocrystals in an Aqueous Micellar Solution", *Inorg. Chem.* **50** (3), 723-725 (2011).

[8] D. Breitwieser, M. Kriechbaum, H. M. A. Ehmann, U. Monkowius, S. Coseri, L. Sacarescu, and S. Spirk, "Photoreductive Generation of Amorphous Bismuth Nanoparticles Using Polysaccharides – Bismuth–Cellulose Nanocomposites", *Carbohydr. Polym.* **116**, 261-266 (2015).

[9] A. Grenville, J. T. Anderson, B. L. Clark, P. De Schepper, J. Edson, M. Greer, K. Jiang, M. Kocsis, S. T. Meyers, J. K. Stowers, A. J. Telecky, D. De Simone, and G. Vandenberghe, "Integrated Fab Process for Metal Oxide EUV Photoresist", *Proc. SPIE 9425, Advances in Patterning Materials and Processes XXXII, 94250S (April 3, 2015)*.

[10] D. H. Hey, D. A. Shingleton, and G. H. Williams, "1075. Homolytic Aromatic Substitution. Part XXIX. The Photolysis of Triphenylbismuth in Aromatic Solvents", *J. Chem. Soc.* (0), 5612-5619 (1963).

[11] P. Weiss, "Photo-Induced Polymerization", *Pure Appl. Chem.* **15** (3), 587-600 (1967).

[12] J. Chen, H. Zhang, I. V. Tomov, X. Ding, and P. M. Rentzepis, "Photochemistry and Electron-Transfer Mechanism of Transition Metal Oxalato Complexes Excited in the Charge Transfer Band", *Proc. Natl. Acad. Sci. U.S.A.* **105** (40), 15235-15240 (2008).

[13] A. S. Mereshchenko, S. K. Pal, K. E. Karabaeva, P. Z. El-Khoury, and A. N.

Tarnovsky, "Photochemistry of Monochloro Complexes of Copper(II) in Methanol Probed by Ultrafast Transient Absorption Spectroscopy", *J. Phys. Chem. A* **116** (11), 2791-2799 (2012).

14 L. Hua, M. Iwamura, S. Takeuchi, and T. Tahara, "The Substituent Effect on the MLCT Excited State Dynamics of Cu(I) Complexes Studied by Femtosecond Time-Resolved Absorption and Observation of Coherent Nuclear Wavepacket Motion", *Phys. Chem. Chem. Phys.* **17** (3), 2067-2077 (2015).

15 W. Liu, L. Wang, F. Han, and C. Fang, "Distinct Broadband Third-Harmonic Generation on a Thin Amorphous Medium-Air Interface", *Opt. Lett.* **38** (17), 3304-3307 (2013).

16 W. Liu, L. Wang, F. Han, and C. Fang, "*In-Situ* Characterization of Femtosecond Laser-Induced Crystallization in Borosilicate Glass using Time-Resolved Surface Third-Harmonic Generation", *Appl. Phys. Lett.* **103** (20), 201116 (2013).

17 M. J. Frisch, G. W. Trucks, H. B. Schlegel, G. E. Scuseria, M. A. Robb, J. R. Cheeseman, G. Scalmani, V. Barone, B. Mennucci, G. A. Petersson, H. Nakatsuji, M. Caricato, X. Li, H. P. Hratchian, A. F. Izmaylov, J. Bloino, G. Zheng, J. L. Sonnenberg, M. Hada, M. Ehara, K. Toyota, R. Fukuda, J. Hasegawa, M. Ishida, T. Nakajima, Y. Honda, O. Kitao, H. Nakai, T. Vreven, J. J. A. Montgomery, J. E. Peralta, F. Ogliaro, M. Bearpark, J. J. Heyd, E. Brothers, K. N. Kudin, V. N. Staroverov, R. Kobayashi, J. Normand, K. Raghavachari, A. Rendell, J. C. Burant, S. S. Iyengar, J. Tomasi, M. Cossi, N. Rega, J. M. Millam, M. Klene, J. E. Knox, J. B. Cross, V. Bakken, C. Adamo, J. Jaramillo, R. Gomperts, R. E. Stratmann, O. Yazyev, A. J. Austin, R. Cammi, C. Pomelli, J. W. Ochterski, R. L. Martin, K. Morokuma, V. G. Zakrzewski, G. A. Voth, P. Salvador, J. J. Dannenberg, S. Dapprich, A. D. Daniels, Ö. Farkas, J. B. Foresman, J. V. Ortiz, J. Cioslowski, and D. J. Fox, *Gaussian 09, Revision B.1* (Gaussian, Inc., Wallingford, CT, 2009).

18 J. C. G. de Sande, T. Missana, and C. N. Afonso, "Optical Properties of Pulsed Laser Deposited Bismuth Films", *J. Appl. Phys.* **80** (12), 7023-7027 (1996).

19 K.-S. Wu and M.-Y. Chern, "Temperature-Dependent Growth of Pulsed-Laser-Deposited Bismuth Thin Films on Glass Substrates", *Thin Solid Films* **516** (12), 3808-3812 (2008).

20 A. A. Melnikov, O. V. Misochko, and S. V. Chekalin, "Ultrafast Eectronic Dynamics in Laser-Excited Crystalline Bismuth", *J. Appl. Phys.* **114** (3), 033502 (2013).

21 S. S. Djokić, N. S. Djokić, and T. Thundat, "Galvanic and Chemical Deposition of Bismuth Powders from Aqueous Solutions", *Journal of The Electrochemical Society* **159** (10), D587-D591 (2012).

22 Y. W. Wang, B. H. Hong, and K. S. Kim, "Size Control of Semimetal Bismuth Nanoparticles and the UV-Visible and IR Absorption Spectra", *J. Phys. Chem. B* **109** (15), 7067-7072 (2005).

23 J. S. Lannin, J. M. Calleja, and M. Cardona, "Second-Order Raman Scattering in

the Group-Vb Semimetals: Bi, Sb, and As", *Phys. Rev. B* **12** (2), 585-593 (1975).

[24] A. A. Melnikov, O. V. Misochko, and S. V. Chekalin, "Generation of Coherent Phonons in Bismuth by Ultrashort Laser Pulses in the Visible and NIR: Displacive versus Impulsive Excitation Mechanism", *Phys. Lett. A* **375** (19), 2017-2022 (2011).

[25] L. Wang, W. Liu, and C. Fang, "Elucidating Low-Frequency Vibrational Dynamics in Calcite and Water with Time-Resolved Third-Harmonic Generation Spectroscopy", *Phys. Chem. Chem. Phys.* **17** (26), 17034-17040 (2015).

[26] T. K. Cheng, S. D. Brorson, A. S. Kazeroonian, J. S. Moodera, G. Dresselhaus, M. S. Dresselhaus, and E. P. Ippen, "Impulsive Excitation of Coherent Phonons Observed in Reflection in Bismuth and Antimony", *Appl. Phys. Lett.* **57** (10), 1004 (1990).

[27] M. F. DeCamp, D. A. Reis, P. H. Bucksbaum, and R. Merlin, "Dynamics and Coherent control of High-Amplitude Optical Phonons in Bismuth", *Phys. Rev. B* **64** (9), 092301 (2001).

[28] M. Hase, M. Kitajima, S.-i. Nakashima, and K. Mizoguchi, "Dynamics of Coherent Anharmonic Phonons in Bismuth Using High Density Photoexcitation", *Phys. Rev. Lett.* **88** (6) (2002).

[29] C. Lee, H. Yan, L. E. Brus, T. F. Heinz, J. Hone, and S. Ryu, "Anomalous Lattice Vibrations of Single- and Few-Layer MoS_2", *ACS Nano* **4** (5), 2695-2700 (2010).

[30] X. Luo, Y. Zhao, J. Zhang, Q. Xiong, and S. Y. Quek, "Anomalous Frequency Trends in MoS_2 Thin Films Attributed to Surface Effects", *Phys. Rev. B* **88** (7), 075320 (2013).

[31] L. Zhu, W. Liu, and C. Fang, "A Versatile Femtosecond Stimulated Raman Spectroscopy Setup with Tunable Pulses in the Visible to Near Infrared", *Appl. Phys. Lett.* **105** (4), 041106 (2014).

[32] W. Liu, L. Zhu, and C. Fang, "Observation of Sum-Frequency-Generation-Induced Cascaded Four-Wave Mixing Using Two Crossing Femtosecond Laser Pulses in a 0.1 mm Beta-Barium-Borate Crystal", *Opt. Lett.* **37** (18), 3783-3785 (2012).

[33] L. Zhu, W. Liu, Y. Wang, and C. Fang, "Sum-Frequency-Generation-Based Laser Sidebands for Tunable Femtosecond Raman Spectroscopy in the Ultraviolet", *Appl. Sci.* **5** (2), 48-61 (2015).

[34] A. B. Myers and R. A. Mathies, in *Biological Applications of Raman Spectroscopy*, edited by T. G. Spiro (John Wiley & Sons, Inc., New York, 1987), Vol. 2, pp. 1-58.

[35] W. Wang, W. Liu, I.-Y. Chang, L. A. Wills, L. N. Zakharov, S. W. Boettcher, P. H.-Y. Cheong, C. Fang, and D. A. Keszler, "Electrolytic Synthesis of Aqueous Aluminum Nanoclusters and *in situ* Characterization by Femtosecond Raman Spectroscopy & Computations", *Proc. Natl. Acad. Sci. U.S.A.* **110** (46), 18397-18401 (2013).

[36] R. R. Frontiera, C. Fang, J. Dasgupta, and R. A. Mathies, "Probing Structural Evolution along Multidimensional Reaction Coordinates with Femtosecond Stimulated Raman Spectroscopy", *Phys. Chem. Chem. Phys.* **14** (2), 405-414

(2012).

[37] O. P. Strausz, J. Connor, and P. J. Young, "Flash Photolysis of Trimethylantimony and Trimethylbismuth and the Quenching of Excited Antimony and Bismuth Atoms", *J. Am. Chem. Soc.* **93** (4), 822-828 (1971).

[38] C. Ludwig, M. Dolny, and H.-J. Götze, "Fourier-Transform Raman and Infrared Spectra and Normal Coordinate Analysis of the Triphenyl Compounds and Their Methyl-, Methoxy- and Fluoro-Substituted Derivatives of Arsenic, Antimony and Bismuth", *Spectrochim. Acta A* **53** (13), 2363-2372 (1997).

Chapter 8 Monitoring Photochemical Reaction Pathways of Tungsten Hexacarbonyl in Solution from Femtoseconds to Minutes

Liangdong Zhu, Sumit Saha, Yanli Wang, Douglas A. Keszler, and Chong Fang*

The Journal of Physical Chemistry B, **120** (51), 13161-13168, December 29, 2016 DOI: 10.1021/acs.jpcb.6b11773

8.1 Abstract

Metal-organic complexes are widely used across disciplines for energy and biological applications, however, their photophysical and photochemical reaction coordinates remain unclear in solution due to pertaining molecular motions on ultrafast timescales. In this study, we apply transient absorption and tunable femtosecond stimulated Raman spectroscopy (FSRS) to investigate the UV photolysis of tungsten hexacarbonyl and subsequent solvent binding events. On the macroscopic timescale with UV lamp irradiation, no equilibrated intermediate is observed from $W(CO)_6$ to $W(CO)_5$(solvent), corroborated by vibrational normal mode calculations. Upon 267 nm femtosecond laser irradiation, the excited-state absorption band within ~400—500 nm exhibits distinct dynamics in methanol, tetrahydrofuran, and acetonitrile on molecular timescales. In methanol, solvation of the nascent pentacarbonyl-solvent complex occurs in ~8 ps and in tetrahydrofuran, 13 ps which potentially involves the associative oxygen-donating ligand rearrangement reaction. In contrast, a stimulated emission feature above 480 nm emerges after ~1 ps in acetonitrile with a nitrogen-donating ligand. These structural dynamics insights demonstrate the combined resolving power of ultrafast electronic and stimulated Raman spectroscopy to elucidate photochemistry of functional organometallic complexes in solution. The delineated reaction pathways in relation to ligand nucleophilicity and solvent reorientation time provide the rational design principles for solution precursors in nanowrite applications.

8.2 Introduction

Group 6 metal carbonyls and their derivatives have been the subject of extensive photophysical and photochemical investigations since the observation of hexacarbonyl photosensitivity in 1961.[1] The pertaining photodissociation is the prototype for metal carbonyl photochemistry and organometallic photoreactions in general.[2] The solvated compounds eliminate a single CO ligand and the resulting unsaturated complexes can lead to functional species that catalyze important industrial and synthetic reactions particularly involving the central metal. Meanwhile, tungsten oxide films can oxidize and reduce reversibly, inducing significant changes in their electrical (specific resistivity)[3] and optical (dielectric)[4,5] properties. Thin films of tungsten trioxide, WO_3, and its oxygen deficient forms, WO_{3-x}, have since been widely studied and used for electrochromic,[6,7] catalytic,[8-10] and gas-sensing[11,12] applications.

The connecting theme and motivation for this work lie in the efficient and sustainable route to prepare such high-quality tungsten oxide thin films directly from solution precursors such as $W(CO)_6$ and its derivatives, which upon annealing or light irradiation, can lose the ligands in a controlled way and yield the desired metal oxide thin films. The fundamental understanding of how these metal-organic complexes behave in solution and respond to light is needed for their future development as functional precursors. We have recently studied the photochemistry of triphenyl bismuth (Ph_3Bi) in methanol, and demonstrated the direct generation and concomitant characterization of crystalline bismuth thin film upon 267 nm femtosecond laser irradiation.[13] Because mixed-metal systems such as the bimetallic Bi–W oxides exhibit appealing applications

from gas sensors, ferroelectric materials,[14,15] to photocatalysts,[16,17] we aim to mechanistically investigate the bimetallic carbonyl complexes including Bi and W metals as solution precursors to sustainably prepare high-quality metal oxide thin films. Therefore, it is crucial to delineate the photodissociation pathway of $W(CO)_6$ in solution before studying the bimetallic complex (ongoing work) so we can gain primary, fundamental mechanistic insights into the chemical bond breaking and formation between the metal center and solvent ligand(s) on the intrinsic molecular timescales.[18,19] In this work, we report such an investigation with synergistic use of the steady-state and time-resolved spectroscopic techniques including femtosecond transient absorption and stimulated Raman on a wide range of timescales, after femtosecond (fs) laser excitation or continuous-wave (cw) lamp irradiation in the ultraviolet (UV) region.

8.3 Experimental methods

Tungsten hexacarbonyl $W(CO)_6$, (99% purity) was purchased from Strem Chemicals, Inc. and used without further purification. For the polar solvents used in this work, HPLC-grade methanol (CH_3OH or MeOH) was purchased from EMD Millipore Corporation, and tetrahydrofuran (THF, ≥99.9%, anhydrous) and acetonitrile (CH_3CN or ACN, 99.8%, anhydrous) were purchased from Sigma-Aldrich. The cw irradiation was performed on the minutes timescale using an unfocused 1000-W UV lamp (broad emission λ=185—400 nm, Porta Cure PC1000, American Ultraviolet Company) at a setting of 125 W/inch.

Our ultrafast laser system consists of a mode-locked Ti:sapphire oscillator (Mantis-5) and an ultrafast regenerative amplifier (Legend Elite-USP-1K-HE, Coherent, Inc.),[13,20,21] which provides the fundamental pulse (FP) centered at 800 nm with ~35 fs pulse duration, 4 W average power at 1 kHz repetition rate. In our fs transient absorption (TA) setup, part of the FP converts to 400 nm through second harmonic generation (SHG) in a 1-mm-thick type-I β-barium borate (BBO) crystal. A calcite plate (Altos Photonics, Inc.) provides the necessary compensation for group velocity delay, followed by a zero-order dual waveplate ($\lambda/2$ at 800 nm; λ at 400 nm) to make the 800 and 400 nm pulses parallel polarized. The FP residual and SHG pulses pass through another 1-mm-thick BBO to generate the third-harmonic pulse at 267 nm, then selected with a dichroic mirror (HR at 257—275 nm, *s*-polarized; HT at 800+400 nm, *p*-polarized) as the ultraviolet (UV) pump pulse at ~0.5 mW. The probe pulse is generated via focusing a small portion of FP onto a 2-mm-thick CaF_2 plate that is mounted on a home-built continuously translating stage powered by a DC linear actuator reciprocating motor, producing the broadband supercontinuum white light (SCWL). To estimate the TA instrument response time in our 1-mm-thick solution sample cell (Spectrosil 1-Q-1, Starna Cells), we measured the cross-correlation time between the UV pump and the SCWL probe and found the full-width-at-half-maximum (FWHM) of the two-photon absorption signal in neat methanol to be ~150 fs.

For the ground state femtosecond stimulated Raman spectroscopy (GS-FSRS), a home-built tunable FSRS apparatus has been described in detail.[20,22,23] Briefly, a small portion of FP is focused on a 2-mm-thick sapphire plate (with higher spectral stability so no motor is needed) to generate

SCWL which goes through a prism pair to compress to ~30 fs pulse duration and used as Raman probe (R_{pr}). The pulse duration of R_{pr} is measured using the optical Kerr effect (OKE) signal between R_{pr} and another fs pulse at 400 nm generated via SHG of the FP.[24,25] The FWHM of the OKE signal is ~40 fs in a 1-mm-thick fused silica glass slide, and assuming the two incident pulse durations are comparable with similar gaussian spectral profiles, the retrieved pulse duration is ~30 fs. The tunable Raman pump (R_{pu}) is generated by a home-built second harmonic bandwidth compressor, a grating-lens-slit-based spectral filter, and a two-stage picosecond (ps) noncollinear optical parametric amplifier. The R_{pu} beam is chopped at half of the laser repetition rate so every other R_{pr} completes the stimulated Raman process and the resultant Raman signal is emitted in the self-heterodyned phase-matching direction (i.e., collinear with the probe beam). We then process and record the FSRS signal by taking the ratio (no additional squaring operation needed) of the R_{pr} spectrum with R_{pu} over that without R_{pu} every 2 ms and averaging for at least 3 seconds to achieve sufficient signal-to-noise ratio.[18,26,27] In a 1-mm-pathlength quartz cell, the sample solution is constantly stirred by a miniature metal staple bar wrapped by a thin layer of parafilm. Steady-state electronic spectroscopy is performed on a Thermo Scientific Evolution 201 UV-Visible spectrophotometer. All the experiments are conducted at room temperature (22 °C) and under atmospheric pressure (1 atm).

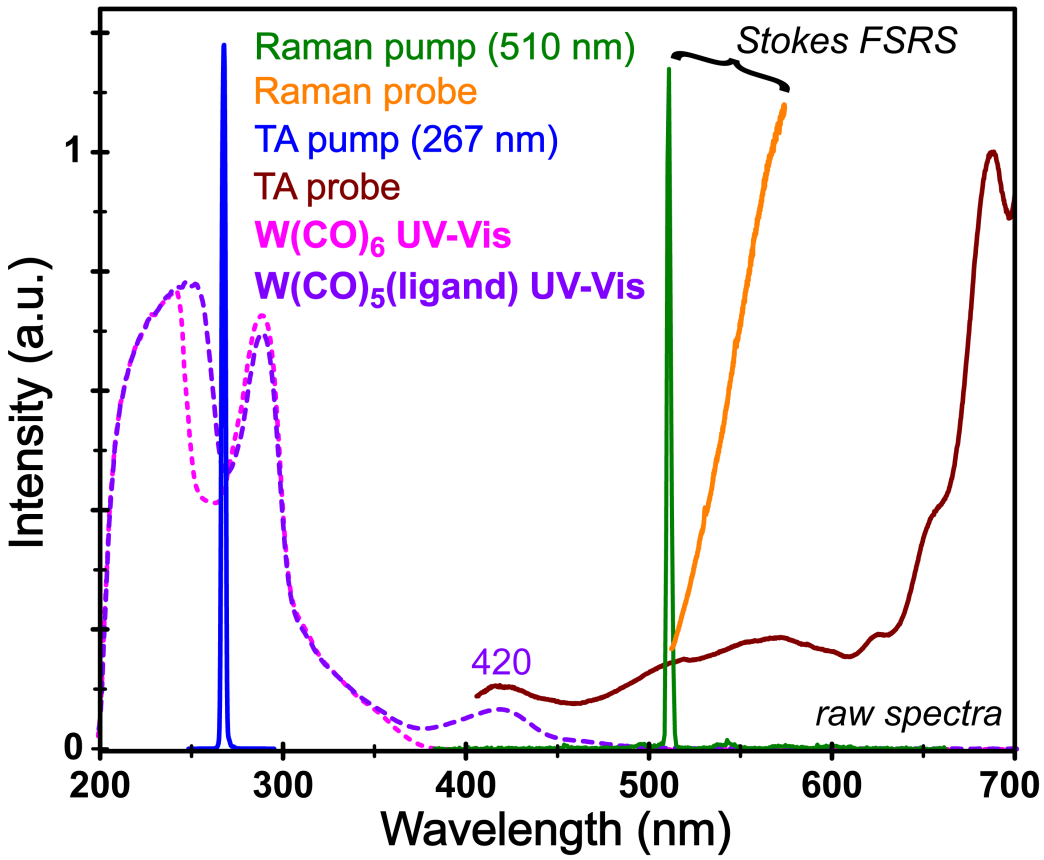

Figure 8.1 Laser spectroscopy and $W(CO)_6$ solution sample absorption profiles. Incident pump and fs probe pulses for FSRS and transient absorption (TA) are color-coded in the spectral domain. The fs TA pump at ~267 nm is shown in blue with the ps Raman pump at 510 nm in green. The UV-Visible absorption of 20 mM $W(CO)_6$ in methanol before (magenta dashed) and after (violet dashed trace) UV lamp irradiation show the emergence of a broad peak at ~420 nm.

8.4 Results and discussion

To investigate the optical behavior and chemical speciation of $W(CO)_6$ in solution under light we first use the cw excitation. Irradiation of 20 mM $W(CO)_6$ in CH_3OH and CH_3CN with a UV lamp changes the solutions from colorless to yellow in ~5 min.[2,28] Overnight, regardless of with light or kept in darkness, the yellow solutions retain their color. This observation indicates an irreversible photochemical reaction upon UV exposure and the resultant photoproduct is light stable. Figure 8.1 presents the steady-state electronic absorption spectra of $W(CO)_6$ in CH_3OH before and after UV irradiation. A new visible absorption band near 420 nm accounts for yellow color of the solution, showing the effective formation of $(CO)_5W(OHCH_3)$ complex after the photolysis of $W(CO)_6$.[2,29,30]

For direct comparison of our experimental conditions particularly regarding the incident laser wavelengths, the two pump-probe pairs in the fs TA and FSRS setups are depicted in the UV to NIR region in Figure 8.1. Notably, the fs TA probe and Raman probe pulses cover a wide spectral range of ~400—700 nm to support the observation of multiple electronic and vibrational bands, respectively, as presented and discussed in detail below. Because the SCWL used as the Raman probe pulse in our setup does not have uniform intensity across the visible range,[31] and in particular for the sapphire plate to generate the nascent SCWL with a sharp drop around 500 nm in the spectral domain, the orange line in Figure 8.1 exhibits a slope instead of being flat. However, it does not affect the FSRS data collection because the stimulated Raman gain is taken as the ratio of the probe (SCWL) spectrum with and without the Raman pump.[26,27] Besides, our spectrograph

has a limited spectral range when the 1200 grooves/mm grating is used at the blaze wavelength of 500 nm to achieve high spectral resolution in the visible region when the probe beam is dispersed inside the spectrograph (SP-2356 Imaging Spectrograph, Princeton Instruments). This optical setup is sufficient to cover the spectral region of interest from ca. 100—2250 cm^{-1} on the Stokes side of the Raman pump (green trace, Figure 8.1).

In order to benchmark vibrational signatures of organometallic compounds in solution,[30,32-37] we perform the GS-FSRS measurement of 20 mM $W(CO)_6$ before and after UV lamp irradiation in three organic solvents (CH_3OH, THF, and CH_3CN). We note this set of experiments is not intended to capture transient structural snapshots during the photochemical reaction, rather it aims to obtain reliable vibrational signatures of the reactant and product on the macroscopic timescales such as minutes following UV lamp irradiation. The rationale to use FSRS instead of an ordinary or resonant Raman setup to expose Raman peaks mainly lies at the high peak power afforded by the ultrafast laser pulses (being orders of magnitude higher in peak density) versus the cw lasers. The FSRS approach also reduces the potential heat effect or sample degradation commonly affiliated with continuous irradiation.[18,38] To further increase the signal-to-noise ratio for the highly symmetrical sample molecules with small Raman cross-sections,[38-40] pre-resonance enhancement is achieved by setting the R_{pu} wavelength at 510 nm and collecting the stimulated Raman scattering signal on the Stokes side.[21,22] The R_{pu} power is ~5 mW and R_{pr} ~150 μW, which is a typical power setting for the two incident pulses in ground-state FSRS experiment. We have recently shown that the ground state FSRS measurement as a function of external perturbation such as the

electrochemically controlled pH change or the cw UV lamp irradiation time can yield previously unavailable physical insights into *flat* aluminum nanocluster formation in water[38] and crystalline bismuth thin film generation in methanol,[13] to name a few.

Figure 8.2 shows the GS-FSRS spectra from ~300 to 2300 cm^{-1} of the reactant and product species in various solutions. The two pronounced clusters of Raman peaks between ca. 400—650 and 1800—2200 cm^{-1} exhibit noticeable changes in response to photoirradiation (see below). To assist the GS Raman assignment, vibrational normal mode frequencies of $W(CO)_6$ with the O_h symmetry in equilibrium S_0 are computed with Hartree-Fock (HF)-LANL2DZ effective core potential and basis set for tungsten (W) as the central transition metal in Gaussian 09,[41] using IEFPCM (integral equation formalism polarizable continuum model) to include the solvent effect. In particular, the corresponding primary photoproduct is the pentacarbonyl species and assumes the molecular structure of $[(CO)_5W\cdots solvent]$ with C_{4v} symmetry.[28,36] The scaling factor is set at 0.95 to compare the calculated frequencies to experimental peak results.

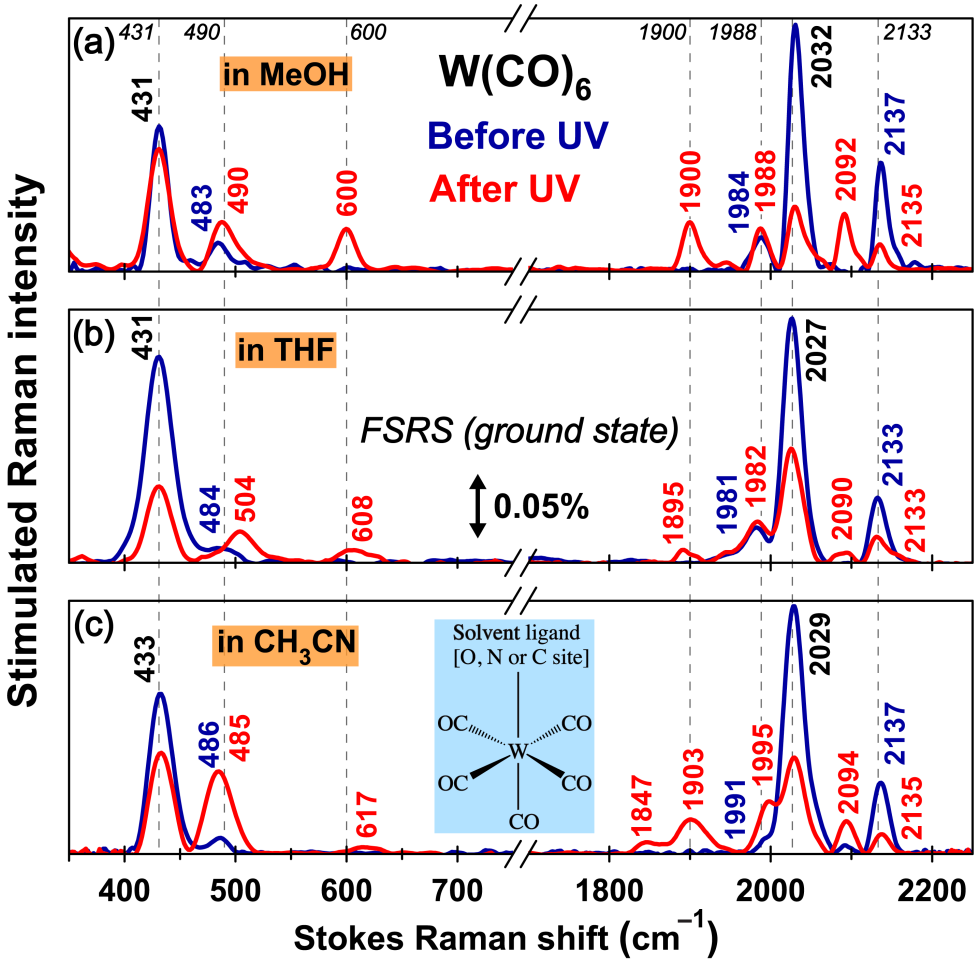

Figure 8.2 Ground state FSRS spectra of 20 mM $W(CO)_6$ in (a) CH_3OH, (b) THF, and (c) CH_3CN before (blue) and after (red trace) UV lamp irradiation. The Raman pump wavelength is 510 nm. Prominent vibrational peaks are labeled in the figure to highlight major spectral changes after photoirradiation. The molecular complex structure is shown in the (c) inset.

Table 8.1. Experimental Raman Mode Frequencies and Assignment Aided by Calculations

Raman mode assignment[a]	$W(CO)_6$ in MeOH / THF / ACN		$W(CO)_5$(MeOH)		$W(CO)_5$(THF)		$W(CO)_5$(ACN)	
	Exp.[b]	Cal.[c]	Exp.[b]	Cal.[c, d]	Exp.[b]	Cal.[c, d]	Exp.[b]	Cal.[c, d]
C–W symmetric stretch, molecular breathing[e, f]	431/431 /433	434/434 /434	N/A					
W–C=O deformation, C–W–C bend[g]	483/484 /486	506/508 /506	490	481	504	477	485	467
In-plane[h] four C=O in-phase wag	N/A		600	611	608	617	617	612
Axial one C=O stretch	N/A		1900	1788	1895	1812	1903	1808
Axial two C=O antisymmetric stretch[i]	1984/1981 /1991	1940/1954 /1939	1988	1896	1982	1906	1995	1899
In-plane[h] four C=O antisymmetric stretch	2032/2027 /2029	2013/2020 /2013	2032	1984	2027	1987	2029	1984
Five C=O symmetric stretch	N/A		2092	2107	2090	2107	2094	2103
All six C=O symmetric stretch[e]	2137/2133 /2137	2147/2151 /2147	N/A					

[a] Aided by quantum calculations, we focus on frequency trend and relative intensities to assign the modes. [b] The S_0 Raman peak frequencies observed by tunable GS-FSRS. [c] Vibrational normal mode frequencies calculated in S_0 with the optimized equilibrium geometry.[41] [d] The relatively large

distance between metal tungsten and the solvent ligand nucleophile site may explain the absence of W–O or W–N stretch. [e] Totally symmetric (A_{1g}) vibrations[42] due to the parent $W(CO)_6$ with O_h symmetry. [f] The asymmetric C–W stretch calculated in $(CO)_5W$(solvent) at ~400 cm^{-1} is not listed (see N/A). [g] In photoproduct species, the listed mode mainly involves the axial C–W stretch. [h] The plane is defined by the four (equatorial) CO groups. See Figure 8.2c inset for illustration. [i] In photoproduct species, this mode involves the "axial" C=O antisymmetric stretch now in the equatorial plane.

The FSRS spectra of $W(CO)_6$ in different solvents are similar except for small frequency shifts (Figure 8.2 and Table 8.1). Five major Raman peaks are observed: C–W symmetric stretch, in-plane C–W–C bend, axial C=O antisymmetric stretch, in-plane C=O antisymmetric stretch, and C=O totally symmetric stretch. Four additional peaks appear after UV irradiation: axial C–W stretch, C=O wag, axial one C=O stretch, and five C=O symmetric stretch. These new peaks reflect the symmetry reduction as one CO dissociates from the original octahedral hexacarbonyl complex, and represent an advantage to IR spectroscopy because only a single active mode C=O stretch is observed therein. In this work, the resultant Raman peak positions and intensity changes exhibit a similar trend (Figure 8.2), showing the decrease of $W(CO)_6$ modes and the increase of photoproduct peaks at ~490, 610, 1900, and 2092 cm^{-1}. This UV-induced photochemical reaction coordinate is corroborated by the calculated frequencies (see Table 8.1) and expanded footnotes in Supporting Information of the paper),[43] particularly the trend upon one solvent ligand complexation.

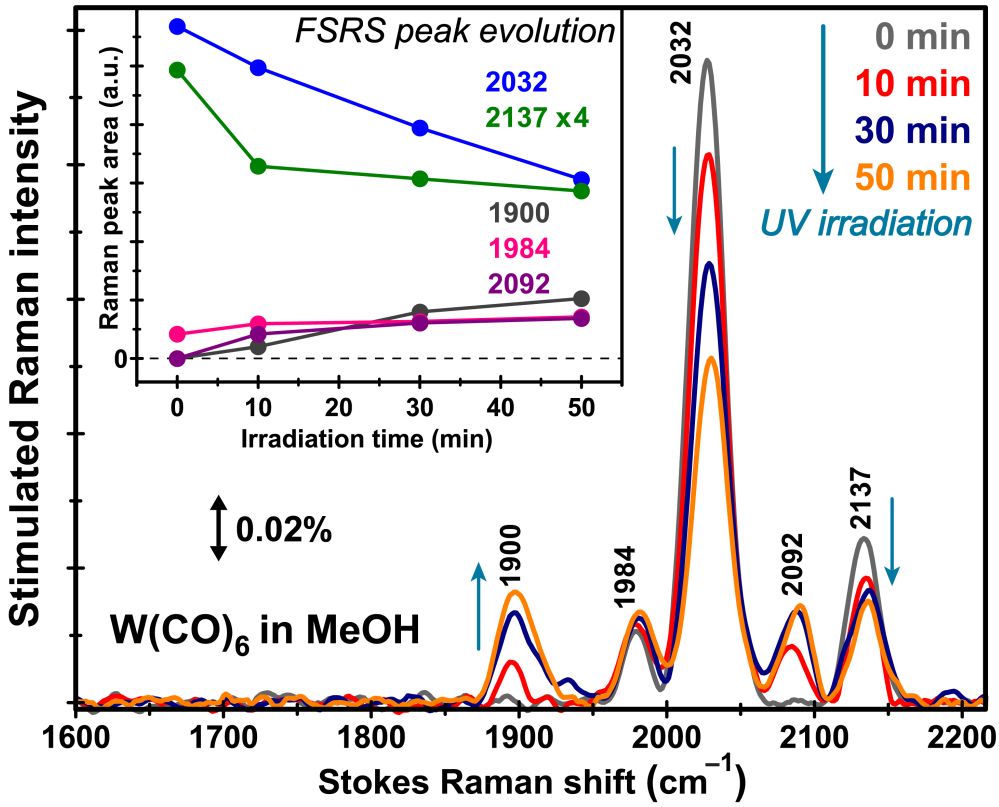

Figure 8.3 Time-resolved GS-FSRS data of 20 mM $W(CO)_6$ in CH_3OH following UV lamp irradiation: 0 (gray), 10 (red), 30 (blue), and 50 (orange) minutes. Time progression is marked by the cyan arrows. The integrated vibrational peak intensity change of several major bands over specific irradiation time is shown in the inset. The stimulated Raman gain magnitude of 0.02% is depicted by the double-arrowed black line.

To dissect the photochemical reaction coordinate on macroscopic timescales and correlate with the solution color change, we used a low-peak-power UV lamp to irradiate 20 mM $W(CO)_6$ in CH_3OH for up to ~1 hour. At each time interval, the UV lamp is turned off and 150,000 GS-FSRS spectra are collected over ~5 minutes, then averaged. In this way, we capture the equilibrium vibrational signatures at defined stages, with the specified irradiation time, from reactant en route to photoproduct. Five marker bands appear within ~1600—2200 cm^{-1} in Figure 8.3 with their time-resolved intensity plot. On the minutes timescale, no intermediate Raman peak is observed, suggesting the ultrafast nature of bond breaking and making events around tungsten metal center in solution.[30,32,44] Moreover, the peak evolution over tens of minutes reflects the population decrease of reactant (e.g., at ~2032 and 2137 cm^{-1}) and increase of product species (e.g., at ~1900 and 2092 cm^{-1} in Figure 8.3 inset, and see mode assignment in Table 8.1).

Further investigation of non-equilibrium electron and atomic motions in the excited state as they proceed requires the time-resolved techniques that dissect photochemical reaction coordinate with sufficient spectral and temporal resolutions.[18,30,32,33,44-47] We perform fs TA experiments on $W(CO)_6$ in various solutions and observe a dominant positive excited-state absorption (ESA) band, which shows distinct dynamics on molecular timescales upon fs UV (267 nm) excitation. The time-resolved spectra in Figure 8.4 elucidate the initial reaction coordinate on the fs to ps timescales in S_1, particularly the singlet MLCT that involves metal-to-ligand charge transfer,[48-50] in conjunction with solvent effect on the photochemical reaction that involves rapid ligand exchange and the intermediate tungsten pentacarbonyl species. We note that the TA results are not

particularly structural because transient electronic not vibrational bands are being monitored, however, the pertaining time constants could provide important dynamics insights particularly when transient molecular species have distinct electronic bands.

After the initial signal rise that is masked by the aforementioned cross-correlation time of ~150 fs (negative time points not shown in the semi-logarithmic graph), the observed ESA data trace in neat methanol (Figure 8.4a) exhibits three distinct stages: a rapid sub-ps decay, a ps rise, and further decay, which can be attributed to the photodissociation of one CO group, solvent ligand complexation, and vibrational relaxation/cooling of the complexed species, respectively. The significance of vibrational cooling could be due to large excess energy upon 267 nm UV excitation versus 300 or 308 nm,[30,44,45,50] and the breaking of the W–C bond is likely accompanied by ultrafast energy transfer and the vibrationally hot CO stretching motions, which were previously monitored by the vibrational up-pumping technique using intense negatively-chirped fs IR pulses.[33] To interpret the fs TA results using fs UV and visible pulses here, we note that the first decay time constant is similar (e.g., ~150—180 fs) across various probe wavelengths (e.g., 410—480 nm),[30,47] whereas the solvent complexation and vibrational relaxation stages differ significantly. The retrieved rise components are ~1.5, 2.5, and 8.1 ps at 480, 440, and 410 nm probe wavelengths, respectively. The first two time constants on the red side largely match the previously observed 2.3 ps rise time for $(CO)_5W(OHCH_3)$ at 440 nm probe following 308 nm laser excitation.[30] The subsequent decay is only observed at 480 and 440 nm with time constants of ~6.0 and 14.9 ps, respectively. This characteristic TA behavior indicates a gradual blueshift of ESA band as the

emerging weakly bound [$(CO)_5W\cdots OHCH_3$] complex is solvated by surrounding methanol molecules.

Qualitatively, solvation events in S_1 stabilize the nascent complex toward an equilibrated [$(CO)_5W–OHCH_3$] complex and thus increase the energy gap between the first excited state and higher-lying states, resulting in an ESA band blueshift. The observed ~8 ps rise at 410 nm correlates well with the average longitudinal relaxation time of methanol (~9 ps),[51,52] which dominates the local dynamic solvation within the first solvation shell of the metal-organic complex. Moreover, the ESA signal decay at 480 nm is faster (~6 ps) than at 440 nm (~15 ps), indicating that the initial [$(CO)_5W\cdots CO$] upon UV excitation rapidly converts to the [$(CO)_5W\cdots$solvent] complex on the few ps timescale. As a result, the ESA band shifts more toward the blue side, hence the lengthened decay time constant at 440 nm. Given the pertaining ps timescale, the solvent ligand substitution is likely via existing H-bonding chains without rearrangement of the entire solvation shell around the complex or diffusion of solvent molecules.[21]

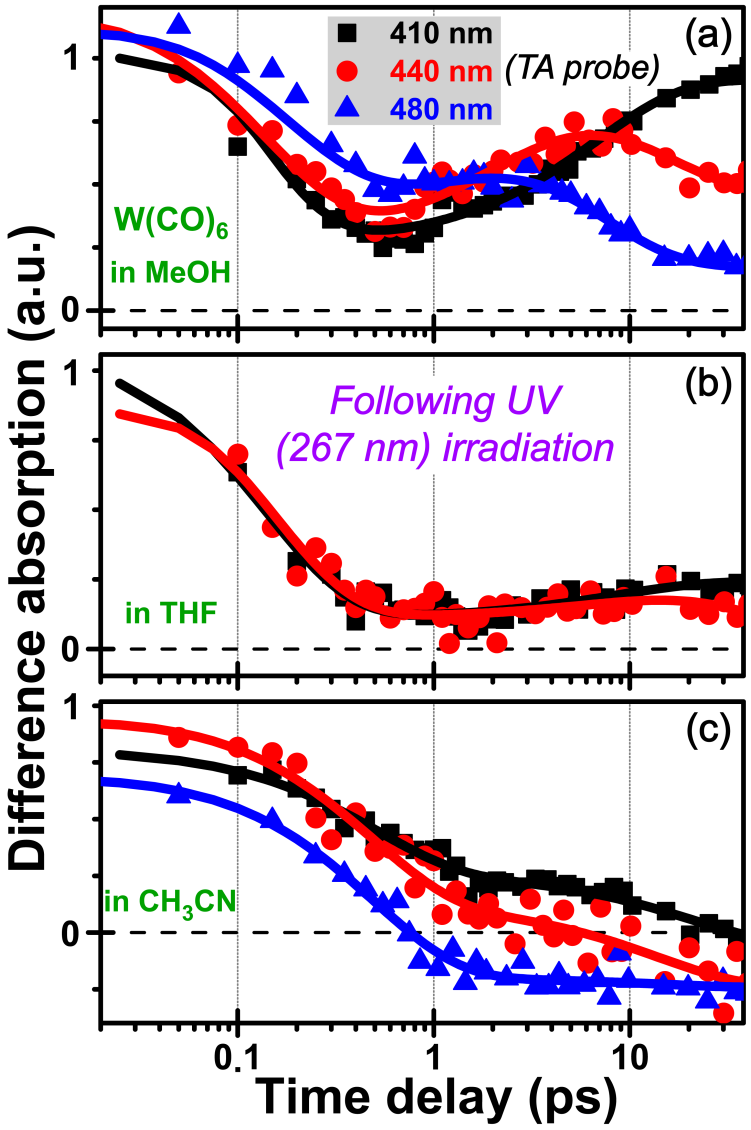

Figure 8.4 Femtosecond transient absorption of ~7 mM $W(CO)_6$ in (a) CH_3OH, (b) THF, and (c) CH_3CN following 267 nm photoexcitation. Time evolution of the integrated (i.e., ±5 nm) ΔOD at three probe wavelengths, 410 (black squares), 440 (red circles), and 480 nm (blue triangles, except in THF), is shown against pump-probe time delay in the semi-logarithmic scale. Color-coded symbols represent the experimental data points, and solid curves display the least-squares multi-exponential fit.

In THF, a similar decay-rise-decay pattern is observed at 440 nm but with a much weaker ESA signal, likely due to a less stable pentacarbonyl-solvent complex than that in CH_3OH. At 410 (440) nm, the initial decay time constant is ~150 (200) fs and the rise time constant is ~13.0 (12.5) ps (see Figure 8.4b). Because THF has four alkyl sites and one heteroatom site that can donate electrons to W, it is plausible that UV photolysis induces rapid and random coordination of W via the vacant site left by one CO to all available solvent sites.[35,46] Meanwhile, the solvent coordination time constants for the metal pentacarbonyl photoproducts are estimated to be smaller than ~3 ps.[30,44] The O-coordinated complex is thermodynamically more stable than the C-coordinated complex, reflecting the increased electron-donating ability of the O-containing group versus the alkyl group to the metal center. Therefore, it takes ~13 ps to undergo "local" ligand rearrangement[35,36] (i.e., for the solvent ligand THF with more than twice the volume of CH_3OH or CH_3CN) and the ESA blueshift is reflected by the dynamic trace at 410 nm. Meanwhile, a further decay component with ~21.5 ps time constant at 440 nm can be attributed to vibrational relaxation[30,33] and/or cooling of the remaining alkyl-coordinated complexes in the ensemble TA measurement.[32]

Interestingly, in contrast to CH_3OH and CH_3CN cases, the yellow solution of UV-irradiated $W(CO)_6$ in THF turns colorless overnight when being kept in the dark, and turns yellow again with light, suggesting the occurrence of a reversible transformation. This interesting observation corroborates the nature of the weak $(CO)_5W(THF)$ complex,[2] wherein the cyclic and bulky ring of THF as well as its reduced nucleophilicity makes the pentacarbonyl-solvent complex unstable in

solution. It is worth mentioning that the dielectric constant of THF (7.5) is significantly smaller than CH_3OH (32.6) or CH_3CN (36.6). Our observation may also be related to the equilibrium gas solubility of CO in the heterocyclic THF which is lower than that in the straight-chain CH_3OH and CH_3CN solvents. The equilibrium may be shifted in THF due to instability of the product species. Meanwhile, the reversible reaction for the CO ligand to displace the solvent ligand and re-coordinate to the metal center proceeds on a timescale presumably set by diffusion.

Notably, the TA results of $W(CO)_6$ in CH_3CN are quite different (Figure 8.4c). The dominant intensity decay constants are ~360, 540, and 600 fs measured at 410, 440, and 480 nm, much longer than their counterparts in CH_3OH (Figure 8.4a) or THF (Figure 8.4b) on the sub-ps timescale. This is due to weaker binding between W and N than binding between W and O, and the decreased initial driving force particularly at early time to form the metal-solvent-ligand chemical bond. In addition, the absence of a rise in this region (>400 nm) can be explained by a further blueshifted ESA band (i.e., below 400 nm) of the nascent tungsten pentacarbonyl-solvent species. The longer decay time constants are ~17.3, 15.4, and 12.0 ps at 410, 440, and 480 nm, respectively, crossing the zero line after ~1 ps. This decay component matches the average vibrational cooling time of ~16 ps measured from time-resolved IR of the $(CO)_5W(NCCH_3)$ photoproduct.[37,49] The emerging negative signal is attributed to stimulated emission from the solvated $[(CO)_5W\cdots NCCH_3]$ complex, corroborated by previous reports of the ~530 nm luminescence from $W(CO)_5$ coupled to a distinct nitrogen or other *n*-electron donors.[2,48]

To reveal detailed structural dynamics during ultrafast photochemical reaction from a fresh perspective, we performed the excited state FSRS experiment[19,21,23] using a UV (267 nm) fs excitation pulse aiming to capture the transient Raman features in S_1. The unique attributes of resonance FSRS should enable the selective enhancement of transient Raman features along the $W(CO)_6$ photodissociation pathway, leading to the formation of the pentacarbonyl-solvent complex. At R_{pu}=500, 505, and 510 nm, weak Stokes Raman peaks are observed between ~400—500 cm^{-1} that are likely associated with photoinduced ultrafast changes of the C–W stretching and bending motions (Table 8.1).[50] The low signal-to-noise ratio, however, hinders further quantitative analysis. This early-stage endeavor to capture the desirable transient Raman features was likely affected by the electronic potential energy landscape of the photoproduct species which absorbs in the bluer region to our stimulated Raman pulses. We plan to tune the Raman pump further to the blue and collect the anti-Stokes signal,[20,53] which should increase the resonance enhancement factor and expose stronger Raman peaks along the reaction coordinate from the reactant, intermediate(s), to photoproduct(s). One possible experimental strategy is to use the SHBC output at 400 nm as the ps Raman pump (see Chapter 4) and one of the sidebands of the SFG-BUMA as the fs Raman probe (see Chapter 6) to collect the anti-Stokes FSRS signal.[20,54,55]

Notably, the anharmonic couplings between CO stretch and low-frequency motions[34,47,49] (see Table 8.1) could be assessed by analyzing the time-resolved vibrational peak evolution at multiple spectral locations, without complication from the conventional transient absorption that typically

shows overlapping electronic bands.[19,21] As the technical advance is underway in the ultrafast spectroscopy laboratory, we expect to provide a much fuller picture of the UV photolysis of tungsten hexacarbonyl in solution in the near future.

Moreover, we find that $W(CO)_6$ in nonpolar solvents[42] such as CCl_4 or cyclohexane upon ~1 mW, 267 nm fs-laser irradiation does not turn the originally colorless solution yellow, instead a blue thin film is formed around the laser focusing spot (~3 mm diameter) in ~30 minutes, which can be attributed to the air-stable WO_3 metal oxide. This rather unexpected observation not only hints fundamental chemistry principles in play, which differs from the aforementioned photodissociation pathways of $W(CO)_6$ in polar solvents that lead to stable to semi-stable pentacarbonyl species, it also represents a solid step toward atom-efficient, green chemistry methods to fabricate metal oxide thin films directly from solution.[13,38] We further demonstrate that the UV lamp irradiation exerts similar but more global effect on the precursor solution: after ~1 min the solution turns dark brown, and after ~15 min at room temperature, a blue solid precipitates from the clear solution. Overnight, blue powder and colorless crystals form which are characterized by FTIR spectroscopy as WO_3 and $W(CO)_6$, respectively. This drastically different photochemical outcome in nonpolar solvents versus the polar solvents speaks to the importance of solute-solvent interactions and solvation dynamics in guiding the photochemical reaction pathways toward product species,[21,40,56] which represents an exciting area for further research as well as an appealing route to nanowrite with metal tungsten.

8.5 Conclusions

To recapitulate, we have employed the ultrafast transient absorption and wavelength-tunable femtosecond stimulated Raman spectroscopy to elucidate the equilibrium and non-equilibrium pathways leading to photoproduct formation after UV lamp or 267 nm fs laser irradiation. Aided by *ab initio* quantum chemical calculations, we benchmark the ground state Raman signatures of tungsten hexacarbonyl and solvated tungsten pentacarbonyl complexes in the polar protic (CH_3OH) and aprotic (THF, CH_3CN) solvents, confirming the substitution of one CO with a solvent ligand as well as the associative mechanism with high sensitivity of reaction rate to the entering ligand. The UV lamp irradiation on the tens of minutes timescale gradually converts the hexacarbonyl to the pentacarbonyl species without noticeable equilibrated intermediates, and the associated key vibrational bands support the two-state reaction model. The fs transient electronic absorption reveals previously unobserved solvation dynamics of the nascent $[(CO)_5W\cdots solvent]$ complex, ~8 ps in CH_3OH and 13 ps in THF, arising from the ultrafast interplay between solvent ligand size, reorientation time, and binding energy to central metal in the local environment. More work remains to be done to record the time-resolved Raman peak evolution during the photochemical reaction with sufficient signal-to-noise ratio, but the experimental results in this work lay the solid foundation (e.g., time constants, electronic and vibrational marker bands, reaction phases) for the femtosecond Raman technology to contribute further to this fundamental yet highly functional molecular system. We expect that the deepened mechanistic understanding of structure-reactivity relationships of photodissociated metal carbonyls in solution, particularly

for the early-time primary events that invoke key atomic sites for metal-organic complexation, paves the path to enable rational design and generation of photocatalysts and high-quality metal oxide thin films from inexpensive solution precursors.

8.6 References

[1] W. Strohmeier, K. Gerlach, and D. V. Hobe, "Photochemische Darstellung von Amin-Derivaten von Metallhexacarbonylen", *Chem. Ber.* **94** (1), 164-168 (1961).

[2] M. Wrighton, "Photochemistry of Metal Carbonyls", *Chem. Rev.* **74** (4), 401-430 (1974).

[3] M. Regragui and A. Donnadieu, "Caractérisation Electrique et Optique de Couches Minces de WO_3 et MoO_3 Préparées par Décomposition en Phase Vapeur (CVD)", *J. Phys. III France* **2** (3), 383-394 (1992).

[4] S. K. Deb, "Optical and Photoelectric Properties and Colour Centres in Thin Films of Tungsten Oxide", *Philos. Mag.* **27** (4), 801-822 (1973).

[5] B. W. Faughnan, R. S. Crandall, and P. M. Heyman, "Electrochromism in WO_3 Amorphous Films", *Rca Review* **36** (1), 177-197 (1975).

[6] G. A. Niklasson and C. G. Granqvist, "Electrochromics for Smart Windows: Thin Films of Tungsten Oxide and Nickel Oxide, and Devices Based on These", *J. Mater. Chem.* **17** (2), 127-156 (2007).

[7] A. Georg, A. Georg, W. Graf, and V. Wittwer, "Switchable Windows with Tungsten Oxide", *Vacuum* **82** (7), 730-735 (2008).

[8] H. Zhang, G. Chen, and D. W. Bahnemann, "Photoelectrocatalytic Materials for Environmental Applications", *J. Mater. Chem.* **19** (29), 5089-5121 (2009).

[9] J. A. Rodriguez and D. Stacchiola, "Catalysis and the Nature of Mixed-Metal Oxides at the Nanometer Level: Special Properties of MOx/TiO_2 (110){M= V, W, Ce} Surfaces", *Phys. Chem. Chem. Phys.* **12** (33), 9557-9565 (2010).

[10] R. Liu, Y. Lin, L. Y. Chou, S. W. Sheehan, W. He, F. Zhang, H. J. M. Hou, and D. Wang, "Water Splitting by Tungsten Oxide Prepared by Atomic Layer Deposition and Decorated with an Oxygen‐Evolving Catalyst", *Angew. Chem. Int. Ed.* **50** (2), 499-502 (2011).

[11] K. Zakrzewska, "Mixed Oxides as Gas Sensors", *Thin solid films* **391** (2), 229-238 (2001).

[12] A. Gurlo, "Nanosensors: towards Morphological Control of Gas Sensing Activity. SnO_2, In_2O_3, ZnO and WO_3 Case Studies", *Nanoscale* **3** (1), 154-165 (2011).

[13] L. Zhu, S. Saha, W. Liu, Y. Wang, D. A. Keszler, and C. Fang, "Simultaneous Solution-Based Generation and Characterization of Crystalline Bismuth Thin Film by Femtosecond Laser Spectroscopy", *Appl. Phys. Lett.* **107** (6), 061901 (2015).

[14] K. Ishikawa, T. Watanabe, and H. Funakubo, "Preparation of Bi_2WO_6 Thin Films by Metalorganic Chemical Vapor Deposition and Their Electrical Properties", *Thin Solid Films* **392** (1), 128-133 (2001).

[15] P. S. Berdonosov, D. O. Charkin, V. A. Dolgikh, S. Y. Stefanovich, R. I. Smith, and P. Lightfoot, "$Bi_{2-x}Ln_xWO_6$: a Novel Layered Structure Type Related to the Aurivillius Phases", *J. Solid State Chem.* **177** (7), 2632-2634 (2004).

[16] R. Rangel, P. Bartolo-Pérez, A. Gómez-Cortés, G. Díaz, S. Fuentes, and D. H. Galván, "Comparison Between γ-Bi_2MoO_6 and Bi_2WO_6 Catalysts in the CO Oxidation", *J. Mater. Synth. Process* **9** (4), 207-212 (2001).

[17] C. Zhang and Y. Zhu, "Synthesis of Square Bi_2WO_6 Nanoplates as High-Activity Visible-Light-Driven Photocatalysts", *Chem. Mater.* **17** (13), 3537-3545 (2005).

[18] R. R. Frontiera, C. Fang, J. Dasgupta, and R. A. Mathies, "Probing Structural Evolution along Multidimensional Reaction Coordinates with Femtosecond Stimulated Raman Spectroscopy", *Phys. Chem. Chem. Phys.* **14** (2), 405-414 (2012).

[19] B. G. Oscar, W. Liu, Y. Zhao, L. Tang, Y. Wang, R. E. Campbell, and C. Fang, "Excited-State Structural Dynamics of a Dual-Emission Calmodulin-Green Fluorescent Protein Sensor for Calcium Ion Imaging", *Proc. Natl. Acad. Sci. U.S.A.* **111** (28), 10191-10196 (2014).

[20] L. Zhu, W. Liu, Y. Wang, and C. Fang, "Sum-Frequency-Generation-Based Laser Sidebands for Tunable Femtosecond Raman Spectroscopy in the Ultraviolet", *Appl. Sci.* **5** (2), 48-61 (2015).

[21] W. Liu, Y. Wang, L. Tang, B. G. Oscar, L. Zhu, and C. Fang, "Panoramic Portrait of Primary Molecular Events Preceding Excited State Proton Transfer in Water", *Chem. Sci.* **7** (8), 5484-5494 (2016).

[22] L. Zhu, W. Liu, and C. Fang, "A Versatile Femtosecond Stimulated Raman Spectroscopy Setup with Tunable Pulses in the Visible to Near Infrared", *Appl. Phys. Lett.* **105** (4), 041106 (2014).

[23] F. Han, W. Liu, L. Zhu, Y. Wang, and C. Fang, "Initial Hydrogen-Bonding Dynamics of Photoexcited Coumarin in Solution with Femtosecond Stimulated Raman Spectroscopy", *J. Mater. Chem. C* **4** (14), 2954-2963 (2016).

[24] A. Bouhal, R. Evans, G. Grillon, A. Mysyrowicz, P. Breger, P. Agostini, R. C. Constantinescu, H. G. Muller, and D. von der Linde, "Cross-Correlation Measurement of Femtosecond Noncollinear High-Order Harmonics", *J. Opt. Soc. Am. B* **14** (4), 950-956 (1997).

[25] Y. Ding, F. J. Decker, P. Emma, C. Feng, C. Field, J. Frisch, Z. Huang, J. Krzywinski, H. Loos, J. Welch, J. Wu, and F. Zhou, "Femtosecond X-Ray Pulse Characterization in Free-Electron Lasers Using a Cross-Correlation Technique", *Phys. Rev. Lett.* **109** (25), 254802 (2012).

[26] D. W. McCamant, P. Kukura, S. Yoon, and R. A. Mathies, "Femtosecond Broadband Stimulated Raman Spectroscopy: Apparatus and Methods", *Rev. Sci. Instrum.* **75** (11), 4971-4980 (2004).

[27] W. Liu, F. Han, C. Smith, and C. Fang, "Ultrafast Conformational Dynamics of Pyranine during Excited State Proton Transfer in Aqueous Solution Revealed by Femtosecond Stimulated Raman Spectroscopy", *J. Phys. Chem. B* **116** (35), 10535-10550 (2012).

[28] M. A. Graham, M. Poliakoff, and J. J. Turner, "Photochemistry of the Group VI Hexacarbonyls in Low Temperature Matrices. Part I. The Pentacarbonyls of Chromium, Molybdenum, and Tungsten", *J. Chem. Soc. A: Inorg. Phys. Theor.* **1971** (0), 2939-2948 (1971).

[29] M. J. Schadt, N. J. Gresalfi, and A. J. Lees, "Characterization and Reaction Kinetics of Intermediates Produced in the Photolysis of $M(CO)_6$ (M = Cr, Mo, W) Solutions

Containing a 1,4-Diazabutadiene Ligand", *Inorg. Chem.* **24** (19), 2942-2946 (1985).

30 A. G. Joly and K. A. Nelson, "Metal Carbonyl Photochemistry in Organic Solvents: Femtosecond Transient Absorption and Preliminary Resonance Raman Spectroscopy", *Chem. Phys.* **152** (1–2), 69-82 (1991).

31 A. Zheltikov, "Editorial: Supercontinuum Generation", *Appl. Phys. B* **77** (2-3), 143-147 (2003).

32 J. C. King, J. Z. Zhang, B. J. Schwartz, and C. B. Harris, "Vibrational Relaxation of $M(CO)_6$ (M=Cr, Mo, W): Effect of Metal Mass on Vibrational Cooling Dynamics and Non-Boltzmann Internal Energy Distributions", *J. Chem. Phys.* **99** (10), 7595-7601 (1993).

33 S. M. Arrivo, T. P. Dougherty, W. T. Grubbs, and E. J. Heilweil, "Ultrafast Infrared Spectroscopy of Vibrational CO-Stretch Up-Pumping and Relaxation Dynamics of $W(CO)_6$", *Chem. Phys. Lett.* **235** (3–4), 247-254 (1995).

34 A. Tokmakoff and M. D. Fayer, "Infrared Photon Echo Experiments: Exploring Vibrational Dynamics in Liquids and Glasses", *Acc. Chem. Res.* **28** (11), 437-445 (1995).

35 J. E. Shanoski, C. K. Payne, M. F. Kling, E. A. Glascoe, and C. B. Harris, "Ultrafast Infrared Mechanistic Studies of the Interaction of 1-Hexyne with Group 6 Hexacarbonyl Complexes", *Organometallics* **24** (8), 1852-1859 (2005).

36 J. E. Shanoski, E. A. Glascoe, and C. B. Harris, "Ligand Rearrangement Reactions of $Cr(CO)_6$ in Alcohol Solutions: Experiment and Theory", *J. Phys. Chem. B* **110** (2), 996-1005 (2006).

37 M. Banno, K. Iwata, and H.-o. Hamaguchi, "Intra- and Intermolecular Vibrational Energy Transfer in Tungsten Carbonyl Complexes $W(CO)_5(X)$ (X=CO, CS, CH_3CN, and CD_3CN)", *J. Chem. Phys.* **126** (20), 204501 (2007).

38 W. Wang, W. Liu, I.-Y. Chang, L. A. Wills, L. N. Zakharov, S. W. Boettcher, P. H.-Y. Cheong, C. Fang, and D. A. Keszler, "Electrolytic Synthesis of Aqueous Aluminum Nanoclusters and *in situ* Characterization by Femtosecond Raman Spectroscopy & Computations", *Proc. Natl. Acad. Sci. U.S.A.* **110** (46), 18397-18401 (2013).

39 A. B. Myers and R. A. Mathies, in *Biological Applications of Raman Spectroscopy*, edited by T. G. Spiro (John Wiley & Sons, Inc., New York, 1987), Vol. 2, pp. 1-58.

40 J. L. McHale, *Molecular Spectroscopy*. (Prentice-Hall, Upper Saddle River, NJ, 1999).

41 M. J. Frisch, G. W. Trucks, H. B. Schlegel, G. E. Scuseria, M. A. Robb, J. R. Cheeseman, G. Scalmani, V. Barone, B. Mennucci, G. A. Petersson, H. Nakatsuji, M. Caricato, X. Li, H. P. Hratchian, A. F. Izmaylov, J. Bloino, G. Zheng, J. L. Sonnenberg, M. Hada, M. Ehara, K. Toyota, R. Fukuda, J. Hasegawa, M. Ishida, T. Nakajima, Y. Honda, O. Kitao, H. Nakai, T. Vreven, J. J. A. Montgomery, J. E. Peralta, F. Ogliaro, M. Bearpark, J. J. Heyd, E. Brothers, K. N. Kudin, V. N. Staroverov, R. Kobayashi, J. Normand, K. Raghavachari, A. Rendell, J. C. Burant, S. S. Iyengar, J. Tomasi, M. Cossi, N. Rega, J. M. Millam, M. Klene, J. E. Knox, J. B. Cross, V. Bakken, C. Adamo, J. Jaramillo, R. Gomperts, R. E. Stratmann, O. Yazyev, A. J. Austin, R. Cammi, C. Pomelli, J. W. Ochterski, R. L. Martin, K. Morokuma, V. G. Zakrzewski, G. A. Voth, P. Salvador, J. J. Dannenberg, S. Dapprich, A. D. Daniels, Ö. Farkas, J. B. Foresman, J. V. Ortiz, J. Cioslowski, and D. J. Fox, *Gaussian 09, Revision*

B.1 (Gaussian, Inc., Wallingford, CT, 2009).

[42] A. Tokmakoff, B. Sauter, A. S. Kwok, and M. D. Fayer, "Phonon-Induced Scattering between Vibrations and Multiphoton Vibrational Up-Pumping in Liquid Solution", *Chem. Phys. Lett.* **221** (5–6), 412-418 (1994).

[43] L. Zhu, S. Saha, Y. Wang, D. A. Keszler, and C. Fang, "Monitoring Photochemical Reaction Pathways of Tungsten Hexacarbonyl in Solution from Femtoseconds to Minutes. ", *J. Phys. Chem. B* **120**, 13161-13168 (2016).

[44] J. D. Simon and X. Xie, "Photodissociation of Chromium Hexacarbonyl in Solution: Direct Observation of the Formation of Pentacarbonyl(Methanol)Chromium", *J. Phys. Chem.* **90** (26), 6751-6753 (1986).

[45] A. G. Joly and K. A. Nelson, "Femtosecond Transient Absorption Spectroscopy of Chromium Hexacarbonyl in Methanol: Observation of Initial Excited States and Carbon Monoxide Dissociation", *J. Phys. Chem.* **93** (8), 2876-2878 (1989).

[46] X. Xie and J. D. Simon, "Picosecond Time Resolved Absorption Studies of the Solvation of $Cr(CO)_5$ in Alcohols: a Unimolecular Kinetic Model for the Formation of $Cr(CO)_5(OHR)$ from Photogenerated $Cr(CO)_5(ROH)$", *J. Am. Chem. Soc.* **112** (3), 1130-1136 (1990).

[47] T. Lian, S. E. Bromberg, M. C. Asplund, H. Yang, and C. B. Harris, "Femtosecond Infrared Studies of the Dissociation and Dynamics of Transition Metal Carbonyls in Solution", *J. Phys. Chem.* **100** (29), 11994-12001 (1996).

[48] R. M. Dahlgren and J. I. Zink, "Ligand Substitution Photochemistry of Monosubstituted Derivatives of Tungsten Hexacarbonyl", *Inorg. Chem.* **16** (12), 3154-3161 (1977).

[49] S. Záliš, M. Busby, T. Kotrba, P. Matousek, M. Towrie, and A. Vlček, "Excited-State Characters and Dynamics of $[W(CO)_5(4\text{-cyanopyridine})]$ and $[W(CO)_5(\text{piperidine})]$ Studied by Picosecond Time-Resolved IR and Resonance Raman Spectroscopy and DFT Calculations: Roles of W → L and W → CO MLCT and LF Excited States Revised", *Inorg. Chem.* **43** (5), 1723-1734 (2004).

[50] K. Kosma, S. A. Trushin, W. Fuß, W. E. Schmid, and B. M. R. Schneider, "Photodissociation of Group-6 Hexacarbonyls: Observation of Coherent Oscillations in an Antisymmetric (Pseudorotation) Vibration in $Mo(CO)_5$ and $W(CO)_5$", *Phys. Chem. Chem. Phys.* **12** (40), 13197-13214 (2010).

[51] J. D. Simon, "Time-Resolved Studies of Solvation in Polar Media", *Acc. Chem. Res.* **21** (3), 128-134 (1988).

[52] N. Agmon, D. Huppert, A. Masad, and E. Pines, "Excited-State Proton-Transfer to Methanol Water Mixtures", *J. Phys. Chem.* **95** (25), 10407-10413 (1991).

[53] U. Harbola, S. Umapathy, and S. Mukamel, "Loss and Gain Signals in Broadband Stimulated-Raman Spectra: Theoretical Analysis", *Phys. Rev. A* **88** (1), 011801(R) (2013).

[54] L. Zhu, W. Liu, and C. Fang, "A Versatile Femtosecond Stimulated Raman Spectroscopy Setup with Tunable Pulses in the Visible to Near Infrared", *Appl. Phys. Lett.* **105** (4), 041106 (2014).

[55] B. G. Oscar, C. Chen, W. Liu, L. Zhu, and C. Fang, "Dynamic Raman Line Shapes on an

Evolving Excited-State Landscape: Insights from Tunable Femtosecond Stimulated Raman Spectroscopy", *J. Phys. Chem. A* **121** (29), 5428-5441 (2017).

[56] D. P. Hoffman and R. A. Mathies, "Femtosecond Stimulated Raman Exposes the Role of Vibrational Coherence in Condensed-Phase Photoreactivity", *Acc. Chem. Res.* **49** (4), 616-625 (2016).

Chapter 9 Concluding Remarks

This thesis has documented our efforts and achievements since 2011 in advancing the wavelength-tunable FSRS methodology and characterizing functional materials in solution. The central theme of the technical work (Chapters 2-6) and characterization work (Chapters 7-8) is the elucidation of structural snapshots during a photoinduced process, which lies at the center of photochemistry wherein the non-equilibrium molecular wavefunction evolves from the reactant to product state. The nonlinear optical insights involve the application of CFWM in generating highly tunable laser sidebands in different phase-matching directions, particularly with an intrinsic OPA effect enabled by the thinness of the transparent medium, the ubiquitous $\chi^{(3)}$ property of the material supplemented by the $\chi^{(2)}$ coefficient, and the noncollinear interaction between the incident 800 nm fundamental pulse and a slightly chirped SCWL.

Notably, the high spatial resolution of FSRS is at the chemical bond level, and even though it is not the exact location of each individual atom, such information is sufficient in tracking structural changes and which functional group of the sample molecule moves first under light irradiation. The simultaneously high temporal resolution is on the fs timescale measured from the cross-correlation between the fs actinic pump and Raman probe pulses, which enables us to precisely initiate a photophysical process or photochemical reaction and capture structural evolution starting from the time zero of photoexcitation. Without detailed kinetic analysis of transient Raman modes

in the electronic excited state as a function of time delay after the actinic pump, we can still gain useful information about the photoinduced reaction mechanism by comparing the different ground state Raman spectrum as a function of light irradiation time (e.g., on the minutes to hours timescale) or solution pH.

The wavelength tunability of FSRS in our lab has been achieved using a home-built ps Raman setup (Chapters 2 and 4), in conjunction with a broadband fs Raman probe from SCWL in sapphire or water as well as from our newly developed BUMA sidebands in a thin transparent medium (e.g., BK7, BBO). The unique time-frequency domain approach of our tunable FSRS setup provides the much needed versatility and generality for nonlinear spectroscopic experiments, complemented by the powerful fs-TA measurements probing the transient electronic states and revealing kinetic time constants. All the incident pulses in FSRS can be individually tuned and optimized. As a result, we can take advantage of the resonance Raman enhancement effect both in the ground state (aided by the steady-state UV/Vis spectral results) or excited state (aided by the time-resolved fs-TA spectral results) to elucidate the photoinduced reaction coordinates for metal-organic complexes in solution involving Bi or W with novel applications in materials science and nanowrite to make microelectronic components in an atom-efficient and environment friendly way.

On the basis of this body of experimental work bridging the gap between structure and function in condensed phase, we envision that tunable FSRS aided by fs-TA spectroscopy will grow into a powerful research and development platform in academic and industrial settings to reveal the working mechanisms of functional molecules in real time with sufficient resolutions to enable

rational design for targeted functionalities. We note that the first commercial turn-key FSRS instrument has been made by Newport, Inc. in 2017 which will broaden the scope and impact of this powerful vibrational technique. Last but not least, the fundamental insights gained from such a unique line of inquiry will continue to enrich modern physical chemistry, chemical physics, photonics, and materials science with a strong perspective for real-world applications.

This page is intentionally left blank.